1-1-2012

Synthesis And Characterization Of Size Controlled Transitionmetal Phosphide Nanoparticles And Their Hydrodesulfurization Catalytic Activity

Galbokka Hewage Layan Savithra
Wayne State University,

Recommended Citation

Savithra, Galbokka Hewage Layan, "Synthesis And Characterization Of Size Controlled Transitionmetal Phosphide Nanoparticles And Their Hydrodesulfurization Catalytic Activity" (2012). *Wayne State University Dissertations.* Paper 696.

SYNTHESIS AND CHARACTERIZATION OF SIZE CONTROLLED TRANSITION METAL PHOSPHIDE NANOPARTICLES AND THEIR HYDRODESULFURIZATION CATALYTIC ACTIVITY

by

GALBOKKA HEWAGE LAYAN SAVITHRA

DISSERTATION

Submitted to the Graduate School

of Wayne State University,

Detroit, Michigan

in partial fulfillment of the requirements

for the degree of

DOCTOR OF PHILOSOPHY

2013

MAJOR: CHEMISTRY (INORGANIC)

Approved by:

Advisor Date

DEDICATION

To my beloved grandmother, Charlet De Zoysa, my parents G.H. Lamasena and W.D. Lalani, and my loving wife Nipuni Gamage

ACKNOWLEDGMENTS

I would like to express my sincere gratitude to Prof. Stephanie L. Brock for her guidance throughout the degree program. Prof. Stephanie L. Brock is an excellent research advisor, a teacher, a motivator, and a person. I am really impressed with her qualities like work ethics, management skills, and professionalism. Most importantly, she is a person with a heart who can understand her students well and treat everyone alike. It has been a great experience to work with her. I would like to say thank you very much Dr. Brock.

I would like to thank my committee members, Prof. Charles Winter, Prof. Colin Poole, and Prof. Simon Ng for their valuable time and suggestions. They have been very helpful during my PhD carrier.

I am grateful my collaborator Prof. Mark Bussell and his group at Western Washington University for their valuable suggestions and ideas throughout my graduate studies. They performed the HDS testing for the sample I made and sent me the data in timely manner. I had the opportunity to work in Bussell lab for 3 weeks in summer, 2010. They helped me a lot during my stay there and treated me well.

I take this opportunity to thank all the CIF staff members of Wayne State University. Dr. Yi Lu and Dr. Mike helped me with TEM, and Dr. Mary Jane Heeg taught me how to use and maintain powder-X-ray diffraction instrument.

I would like to thank all the office staff members of the Department of Chemistry. Melissa Barton, Debbie McCreless, Diane Klimas, and Erin Bachert are really helpful in resolving many paperwork involved during my graduate studies.

I want to thank Nestor Ocampo and technical staff members for their help. Nestor is a friendly person and always there to help for any kind of computer problem.

I would like to thank all the past-Brock group members, Keerthi, Hongtao, Qinghong, Elayaraja, Irina and Shreyashi. It was wonderful experience for me to work with these lab mates. They were really helpful me when I started working in the Brock lab. Keerthi showed me how to do a reaction using glove box and Schlenk line for the first time. Elayaraja and me has great conversations regarding chemistry, politics, and cricket. Irina, Shreyashi, and Qinghong were some of nicest and friendliest people I have ever met during my life. They all are really friendly, helpful, and kind to me.

I also want to thank all the current group members, Yanhua, Lasantha, Asha, Roshini, Derek, Ruchira, and, Jessica. They were really friendly to me and always there for me in various situations. Yanhua is a really helpful friend who resolved a lot of technical problems in my computer. I had the opportunity to work with Lasantha and Asha for a substantial amount time during my graduate studies and had a great time with them.

Finally, would like to thank my family and relatives for their immense and continuous support. My grandmother and parents were always behind me during both good and bad times. They constructed the foundation for me to go there and face any challenge in life. I want to thank my three brothers, Naveendra, Vimukthi, and Thanrindu for their love and care. I am really grateful to my loving my wife for taking care my health and sharing my good and bad times throughout the graduate life.

TABLE OF CONTENTS

LIST OF TABLES

LIST OF FIGURES

CHAPTER 1

INTRODUCTION

Materials tend to show superior or completely different properties from their bulk counterparts when the particle dimensions are reduced to the nanoscale (1-100 nm).[1-11] These unique physiochemical properties of nanoscale materials have led to new research findings in solar cell applications, thermoelectrics, and catalysis among other fields. The increased surface to volume ratio upon decreasing size is particularly relevant to the specific case of catalysis, which is a key focus of the dissertation research. Increased surface to volume ratio allows maximum exposure of the active sites of the catalysts towards reactive species in the reaction. In addition to this effect, changes in the electronic nature of materials upon decreasing size may also impact catalytic activity. For example, Au is an inert metal in the bulk state, but it shows great catalytic activity towards CO oxidation when the particle size is reduced to less than 10 nm.[12] In addition to the particle size effect on heterogeneous catalysis, the chemical reactivity depends on how the atoms at the active sites are arranged on the catalysts' surface. Therefore, the catalytic activity may differ significantly among different crystal facets. For example, Pt is a well-known catalyst for hydrogenation of ethylene and pyrrole. Recently, it has been reported that n-butylamine formation due to pyrrole hydrogenation on the Pt (100) surface is enhanced relative to the Pt (111) surface.[13] Therefore, cubic Pt nanoparticles having well defined (100) facets showed superior catalytic activity to similar sized spherical Pt NPs having (111) facets.

In the dissertation research, the creation of transition metal phosphide nanoparticles with different surface to volume ratios (size control), morphologies (crystal facets), and chemical attributes (noble vs. base metal phosphides) are explored and these characteristics are correlated with catalytic activity towards hydrodesulfurization (HDS). The motivation for these studies lies in the potential to improve activity of transition metal phosphide HDS catalysts for fuel processing by determining the relationships between size, morphology, chemical composition and HDS of thiophenes.

In this chapter, background information about HDS catalysis is described, along with the promise of metal phosphides as next-generation catalysts. Subsequently, synthetic methods for preparing metal phosphide nanoparticles using solution based arrested precipitation and temperature-programmed reduction will be discussed.

1.1. Hydrodesulfurization (HDS)

Organosulfur compounds found in oil sources consist of thiophene, dibenzothiophene, and substituted dibenzothiophenes. The removal of these organosulfur compounds from crude oils is achieved via HDS. The direct reaction between the thiophene ring and H_2 is hard to achieve even at high temperature and pressure, due to the high activation barrier for the reaction.[14] HDS catalysts have active sites capable of binding the two reactants, facilitating the HDS reaction by lowering the activation energy barrier and therefore enabling high rates of conversion.

There are two possible reaction pathways responsible for the HDS catalytic reaction (Figure 1.1). The hydrogenation (HYD) pathway involves perturbation of the aromatic system by reducing the aromatic rings, followed by the reaction between H_2 and the deplanarized S atom. The HYD pathway results in cyclohexylbenzene (CHB) and bicyclohexane (BCH) as byproducts. In contrast, the direct desulfurization (DDS) pathway is characterized by the formation of biphenyl (BP) due to direct reaction of the thiophene with H_2 on the catalysts' surface.[15-18] Gas chromatography is typically employed to probe the components of the gaseous products and thus assess the relative occurrence of the two pathways.

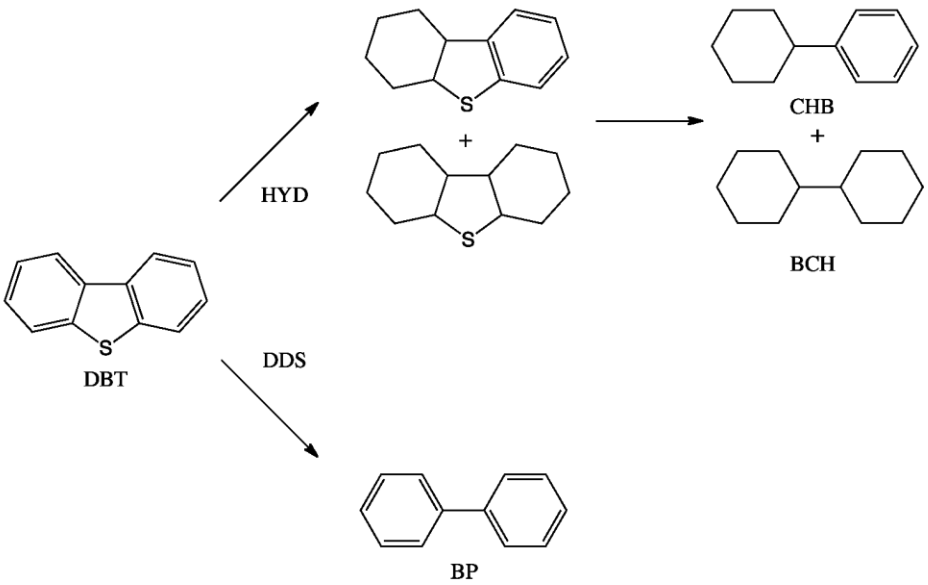

Figure 1.1. Reaction scheme for HDS of dibenzothiophene (DBT) by the hydrogenation (HYD) pathway producing cyclohexylbenzene (CHB) and bicyclohexane (BCH); and by the direct desulfurization (DDS) pathway generating biphenyl (BP).

The removal of bulky refractory sulfur compounds, such as 4,6 dimethyldibenzothiophene (4,6-DMDBT), from crude oil is known as deep-HDS. The very low reactivity of these refractory sulfur compounds is due to steric hindrance limiting access to the C-S bond.[16, 17, 19, 20] Removal of refractory sulfur occurs more efficiently by the hydrogenation (HYD) pathway. Thus, catalysts that favor this pathway will be more effective for deep-HDS.

1.2. Industrial Sulfided-Mo Catalyst for HDS

Industrial molybdenum-based catalysts doped with cobalt or nickel are currently used for hydrotreating, and a two-fold increase in hydrodesulfurization (HDS) capacity has been achieved over the last thirty years by their optimization.[4] However, it is unlikely that sulfided-molybdenum catalysts can be further enhanced to generate ultra-low sulfur levels from low-purity sources. This limitation of the activity can be attributed in part to the layered structure of $MoS_{2,}$ as shown in Figure 1.2. Because metal atoms are exposed only on the edge planes, the active site density is low relative to isotropic materials that expose metal atoms on all crystal faces. Therefore, research is now focused on exploring new and more efficient catalytic systems with high site density to enable reduction of sulfur to ultra-low levels.

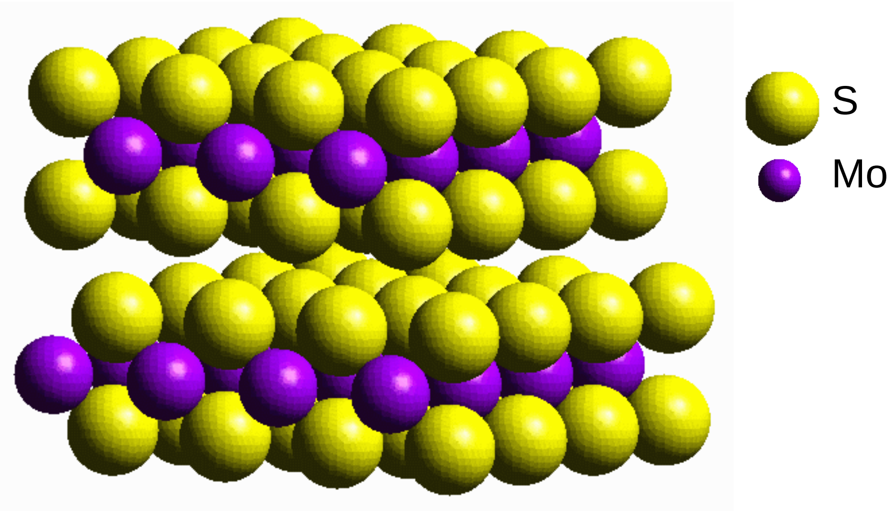

Figure 1.2. Schematic representation of the unit cell of MoS_2.[21]

1.3. Transition Metal Phosphides

Transition metal phosphides exhibit a wide variety of properties making them suitable for a range of applications in catalysis, magnetism, electronics, etc.[22-24] In general, metal-rich phosphides exhibit metal-like properties while phosphorous-rich phosphides show covalent properties. These transition metal phosphides can adopt a wide range of phases for a given metal depending on the metal to phosphorous ratio/stoichiometry and this has consequences for the behavior of the phase. Thus, in the iron phosphide system, magnetic properties are dependent on the Fe:P ratio and their until cell structure. Both Fe_3P and Fe_2P are ferromagnetic with Curie temperatures (T_C) of 217 K and 716 K, respectively, while FeP is anti-ferromagnetic with a Néel temperature (T_N) of 115 K.[12] Importantly, transition metal phosphides that adopt isotropic structures have shown excellent capacity for HDS.[23, 25] Among them, Ni_2P supported on silica exhibits the highest HDS activity relative to other binary metal phosphides (Fe_2P, MoP, WP),[26] including other nickel phosphides (Ni_5P_4 and NiP_2).[23]

Noble metal particles that are good hydriding agents, such as Pd, Pt, or Rh, show high activity for deep-HDS when dispersed on an oxide support.[27-29] However, noble metals are susceptible to sulfur poisoning, causing the activity to drop over time. This problem has been addressed by the use of noble metal phosphides (Rh_2P,[30] Ru_2P,[31] Pd_5P_2) prepared by the temperature programmed reduction method (TPR), see below. Phosphides are more resistant to sulfur poisoning while maintaining good HDS activity. For example, Rh_2P catalysts showed higher dibenzothiophene (DBT) HDS activity compared to commercial Ni-Mo/Al_2O_3 and Rh/SiO_2 catalysts and are sulfur tolerant (stable over 100 h of DBT HDS).[30]

1.3.1 Ni_2P Structure and HDS Activity

Ni_2P has a Fe_2P-type hexagonal until cell structure consisting two types of Ni atoms (type I and type II) as shown in Figure 1.3. The type I Ni atom (Ni_I) is surrounded by four P atoms tetrahedrally while the type II Ni (Ni_{II}) atom is surrounded by five P atoms in a square pyramidal arrangement. It is well established that Ni_{II} sites have higher electron density compared to Ni_I sites because a higher number of P atoms (phosphide) are interacting with the Ni_{II} sites. Therefore, Ni_{II} sites are presumed to predominately facilitate an HYD pathway while Ni_I sites presumably favor the DDS pathway.[32]

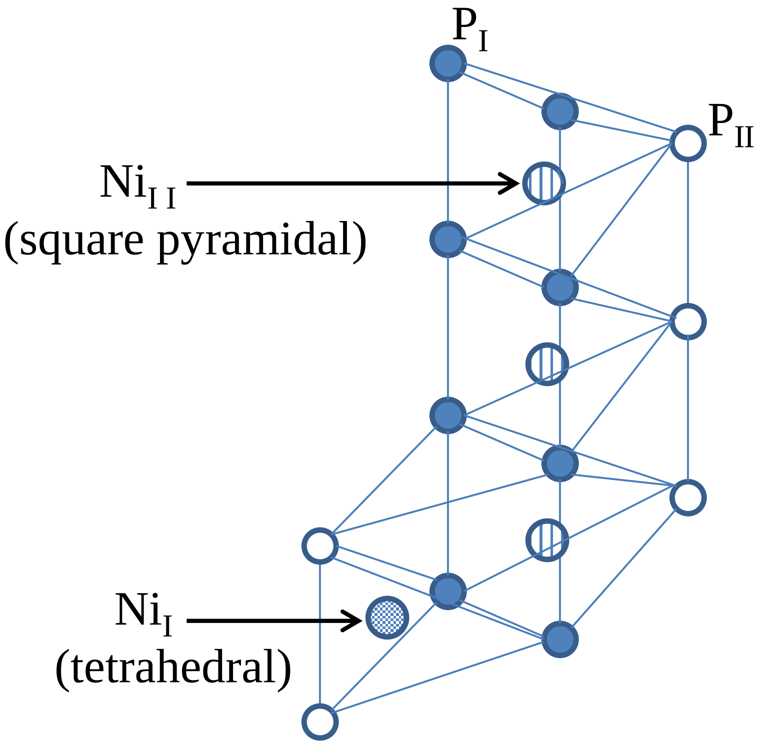

Figure 1.3. Hexagonal structure of Ni_2P unit cell showing the arrangements of Ni and P atoms.[32]

1.4. Incipient Wetness and Temperature Programmed Reduction (TPR)

Incipient wetness impregnation, also called capillary impregnation or dry impregnation, is a commonly used technique for the synthesis of heterogeneous catalysts. Typically, the active-metal precursor is dissolved in an aqueous or organic solution. Then the metal-containing solution is added to a catalyst support containing the same pore volume as the volume of the solution that is to be added, and capillary action draws the solution into the pores.[33-37] Solution added in excess of the support pore volume causes the solution transport to change from a capillary action process to a diffusion process, which is much slower. The catalyst can then be dried and calcined to drive off the volatile components within the solution, depositing the metal on the catalyst surface. The maximum loading is limited by the solubility of the precursor in the solution. The concentration profile of the impregnated compound depends on the mass transfer conditions within the pores during impregnation and drying.

The Oyama and Bussell groups have pioneered the synthesis of supported metal phosphide catalysts by using the incipient wetness method as the first step to disperse metal and P sources on the support followed by temperature programmed reduction (TPR).[23, 25, 38, 39] For the specific case of Ni_2P, They first added aqueous $Ni(NO_3)_2$ solution to an oxide support (silica or alumina) dropwise while mixing thoroughly until the support is saturated, followed by the evaporation of water at 80 °C for 1 h. This cycle is carried out until desired weight loading achieved. An aqueous $(NH_4)_3PO_4$ / $(NH_4)_{3-x}H_xPO_4$ solution is then introduced to the support in a similar manner. After impregnation is complete, the support containing the two ions is subjected to a calcination step. Calcination is an important step in the synthesis because it presumably enables formation of strong interactions between the catalyst precursors and the support.

Following impregnation and calcination, the TPR method is performed to convert the calcined (oxidized) material to Ni_2P. In this technique, the calcined material is placed in a U-shaped quartz tube and then H_2 gas, which is used as the reducing agent, is sent through the oxidized precursor species at elevated temperatures.[40] The reduction of the oxidized species to the final reduced material usually occurs in discrete steps (probed by H_2 consumption) at specific temperatures, as shown in Figure 1.4.

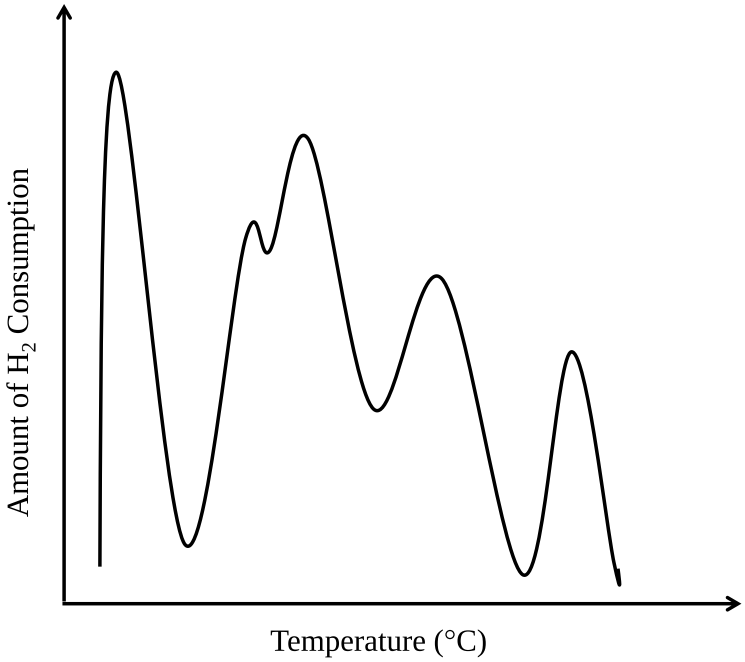

Figure 1.4. A graph showing the variation of H_2 consumption with respect to temperature for the TPR method for a hypothetical material (adapted from Jone).[31]

The amount of H_2 gas consumed is determined by the amount of gas introduced to the reactor and the amount of gas exiting from the reactor. When the gas consumption is large at a specific temperature, it indicates a reduction step is taking place.[40] Therefore, the extent of the reduction can be controlled by adjusting the time and temperature applied. The temperature required for reduction also depends on the starting precursor used. In Ni_2P/SiO_2 synthesis, a lower reduction temperature of 500 °C and a smaller amount of H_2 could convert $NH_4H_2PO_4$ (more reducible) whereas $(NH_4)_3PO_4$ to Ni_2P whereas reduction requires > 700 °C. After the completion of Ni_2P particle formation, the temperature is brought back to room temperature and the surface of the Ni_2P particles is passivated by treatment with a 2% O_2/He mixture before exposing samples to the ambient.

This Ni_2P/SiO_2 catalyst prepared by the TPR method has shown very high HDS activity when compared to other nickel phosphide phases and commercially-used sulfided-Mo catalysts. The Ni_2P/SiO_2 and the commercial Ni-Mo-S/Al_2O_3 catalysts with equal number of active sites as determined by O_2/CO chemisorption measurements were employed to measure and compare the HDS activity of Ni_2P/SiO_2. The Ni_2P/SiO_2 catalyst showed 98% DBT HDS conversion while the commercial Ni-Mo-S/Al_2O_3 catalyst converted only 78% of the DBT during HDS measurements.[23] This activity difference clearly shows the superior HDS catalytic activity of the Ni_2P/SiO_2 catalyst. However, the large polydispersity and a lack of control of particle size are drawbacks of this method that make the study of structure-activity relationships for the Ni_2P catalyst challenging. Accordingly, synthetic methods to make metal phosphide nanoparticles with controlled composition (phase), size, and shape are needed.

1.5. Synthesis of Transition Metal Phosphide Nanoparticles

In order to synthesize monodisperse samples of nanoparticles with controlled size and morphology, the solution-phase arrested-precipitation (SPAP) method has become popular among researchers. In this method, surface protecting ligands are used to arrest the growth of the nanoparticles during the reaction. The surface protecting groups can be either organic or inorganic groups that bind to the nanoparticle surface, thereby controlling the growth. The ability to control and separate nucleation and growth steps is crucial to make monodisperse nanoparticles using this method. This is achieved by either injecting precursor reagents into a hot solvent containing coordinating groups/ligands or mixing the reactants and coordinating ligands followed by increasing the temperature gradually until the nucleation takes place. In both methods, the nucleation step takes place abruptly at a specific temperature, producing a large number of nuclei in the reaction medium. When the temperature is maintained at or below the nucleation temperature, the reaction of monomers with the already formed nuclei becomes a lower energy process than nucleation, resulting in particle growth.[41] In the growth steps, the particles mainly undergo Ostwald ripening, where smaller particles are dissolved resulting in the release of monomers to the medium.[42, 43] This facilitates the further growth of larger particles, enabling formation of monodisperse nanoparticles using SPAP. Other advantages of the SPAP method are the abilities to (1) control size and morphology (spherical, rods, and wires) by changing the coordinating ligands (binding ability) and reaction conditions (concentration, temperature and time) and (2) exchange the surface binding ligands (non-polar with polar groups and vice versa) with other ligands, or remove them entirely, in order to achieve the desired surface properties for the applications in question.

The SPAP method has been used to synthesize a wide range of transition metal phosphides by different research groups.[44-56] Brock and co-workers were the first to demonstrate the synthesis of discrete transition metal phosphide nanoparticles (FeP and MnP) with low polydispersity by this method.[46] In the FeP nanoparticle synthesis, iron(III) acetylacetonate was reacted with a highly reactive P source, $P(SiMe_3)_3$ at a temperature of 260 °C.[46] Highly monodisperse FeP nanoparticles with a size of 4.7 nm resulted when using trioctylphosphine oxide (TOPO) as the solvent and dodecylamine plus myristic hexylphosphonic acid as the capping groups.[46] MnP nanoparticles were prepared similarly by using $Mn_2(CO)_{10}$ and $P(SiMe_3)_3$.[46] Even though $P(SiMe_3)_3$ acts as a good stoichiometric phosphorus source in the above FeP and MnP syntheses, it is very expensive and difficult to handle in the laboratory (highly reactive and pyrophoric). Therefore, a phosphorus source with mild reactivity, (trioctylphosphine (TOP)), was subsequently employed to make MnP, FeP, and CoP nanoparticles.[46] These nanoparticles were also found to be spherical, phase-pure, and highly crystalline, enabling us to avoid expensive and problematic $P(SiMe_3)_3$ in the transition metal phosphide nanoparticles syntheses.

Hyeon and coworkers extended the TOP-based transition metal phosphide synthesis in order to make anisotropic structures (nanorods and nanowires) in contrast to spherical particles.[35, 36] A syringe pump was used to deliver the metal-TOP complex slowly and gradually to the reaction vessel containing octylether and octylamine at > 300 ° C in order to maintain the high monomer concentration in the reaction mixture, facilitating the anisotropic growth of nanoparticles. Shorter Fe_2P nanorods (3 nm x 12 nm) were synthesized when the injection of Fe-TOP into octylether/oleylamine mixture at 300 °C was done once. Longer Fe_2P nanorods (5 nm x 43 nm) were formed after a second addition of Fe-TOP complex, by maintaining the high concentration of monomers and thus enabling the control of nanorod dimensions.[35] They also observed that the length (along the growth direction) of the nanorods tends to increase with decreasing injection rate in MnP systems, where the length of the MnP nanorods was increased from 8 nm to 11 nm while the width of nanorods remained at 15 nm.[49] Finally, the syringe pump synthesis has been extended for nanorod formation to make other metal phosphides such as Co_2P, FeP, and Ni_2P.[49]

Brock and co-workers subsequently reported an alternative method to make MnP nanorods with narrow polydispersity by injecting $Mn_2(CO)_{10}$ dissolved in octadecene into a hot TOP/TOPO mixture rapidly.[57] In contrast to the Hyeon method, this method resulted in shorter MnP nanorods when the injection rate was reduced. While Hyeon and co-workers injected the Mn-TOP complex slowly into the solvent/coordinating ligands mixture, Brock and co-workers introduced the Mn-octadecene mixture into the TOP/TOPO mixture rapidly (as a single step). Therefore, the sequence of reagent addition, rate of injection, and nature of the reagents along with material structure play major roles in deciding the anisotropic growth of metal phosphides.

In 2007, Schaak and co-workers reported a general strategy to convert a series of metal nanoparticles into metal phosphide nanoparticles using TOP under mild conditions.[53] In this method, the metal nanoparticles (Ni, Rh, Pt, Co, Pd, etc.) were synthesized at relatively low temperature (< 300 °C) from thermal decomposition of their corresponding precursors. These metal nanoparticles were then isolated and reacted with TOP at a relatively high temperature (> 300 °C). The conversion of metal to metal phosphide appears to go through a metal-rich phase to achieve a phosphorus-rich final product, presumably because TOP slowly releases reactive phosphorus species to the reaction medium. Therefore, elevated temperature and longer times favor the formation of phosphorus-rich products. Moreover, Schaak and co-workers also observed formation of hollow Ni_2P nanoparticles, attributed to the nanoscale Kirkendall effect, in which the diffusion rate of Ni outward is greater than the diffusion rate of P inward, resulting in void formation.[42, 45] At the same time as Schaak, Chiang and co-workers also reported formation hollow Ni_2P nanoparticles as the result of reaction between Ni nanoparticles and TOP.[55]

Brock an co-workers used Schaak's metal to metal-phosphide conversion strategy to make phase-pure Fe_2P nanoparticles successfully.[58] They also extended this strategy to the nickel phosphide system in order to establish and optimize reaction conditions to control phase and morphology simultaneously.[59] In this study, the factors governing the final phase and morphology were studied systematically with respect to the precursor concentration, temperature, surfactant (oleylamine) concentration, and time. In this study, both Ni_2P and $Ni_{12}P_5$ nanoparticles were synthesized as hollow or solid particles. The morphology (solid or hollow) of the final nickel phosphide phase is dependent on the initial P:Ni ratio, where a high ratio yielded amorphous Ni-P nanoparticles and a low P:Ni ratio yielded crystalline Ni nanoparticles at relatively low temperature (< 260 °C). Upon increasing the temperature (> 300 °C), the smaller amorphous Ni-P nanoparticles were converted to solid nickel phosphide nanoparticles and the larger crystalline Ni nanoparticles were converted to hollow nickel phosphide. In addition, Brock and co-workers also showed the templated conversion of $Ni_{12}P_5$ nanoparticles into Ni_2P nanoparticles upon reaction with TOP at elevated temperature.[60] Finally, the feasibility of converting metal oxide precursor particles into metal phosphides was demonstrated for generation of Ni_2P, FeP, and CoP.[61] This suggests that oxidation is not an impediment to phosphide formation.

1.5.1 HDS Studies of SPAP-prepared Ni_2P Nanoparticles

Our group first reported the formation of monodisperse, discrete and fully dense Ni_2P nanoparticles by cannulating a bis(1,5-cyclooctadiene)nickel(0)/TOP mixture into a hot coordinating solvent (TOPO) and heating the reaction mixture at 350 °C for 24 hours.[56] These TOPO/TOP capped Ni_2P nanoparticles were washed using chloroform to remove surface ligands. Thiophene HDS activity was measured for unsupported Ni_2P nanoparticles and compared to TPR-prepared unsupported Ni_2P. The catalytic activity of the unsupported Ni_2P nanoparticle sample was ~ two times higher than the TPR-generated Ni_2P particle sample. These data suggested that SPAP-prepared Ni_2P nanoparticles potentially have an inherently high HDS catalytic activity.

1.6 Thesis Statement

Conventional oil sources, such as Arabian crude oils, are being depleted substantially and their price is increasing rapidly. Therefore, countries all around the world have turned their attention towards new energy sources, including unconventional oil sources. There is a crucial limitation for usage of unconventional oil sources, such as Canadian oil sands, even though they are still abundant and less costly. The higher impurity levels, especially sulfur, in crude oil derived from oil sands (5 wt% S) compared to low-impurity Arabian crude oils (1.8-2.9 wt% S) is a major obstacle for the efficient and wide usage of these oil sources.[1] Commercially available hydrodesulfurization (HDS) catalysts have failed to reduce S to the level demanded by health and environmental guidelines (5 ppm by 2010). In addition, proton exchange membrane (PEM) fuel cells used for production of hydrogen (H_2) by reformulating fuels,[2] and copper-based catalysts used for the water-gas shift (WGS) reaction[3] to produce H_2, are particularly sensitive to sulfur poisoning. Thus, ultra-low sulfur levels in fuels will also be needed for effective functioning of these systems.

Industrial molybdenum-based catalysts doped with cobalt or nickel are currently used for hydrotreating, and a two-fold increase in hydrodesulfurization (HDS) capacity has been achieved over the last thirty years by their optimization.[4] However, it is unlikely that sulfided molybdenum catalysts can be further enhanced to generate ultra-low sulfur levels from low-purity sources. This limitation of the activity can be attributed in part to the layered structure of MoS_2. Because metal atoms are exposed only on the edge planes, the active site density is low relative to isotropic materials that expose metal atoms on all crystal faces. Therefore, research is now focused on exploring new and more efficient catalytic systems with high site density to enable reduction of sulfur to ultra-low levels.

Transition metal phosphides that adopt isotropic structures have shown excellent capacity for HDS.[5,6] Among them, Ni_2P supported on silica exhibits the highest HDS activity relative to other metal phosphides (Fe_2P, MoP, WP),[7] including other nickel phosphides (Ni_5P_4 and NiP_2).[5] Particle size is expected to play an important role in the heterogeneous catalytic activity of Ni_2P, as active site density scales inversely with size. However, the conventional synthetic method for catalyst production (temperature programmed reduction of supported nickel phosphate) results in polydisperse particle sizes with average sizes that vary with loading, making it difficult to independently assess the effect of size and loading, or to extract pertinent mechanistic information.

Recently, it has been shown that noble metal phosphides (Rh_2P, Pd_5P_2) have a high capacity for removal of substituted dibenzothiophenes (4,6-dimethylbenzothiophene), which requires a hydrogenation step (HYD).[8,9] These phosphides have the benefit of being more resistant to S poisoning than the native metals as discussed in Chapter 1.3. Thus, a two stage system where the primary catalyst reduces the S load (by removal of less bulky thiophenes) by a direct desulfurization pathway (DDS), so that the secondary catalyst can remove the more refractory S by HDS, a process referred to as deep-HDS, can be used.[10,11] As with Ni_2P, these catalysts are prepared by TPR where there is little control of size and dispersity.

The dissertation research has two aims: (I) Establish the relationship between site density and the HDS activity of Ni_2P nanoparticles supported on silica; and (II) Synthesize monodisperse Pd_5P_2 nanoparticles and study their HDS activity and product selectivity.

In addressing aim I, we have targeted an arrested precipitation method for the synthesis of Ni_2P nanoparticles that yields narrow polydispersity samples with control of size. Chapter 3 discusses the size-controlled synthesis of Ni_2P nanoparticles and the preparation of a Ni_2P/SiO_2 precatalyst using the incipient wetness method. Chapter 3 also includes preliminary size-dependent HDS data for a Ni_2P/SiO_2 catalyst. However, the size-dependent HDS of Ni_2P/SiO_2 catalyst could not be correlated with the simple surface to volume ratio of Ni_2P nanoparticles, because of the significant sintering that occurred during the testing process. Accordingly, a systematic sintering study of Ni_2P nanoparticles supported on silica using the incipient wetness method was performed is also described in this Chapter.

In order to reduce sintering, a large scale approach for in-situ incorporation of Ni_2P nanoparticles within mesoporous silica was pursued, as described in Chapter 4. The mesoporous shell reduces sintering and thus enables the size-dependent activity of $Ni_2P@mSiO_2$ to be probed. HDS is performed on different sized particle samples over the temperature range of 200 – 425 °C. HDS activity of $Ni_2P@mSiO_2$ catalyst increases with the decreasing particle size, as expected, in contrast to results from Chapter 3 on non-encapsulated catalysts.

In addressing aim II, we have developed a novel approach to make Pd_5P_2 particles in the size range of 6-10 nm by encapsulation of amorphous Pd-P nanoparticles in a mesoporous silica shell followed by crystallization (Chapter 5). In the first step, monodisperse Pd-P nanoparticles are formed using an arrested precipitation method. The mesoporous silica shell is then added to prevent particle sintering. Finally, the conversion of $Pd\text{-}P@mSiO_2$ to $Pd_5P_2@mSiO_2$ is carried out by heating at 500 °C for 2 hours under 5% H_2/Ar mixture in a flow furnace. HDS activity is assessed and confirms access of DBT to the catalyst surface.

In addition to the research chapters, there is a chapter describing the experimental methods used (Chapter 2) . A final chapter describing conclusions and future directions (Chapter 6) is also provided.

CHAPTER 2

EXPERIMENTAL AND MATERIALS CHARACTERIZATION TECHNIQUES

This chapter focuses on the experimental methods and characterization techniques employed in this dissertation research study. Transition metal phosphide (Ni_2P, Rh_2P, Pd_5P_2) syntheses were carried out by arrested precipitation reactions using air-sensitive synthetic techniques (glove box and Schlenk line). The materials synthesized were characterized by a variety of material characterization methods including Powder X-Ray Diffraction (PXRD), Transmission Electron Microscopy (TEM), Energy Dispersive Spectroscopy (EDS), BET surface area and porosimetry analysis, Thermogravimetric Analysis (TGA), and IR spectroscopy. Finally, HDS catalytic activity was evaluated for the transition metal phosphide catalysts in collaboration with Prof. Mark E. Bussell in the department of Chemistry at Western Washington University.

2.1 Experimental Techniques

2.1.1 Inert Atmosphere Glove Box

Inert atmosphere glove boxes provide storage and handling space for air and moisture sensitive materials in laboratories. The glove box consists of a tightly sealed steel box and one or two gloves connected to the window of the box. A source of an inert gas (Ar) is connected to the steel box. The continuous circulation of Ar gas through a copper catalyst and molecular sieves is maintained to remove trace amounts of oxygen and water inside the box. The copper catalyst and molecular sieves are periodically regenerated by heating under a mixture of H_2 and N_2 followed by evacuation. In this process, oxygen adsorbed on to copper is eliminated as H_2O (moisture), resulting in a fresh copper catalyst surface back. The water from the molecular sieves and Cu regeneration is removed in the final evacuation process. The box is connected to the outside through an antechamber (small and/or big). Materials are introduced to the antechamber and then degassed using a vacuum pump connected to the chamber for a sufficient time (minimum of 20 minutes) to remove air/moisture before refilling with Ar from the box and transferring the contents from the chamber to the box. A photohelic pressure gauge connected to the glove box maintains the positive pressure inside, minimizing air getting in through pin holes in the rubber gloves, or other weak points.

2.1.2 Schlenk Line Techniques

Schlenk line techniques are used to maintain an inert and moisture-free environment in the reaction vessel (Schlenk flask). The line consists of two manifolds; one is attached to an inert gas (Ar) tank and other is attached to a vacuum pump via a cold trap (liquid N_2). The double manifold line has several ports with two way stopcocks that are connected to the Schlenk flasks through flexible rubber tubes. The Schlenk flask containing the reaction mixture is typically loaded in the glove box, sealed, and then attached to the line. It is first degassed by opening the side arm of the flask to the evacuation manifold via a two way stopcock. The flask is then filled with inert gas (Ar) by opening the stopcock to the Ar line manifold. Reactions are typically conducted under a positive pressure of Ar.

2.2 Characterization Techniques

2.2.1 Powder X-Ray Diffraction (PXRD)

Powder X-ray diffraction (PXRD) is a fingerprint technique used to identify the structure, phase and crystallinity of a material. X-rays are electromagnetic radiation of wavelength ~ 0.1 nm and are produced as a result of the collision of high energy electrons (accelerated through A 30-50 kV electric field) with matter. A schematic diagram of an X-ray generator tube is shown in Figure 2.1. The electrons produced by a heated tungsten filament travel through a vacuum in the tube and strike the anode (Cu - in the case of all studies presented in this dissertation).

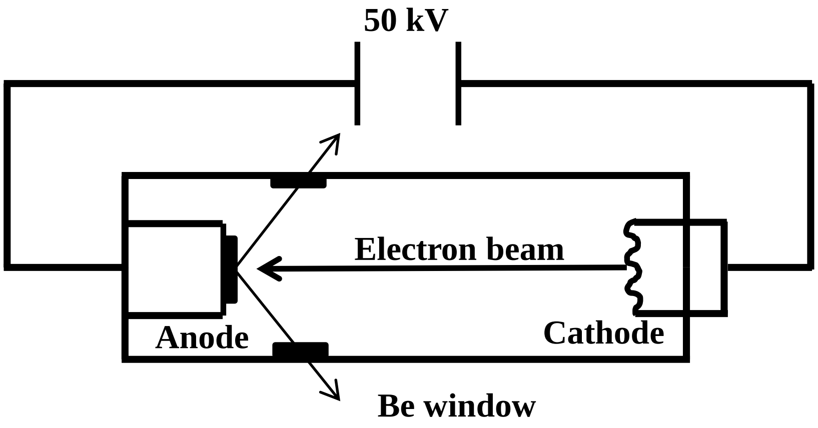

Figure 2.1. Schematic diagram of an X-ray generator tube (adapted from West).

As shown in Figure 2.2, the collision of the high energy electron results in removal of an electron from the K shell of the Cu anode leaving a vacancy. This vacancy is immediately filled by a higher energy electron from 2p or 3p orbitals. This electron transition from a high to a low energy shell results in emission of energy as electromagnetic radiation (X-rays). Two major transitions take place resulting in two radiation waves with varying energies. The transition of the electron from the 2p to the 1s is known as the K_α line (1.5418 Å, Cu) and, 3p to 1s is the K_β line (1.3922 Å, Cu) for Cu. A monochromator is used to filter out the K_β line to exclusively use the more intense K_α line for experiments.

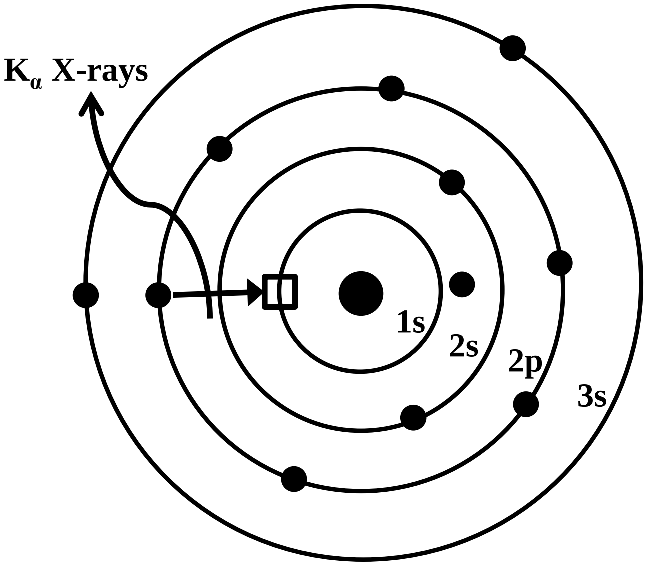

Figure 2.2 Illustration of the generation of a Cu Kα X-ray from the ionization of a 1s electron followed by transition of a 2p electron into the vacancy (adapted from West).

Crystals are composed of planes of atoms as regularly repeating patterns (Figure 2.3). When X-rays collide with these crystal planes, a fraction of the X-rays is diffracted from the atoms at an angle equal to the incident angle (θ) (a to a’). Additional rays can penetrate through the top crystal planes and undergo similar diffraction events at deeper planes (b to b’). These diffracted waves interfere with each other either constructively or destructively. Constructive interference is generated when the diffracted waves are in phase as shown in Figure 2.3, resulting in an enhanced signal (intensity) of X-ray waves that can be detected and quantified. According to Bragg's law, the summation of the extra distances traveled by the wave (xyz) should be equal to nλ for constructive interference to take place (Equation 2.1).

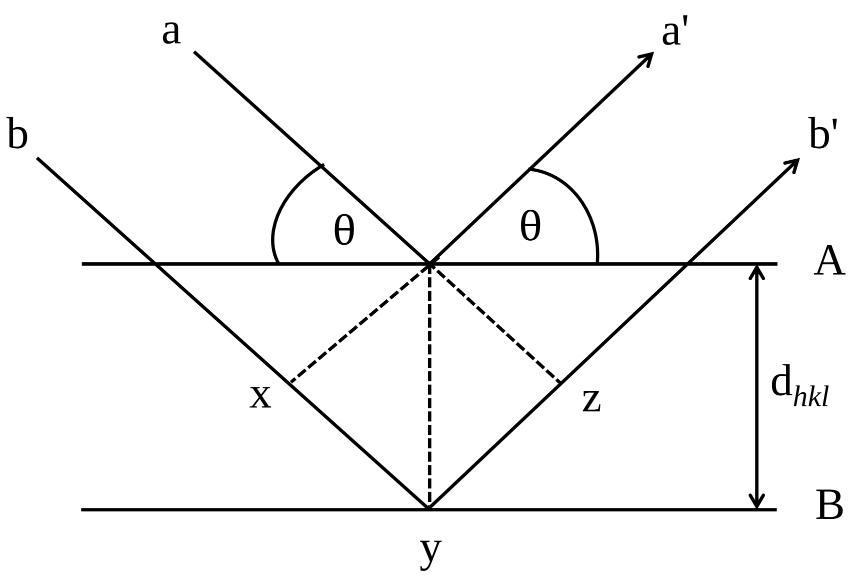

Figure 2.3 Schematic representation of the diffraction of X-rays by lattice planes in a crystal (adapted from West).

$$n\lambda = xyz \qquad (2.1)$$

xyz is related to the angle θ and interplane spacing, d, by Equation 2.2.

$$2d\sin\theta = xyz \qquad (2.2)$$

Combining Equations 2.1 and 2.2 yields Equation. 2.3, Bragg's law.

$$2d\sin\theta = n\lambda \qquad (2.3)$$

In a powder sample, crystallites are arranged in all possible directions. Thus, rotation of the x-ray source by θ relative to the detector ensures that if there are planes of correct d spacing. Only the diffracted beam resultant by constructive interference is detected. The signals are then represented as a one-dimensional plot where X-ray intensities are plotted against 2θ. The peak positions of a PXRD pattern depend on the shape of the unit cell and symmetry while the intensity of the peaks depend on the electron density of atoms making up the material as well as the symmetry of their arrangement.

The PXRD pattern (peak width) of a nanoscale material differs with respect to that of the bulk form. On the nanoscale, a material consists of a lesser number of lattice planes compared to larger crystallites. Therefore, there is not complete cancellation of diffracted beams that do not satisfy Bragg's law. This results in broader PXRD peaks for nanocrystals. As the crystallite size is reduced, the breadth of the PXRD peaks increases. The quantitative relationship between crystallite size and peak breadth is expressed by the Scherrer formula given in Equation 2.4 where t is the size of the crystallites (thickness), λ is the wavelength of X-rays, B is the full width at half maximum (FWHM) of the peak and θ is the angle at which the diffraction occurs.

$$t = \frac{0.9\lambda}{B\cos\theta} \tag{2.4}$$

In this study, PXRD patterns were collected on a Rigaku diffractometer RU 200B (40kV, 150 mA, Cu Kα radiation). Samples were deposited on a zero-background quartz holder coated with a thin layer of grease and the data were acquired in the 2θ range of 30-75° with a step size of 1.2°. The PXRD data obtained were processed using Jade software and compared to powder diffraction files (PDFs) from the International Center for Diffraction Data Package (ICDD).

2.2.2 Transmission Electron Microscopy (TEM)

The invention of transmission electron microscopy (TEM) has led to a tremendous development in the characterization and visualization of materials on the atomic to micrometer level. This led to significant advances in nanotechnology where the transmission electron microscope is an essential tool for characterization of nanoparticle size, shape, and morphology.

Electrons have a wave-like nature with wavelengths significantly smaller than visible light, leading to enhanced resolution. By changing the accelerating voltage of a TEM instrument, it is possible to change the wavelength of the electrons. The ability to manipulate the wavelength of electrons (most TEM instruments operate at voltages of 100-300 kV) has enabled consistent improvements in the imaging with respect to resolution.

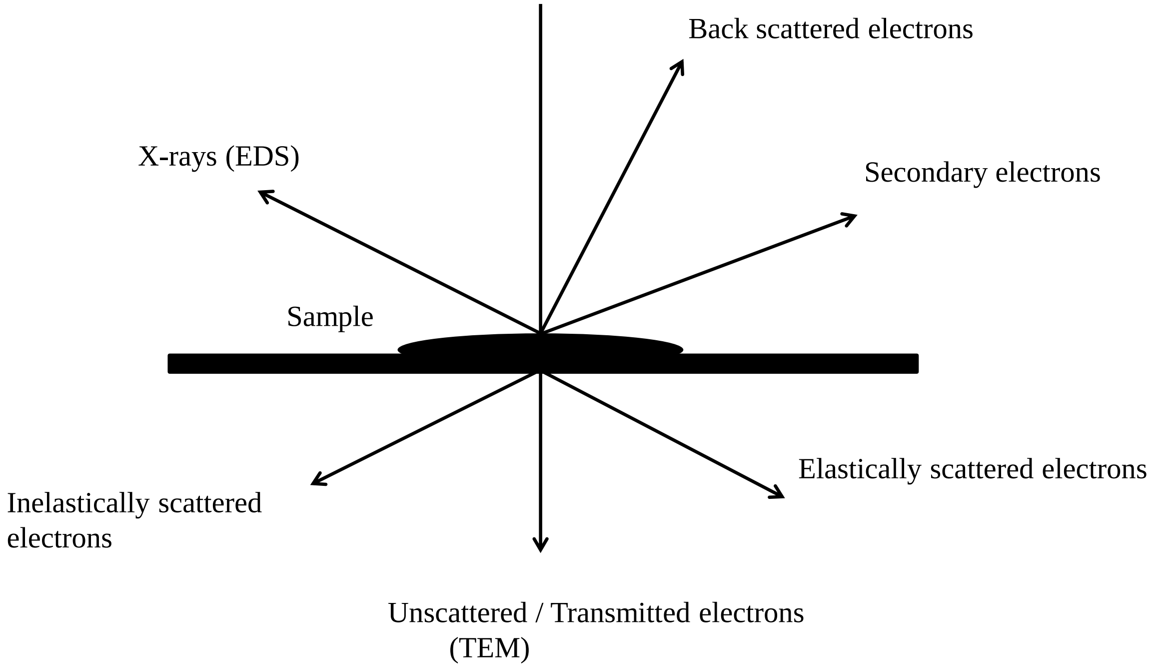

Figure 2.4. Processes occurring in a sample when a material is bombarded with high energy electron beam.

When high energy electrons hit the specimen, the interactions of the highly energetic electron beam and sample take place, resulting in several electronic excitations as shown in Figure 2.4. In Transmission electron microscopy (TEM), the electrons that are transmitted and scattered are used to image the material, thereby providing morphological and structural features of the material. The wavelength of the generated electrons has an inverse relationship with the accelerating voltage of the instrument as shown in Equation 2.5. Therefore, the spatial resolution can be optimized by increasing the operating voltage. In high resolution transmission electron microscopy (HRTEM), lattice fringes can be imaged if the particles are crystalline enabling us to study the crystal structure of the material. This is especially useful to determine the growth direction of anisotropic materials such as nanorods and nanowires.

$$\lambda = \frac{h}{\left(2m_0eV\right)^{1/2}} \qquad (2.5)$$

Figure 2.5 shows a pictorial representation of a typical TEM instrument with its components. Typically a Cu grid is used to support nanoparticles dispersed in a suitable solvent. Then, the nanoparticles-containing grid is mounted onto a special sample holder and inserted into the TEM instrument. An electron beam generated in the electron gun due to a high voltage (200 kV in the case of this dissertation research) is passed through a series of condenser lenses. These condenser lenses help to concentrate or direct the electron beam onto the goniometer (sample specimen). The electrons transmitted form the sample specimen passes through objective lenses, constructing the image and the diffraction pattern. Objective and intermediate apertures further magnify the constructed image and the diffraction pattern. As the transmitted electrons hit a florescent screen or camera, TEM images of the sample can be visualized.

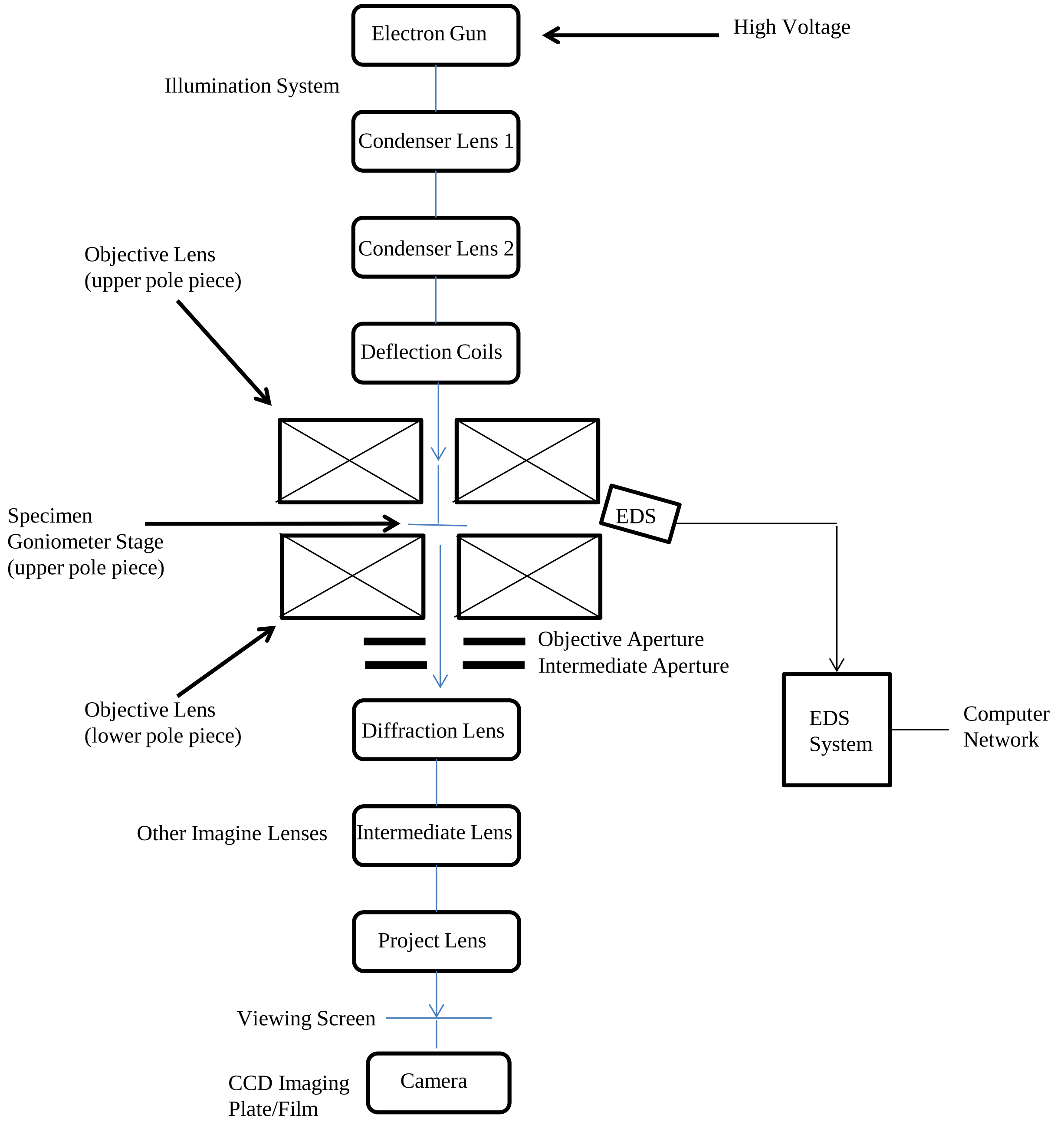

Figure 2.5 Pictorial representation of a typical TEM instrument (adapted from Fultz).[62]

In this dissertation work, samples were imaged with a JEOL 2010 analytical TEM at an accelerating voltage of 200 kV and a current of 109 μA. The images obtained were analyzed by Amtv600 software (Advanced Microscopy Techniques). Samples for TEM were prepared by dispersing metal phosphide nanoparticles (Ni_2P, Rh_2P, and Pd_5P_2) in chloroform while mesoporous silica coated particles were dispersed using methanol. A drop of the resultant solution was deposited on a carbon-coated 200 mesh Cu grid (SPI), followed by air drying for a few hours. The particle size distribution was calculated from measuring using well separated particles in TEM micrographs using the scion image size calculation software.

2.2.3 Energy Dispersive Spectroscopy (EDS)

Energy dispersive spectroscopy (EDS) is a semi-quantitative method used to probe the elemental composition of a material. In this technique, high energy X-rays generated due to the bombardment of high energy electrons with the specimen are analyzed. The energy (wavelength) of the emitted X-ray is dependent on the identity of elements of the material. The relative intensities of X-rays generated from the component elements provides comprising information on the relative ratio of elements in the material. In this dissertation research, EDS data were collected using a EDAX, Inc. detector attached to the TEM (JEOL 2010). EDAX Genesis software was used for analyzing the elemental composition of the sample.

2.2.4. Atomic Absorption Spectroscopy (AAS)

Atomic-absorption (AA) spectroscopy is an analytical technique for the quantification of elements of interest. In this technique, gas phase atoms are excited by radiation having identical wavelength to the excitation wavelength of the element. The solid or liquid phase samples are first vaporized into the gas phase in a flame or graphite furnace before electronic excitation. These vaporized atoms are introduced to the atomization shell where they adsorb UV or visible light causing electronic transitions from lower to higher energy levels. The components of an AA spectrometer include a hollow cathode lamp (radiation source), atomization shell, a monochromator, and a detector.

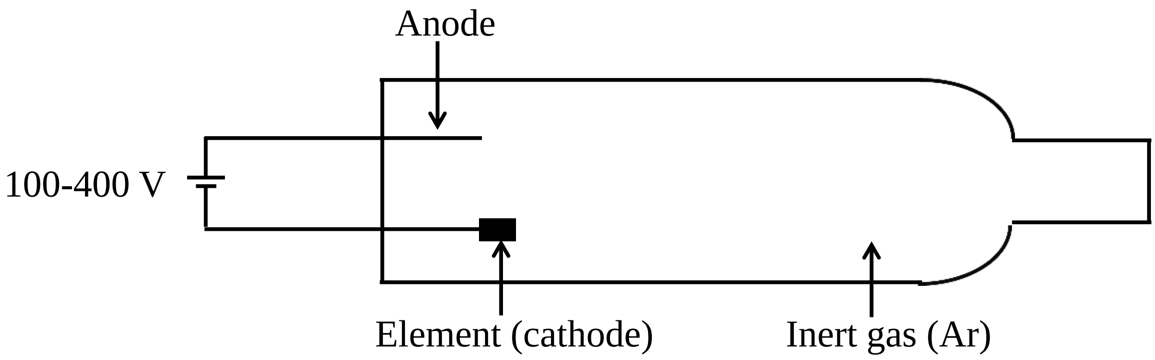

Figure 2.6. Schematic diagram of a hollow cathode lamp.[63]

A hollow-cathode lamp (HCL) is often used as the radiation source and emits characteristic radiation of the element of which it is made. A HCL is composed of a cathode of the element of interest, a tungsten anode, Ar inert gas, and a glass cylindrical housing as shown in Figure 2.6.[63] A near-vacuum pressure (100-200 Pa) is maintained inside the lamp with Ar or Ne inert gases. Upon applying a voltage (100-400 V) across the cathode and anode, the outer electrons of the inert gas are excited and produce positively charged ions (Ar^+) in the HCL tube. These positively charged ions then interact with the negatively charged cathode (consisting element of interest) resulting in ejection of atoms of the cathode element. These cathode atoms then undergo a series of excitations and relaxations. The most intense line emitted is filtered from the rest of the radiation using a monochromator and is used to excite the vaporized atoms of the sample in the atomization shell. The amount of analyte (concentration) is determined by the extent of absorption. According to the Beer-Lambert law, the concentration and path length are directly proportional to the absorption. However, the Beer-Lambert law can't be directly employed in AAS, because a only a fraction of atoms get vaporized when the sample is a solid or a gas. Therefore, a calibration curve is constructed using a series of known concentrations of the element of interest to quantify the concentration of unknown (analyte).

In this dissertation research, a series of $Ni^{2+}_{(aq)}$ standards were prepared (2, 4, 6, 8, and 10 ppm) by diluting a 1000 ppm standard Ni^{2+} in 2% HNO_3 and 2% HNO_3. These solutions were used to construct a calibration curve. Silica impregnated and in-situ mesoporous silica incorporated Ni_2P particles were first digested with a few drops of conc. HNO_3 before diluting to a it 2% HNO_3 aqueous solution. A Perkin Elmer AAnalyst 700 atomic absorption spectrometer equipped with a flame furnace was used to determine the weight loading of Ni_2P catalysts supported on to silica.

2.2.5. Infrared Spectroscopy (IR)

Solution based nanoparticle synthesis involves the use of organic ligands as capping groups. In order to use these nanomaterials as catalysts, it is important to remove these surface ligands and expose the particle surface. IR spectroscopy can be an important tool for probing the presence of organic ligands (organic functional groups). In this technique, IR radiation is used as the energy source to excite vibration modes of polar molecules. The vibrating frequency of a specific bond or functional groups is directly related to the mass of atoms involved in the vibration and the strength of the bond between atoms. For example, IR vibration frequency increases as the bond strength increases (double bonds have higher frequency than single bonds between the same atoms). The intensity of the vibration band (peak) in the IR spectrum depends on the polarizabilty and vibration mode of the bond. Therefore, this technique provides information about the functional groups and their relative composition present on the nanoparticle surface. Most organic functional groups adsorb IR radiation in the region 4000-600 cm^{-1}.

In this dissertation study, a Varian FTS 3000 MX FTIR spectrometer was used to probe ligand groups on the nanoparticles' surface. KBr powder was ground with nanoparticle powder and placed in a 13 mm dye and pressed up to 2000-3000 psi pressure using a Carver hydraulic pellet press to produce a transparent pellet for analysis.

2.2.6. Thermogravimetric Analysis (TGA)

Thermogravimetric analysis (TGA) is very useful technique for analyzing desorption and decomposition temperatures of a material of interest. It also provides quantitative analysis of the weight fraction that undergoes desorption or decomposition at a specific temperature or temperature range. In this technique, a very small amount of sample (5 mg) is placed in a crucible and suspended from a high precision balance with a resolution of 0.001 mg. A thermocouple is placed very close to the sample to detect the accurate temperature of the sample when the temperature is ramped up. Finally, a flow of gas (air, N_2 or H_2/Ar) is introduced and the sample mass is recorded as a function of temperature.

In this dissertation research, A Perkin-Elmer Pyris 1 thermogravimetric analyzer was used to determine ligand and template desorption or decomposition temperatures and relative weight losses. The data were collected and analysed using the Pyris Manager Software.

2.2.7 Surface Area Analysis and Pore Size Distribution

Gas sorption is a powerful technique for analysis of porous materials. Depending on the interaction between solid surface (adsorbent) and gases (adsorbate), adsorption can be categorized in to two classes. When the interaction is weak (Van der Waals forces) between adsorbent and adsorbate, it is known as physisorption whereas chemical interaction between adsorbent and adsorbate is known as chemisorption. In chemisorption, the chemical interaction can be either covalent or ionic depending on the nature of two components involved.

In a surface area analysis experiment, the sample is first subjected to the degassing process by heating at appropriate temperature under vacuum or under nitrogen flow. In this step, moisture and organic ligands are desorbed from the system. This step is crucial in purifying the exposing the sample surface for adsorption of gases. The specific temperature and amount of time required depend on the nature of the sample. After the degassing step, the sample is brought to room temperature and the actual mass of the sample is measured. The next step, analysis, is done by transferring the sample tube to the analysis port. The system temperature is brought down to 77.2 K by using liquid nitrogen to ensure complete coverage of adsorbent by adsorbate. In this dissertation research, N_2 gas is used as an inert adsorbate to ensure physisorption. N_2 gas is introduced slowly to the tube containing a known quantity of the sample, and the change in gas pressure arising from physisorption is recorded. The change in gas pressure becomes insignificant as the surface becomes saturated. The quantity of gas adsorbed can thus be calculated using basic gas laws, as the volume of the sample tube and the mass of sample are known.

To create an adsorption isotherm, the amount of gas adsorbed (cm^3/g) is plotted versus the relative pressure (P/P_O), where P is the actual pressure and P_O is the saturation pressure at constant temperature (77.2 K). In a surface area analysis experiments, both adsorption and desorption isotherms are constructed providing valuable information on the nature of pores constituting the material.

The pores present in a solid sample can be categorized into 3 classes depending on their sizes. Micropores (2 nm) are the smallest class of pores and they are filled first at relatively low gas pressure. As the pressure of adsorbate (N_2) molecules increases, a monolayer of coverage on the adsorbent is formed. After that, mesopores (2-50 nm) are filled at relatively high pressure. A third class of pores, macropores (< 50 nm), are then filled when the pressure is increased further. [64]

Isotherms patterns can be categorized into six classes depending on the shape, as shown in Figure 2.7.[64] A type I isotherm shows a gradual increase of volume adsorbed with the relative pressure initially, and then saturates. Type I isotherms are characteristic of a sample composed of small pores (micropores, < 2nm). The type II and type IV isotherms show an identical adsorption pattern, but the type IV isotherm shows hysteresis due to an incomplete desorption. Both type II and IV are indications of the presence of mesopores (2-50 nm) and macropores (> 50 nm) in the material. Type III and Type V isotherms are observed when the interaction between adsorbate and adsorbent is weak or adsorbate molecules have greater attraction for each other than the solid material. Type VI isotherms occur in the presence of a highly smooth surface and suggets layer-by-layer adsorption.

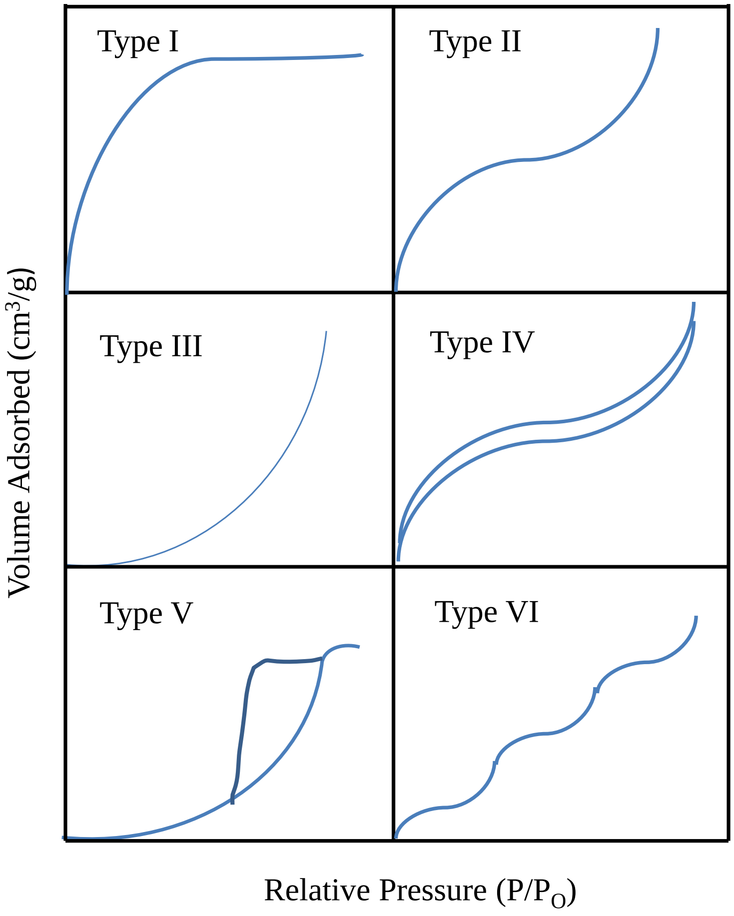

Figure 2.7 Six basic types of adsorption isotherms, adapted from Webb.[64]

The Brunauer, Emmett and Teller (BET) theoretical model is applied to the adsorption/desorption isotherms collected during the analysis to determine the surface area of the material. BET theory is applicable when multilayers are formed between adsorbent and adsorbate due to physisorption.[64] As there is no interaction between layers (physisorption) in the multilayer, BET theory predicts a linear expression when the adsorption/desorption takes place at moderate relative pressures (P/P_0), commonly from 0.02 to 0.20, as shown in Equation 2.6.

$$\frac{P}{V_a(P_0 - P)} = \frac{1}{V_m C} + \frac{C-1}{V_m C}\left(\frac{P}{P_0}\right) \tag{2.6}$$

V_a = volume of the gas adsorbed at a given relative pressure (P/P_0)

V_m = volume of the gas required for monolayer coverage

C = a constant

According to equation 2.6, V_m and C are the gradient and intercept of a plot of $P/(V_a(P_0-P))$ *vs.* P/P_0. This plot can be constructed using the adsorption/desorption isotherm data.[64]

In order to obtain pore volumes, average pore size and pore size distributions, the Barrett, Joyner and Halenda (BJH) theoretical model is employed as shown in Equation 2.7. This model assumes that all the pores have cylindrical geometry. The BJH model collects the data from the portion of the adsorption/desorption isotherm where pore filling and emptying occurs. The amount (volume) of removed or added adsorbate has a direct relationship to the volume of pores and is controlled by the relative pressure.

$$\ln\left(\frac{P^*}{P_0}\right) = \left(\frac{2\gamma\nu\cos\theta}{RTr_m}\right) \tag{2.7}$$

P* = critical condensation pressure

γ = liquid surface tension

ν = molar volume of the condensed adsorptive

θ = contact angle between the solid and condensed phase

r_m = mean radius of curvature of the liquid meniscus

R = ideal gas constant

T = absolute temperature

In the dissertation research, surface area and pore size analysis were performed using a Micromeritics Tristar II surface area/porosimeter. Samples were degassed before analysis at 200 °C for 12 hours under 500 mmHg vacuum. Surface areas were computed based on the Brunauer–Emmett–Teller (BET) multimolecular adsorption method and pore sizes and their distribution were determined using the BJH model.

2.3.7 Hydrodesulfurization (HDS) Catalytic Activity Measurements (Conducted at Western Washington University in the Lab of Mark Bussell)

Catalyst samples were pretreated in flowing H_2 at 377 °C for 2 hours prior to the HDS activity measurements. The HDS activity measurements were carried out using a fixed-bed flow reactor design, operating at a total pressure of 3.0 MPa and temperatures in the range of 225-400 °C. The reactor feed consisted of a solution containing 3000 ppm dibenzothiophene and 500 ppm dodecane. The liquid feed (5.4 mL/h) was injected into a 100 mL/min flow of hydrogen and vaporized prior to entry into the reactor. Aliquots of the products resultant from the catalytic reaction were collected as a function of temperature in 25 K intervals and were quantified using an offline gas chromatography technique.[30]

CHAPTER 3

CONTROL OF SIZE AND MORPHOLOGY OF Ni_2P NANOPARTICLES: STUDYING SIZE DEPENDENT HDS ACTIVITY AND ITS SINTERING BEHAVOIR

3.1 Introduction

Solution-phase arrested-precipitation reactions represent a powerful approach to generate narrow polydispersity nanoparticles of controlled size. The synthesis of discrete Ni_2P nanoparticles by such methods has been reported by several research groups [53, 55, 56, 59, 65, 66] and involves either direct reaction between an organometallic or coordination complex (Ni source) and a phosphine[10] (P source), or between pre-made Ni/NiO nanoparticles and a phosphine.[5,9,61] In general, these reports do not focus on controlling size and the resultant materials are polydisperse and often not phase-pure. Recently, we have adapted and improved the Ni_2P synthesis method originally developed by Schaak and co-workers[53] to make spherical hollow and solid Ni_2P nanoparticles without other phosphide impurities and with a nearly monodisperse size distribution. In the dissertation research, the ability to control size in the range 5-20 nm is demonstrated for the first time. Preliminary data collected on Ni_2P nanoparticles supported on silica, alumina, or silica-alumina by the impregnation method is revealed and the observed catalytic activity related to the sintering behavior of Ni_2P nanoparticles under catalytic conditions. Accordingly, processing conditions that can reduce or eliminate sintering are probed. Finally, a method to produce anisotropic particles (nanorods) is reported with the goal of elucidating crystal face effects on activity.

I collected all data in this chapter with the exception of HDS catalytic data which were collected in Bussell lab in department of chemistry at western Washington University.

3.2 Experimental Section

All chemicals used for the syntheses described in this Chapter are listed in Section 2.1.

3.2.1. Synthesis of Size-Controlled Monodisperse Ni_2P Nanoparticles

All reactions were carried out under an Argon atmosphere using standard Schlenk line and glove box techniques. The synthesis of phase-pure Ni_2P nanoparticles involves two steps. In the first, the synthesis of Ni/Ni_xP_y precursor particles was performed by taking 2 mmol of nickel acetylacetonate ($Ni(acac)_2$), 5 mL of TOP, 10 mL of octylether (solvent), and x mL (x = 2 to 20 mL) of oleylamine and heating at 230 °C for 90 minutes. The conversion of precursor particles to Ni_2P (step 2) was done by injecting 5-10 mL of TOP (depending on the amount of OA added initially) at 230 °C. The system temperature was then raised to 350 °C and kept for 2 hours, then allowed to cool naturally to room temperature. The black precipitate (as-prepared Ni_2P) is dispersed with chloroform (ca. 4 mL) and precipitated with excess ethanol. The as-prepared sample of Ni_2P nanoparticles is then sonicated in chloroform to remove organics bound to the surface of the nanoparticles and re-precipitated by adding excess ethanol. This sonication-precipitation cycle is done at least three times to remove as much of the bound organics as possible from the system. The isolated black powder ($CHCl_3$-washed) is then dried under vacuum.

3.2.2. Preparation of 10 wt % Ni_2P/Support (Silica, ASA, and γ-alumina) Precatalysts

Silica, ASA (hybrid of silica and γ-alumina), and γ-alumina supports were calcined at 500 °C for 3 hours in air prior to use. 100 mg of Ni_2P particles was placed in 5 mL of ethanol and sonicated for 30 minutes until the particles were completely dispersed. The dispersed Ni_2P particles were then introduced onto a support (900 mg) drop-wise (incipient wetness method). Ethanol was then evaporated out from the system by heating at 80 °C under Ar flow. The resulting Ni_2P/support composite was dried under vacuum to remove any residual solvent. In order to determine the actual Ni loading on the support, atomic absorption spectroscopy (AAS) measurements were taken described in Chapter 2.2.4

3.2.3. Acquisition of HDS Activity Data on Supported Ni_2P Catalysts

Catalyst samples were pretreated in flowing H_2 at 373 °C for 2 hours prior to the HDS activity measurements. The HDS activity measurements were carried out using a fixed-bed flow reactor design, operating at a total pressure of 3.0 MPa and temperatures in the range of 225-375 °C. The reactor feed consisted of a solution containing 3000 ppm dibenzothiophene and 500 ppm dodecane. The liquid feed (5.4 mL/h) was injected into a 100 mL/min flow of hydrogen and vaporized prior to entry into the reactor. Aliquots of the products resultant from the catalytic reaction were collected as a function of temperature in 25 °C intervals and were quantified using an offline gas chromatography technique.[30]

3.2.4. Exploration of Sintering Behavior Using Ni_2P/SiO_2 Catalysts

The factors that may contribute to the sintering of Ni_2P nanoparticles during the reducing HDS catalytic conditions, such as temperature (200-650 °C), loading (2.5-20 wt%), time (0.5-6 hours), and the impregnation method (one-step vs. step-wise) were studied independently. Treatment of support with solutions of Ni^{2+} and/or PO_4^{3-} prior to introduction of nanoparticles was also tested by adding 1 mL each of 1.5 M $Ni(NO_3)_2\cdot 6H_2O$ and $(NH_4)_2HPO_4$ solutions to 1 g of 10 wt% Ni_2P/SiO_2 precatalyst. Ni_2P/SiO_2 precatalysts were subsequently placed in a quartz tube and heated in a furnace from 200-650 °C under a flow of 5% H_2/Ar.

3.2.5. Synthesis of Ni_2P Nanorods with Varying Aspect Ratios: Study of Reactive Crystal Face Effects on HDS Catalytic Activity

The synthesis of Ni_2P nanorods consists of two steps as described by Muthuswamy et. al.[61] In the first, the synthesis of precursor NiO particles was done by taking varying amounts (0.5, 1, and 2 mmol) of $Ni(acac)_2$, 10 mL of octyl ether (solvent), 4 mL of oleylamine and heating at 260 °C for 2 hrs under bubbling air. The system was then bought to room temperature, and NiO particles were isolated by centrifuging. NiO nanoparticles were mixed with 10 mL octyl ether and 5 mL oleylamine in a Schlenk flask. The subsequent conversion of isolated precursor NiO to Ni_2P nanorods was done by injecting 10 mL of TOP at 230 °C and increasing the temperature to 350 °C. The black precipitate (as-prepared Ni_2P rods) was isolated by dispersing with chloroform and re-precipitating with ethanol as described in Chapter 3.2.1. The rods were then dispersed on to a silica support and HDS activity was measured as described in Chapter 3.2.2 and 3.2.3.

3.3. Results and Discussion

3.3.1 Synthesis of Size Controlled Ni_2P Nanoparticles *(Spherical, Solid, and Monodisperse)*

The synthesis of phase-pure nickel phosphide nanoparticles using solution-phase approaches is challenging due to the existence of a large number of accessible Ni_xP_y phases within the phase diagram. In particular, $Ni_{12}P_5$ and Ni_5P_4 phases are hard to avoid in the synthesis of Ni_2P because these three phases are formed in a narrow temperature range (from 300 °C to 350 °C). Control of the Ni_2P nanoparticle size can also be challenging because changing reaction parameters such as temperature, precursor ratio (P:Ni), surfactant concentration, and heating time to control nucleation and growth may lead to morphological and phase changes in nickel phosphide systems.[8] While there is considerable literature describing the precise control of metal nanoparticle size,[15, 67-70] to our knowledge, there is no report of controlled size tunability of phase-pure metal phosphide nanoparticles, primarily due to the challenge of maintaining the desired phase and spherical morphology upon changing the growth parameters.

In previous studies, we and others have shown that precursor Ni/Ni-P particles are formed by arrested precipitation reactions between TOP and Ni(acac)$_2$ in octylether at 230 °C.[50, 59] We found that when the precursor P:Ni ratio is less than 1.12, highly crystalline Ni nanoparticles are formed as the intermediate or precursor particles. Crystalline Ni results in hollow nickel phosphide nanoparticle formation upon increasing the temperature range to 300-350 °C, attributed to the Kirkendall effect.[65] However, when the P:Ni ratio is greater than 2.8, the intermediate particles formed at 230 °C are amorphous Ni-P particles, and these yield fully dense nickel phosphide particles when the temperature is increased. The morphological changes are attributed to (1) the larger size of the crystalline Ni particles relative to the amorphous Ni-P particles resulting in a longer diffusion length for phosphidation and (2) a greater (Ni:P) concentration gradiant in the Ni nanoparticles (where the initial P content is zero) relative to the Ni-P amorphous alloy. Moreover, Muthusawamy et. al reported that the conversion of intermediate Ni/Ni-P to $Ni_2P/Ni_{12}P_5$ is a templated conversion in which the morphology and size of the intermediate particles is maintained in the final Ni_2P particles. Thus, control of size at the precursor level is expected to enable size control at the product level.

To target fully dense nickel phosphide nanoparticles, we carried out a series of reactions using a TOP:Ni ratio of 5.6 (2 mmol of Ni(acac)$_2$ and 5 ml (11.12 mmol) of TOP) to favor formation of Ni-P amorphous precursor particles, and we varied the amount of oleylamine (2 -20 mL = 6 - 60 mmol) to control size. Ni-P nanoparticles formed at 230 °C over 90 min (Figure

3.1) were then converted to Ni_2P dense nanoparticles by injecting an extra portion of TOP (5 mL) and then increasing the temperature to 350 °C. Extra TOP is needed whenever the OAm:Ni ratio is ≥ 3, as is the case here, because excess oleylamine (relative to TOP) favors the more reduced $Ni_{12}P_5$ phase. [59]

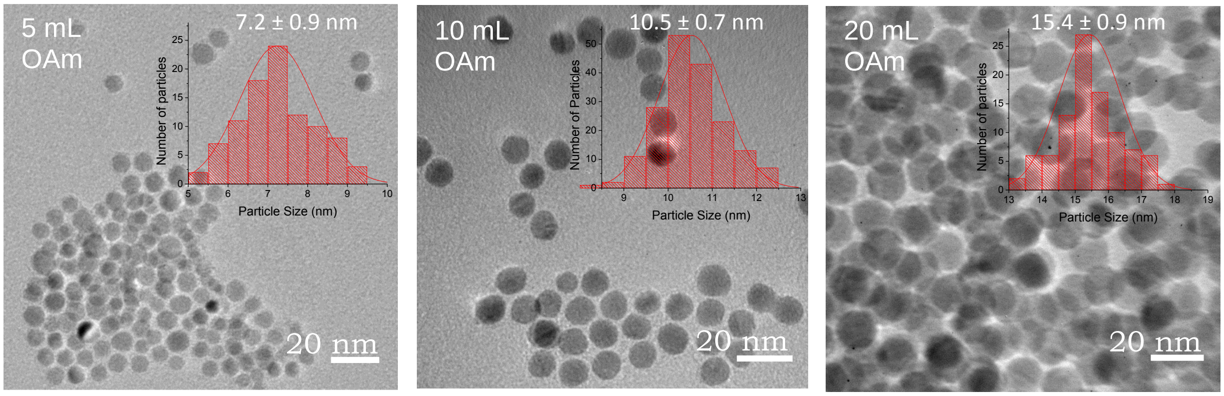

Figure 3.1. TEM images and particle size histograms of intermediate Ni-P amorphous particles prepared at 230 °C with varying amounts of oleylamine (5, 10, and 20 mL).

Based on observations made by Carenc and co-workers we anticipated that particle size would decrease with increasing oleylamine.[15] In their study, the crystalline Ni nanoparticle size is reduced when the amount of oleylamine is increased from 2 to 8 equivalents relative to 0.8 equivalents of TOP and 1 equivalent of Ni. At this low concentration of TOP (P:Ni < 1.12), crystalline Ni particles, not amorphous Ni-P alloys, form as the product. They attributed the reduction of the particle size as the oleylamine amount is increased to the increased nucleation rate of Ni(0) by oleylamine, which acts as a reducing solvent, resulting in more nuclei and hence smaller particle sizes.

Figure 3.2 shows the powder X-ray diffraction patterns of Ni_2P nanoparticles prepared with different quantities of oleylamine. The size of the nanoparticles was calculated using the Scherrer formula on the (200) reflection. As shown in Figure 3.3, Ni_2P particles are solid, spherical, and monodisperse, as needed for the study of the active site density on HDS activity. The particle sizes determined by TEM analysis are very similar to the crystallite sizes calculated by PXRD analysis using the Scherrer equation (Figure 3.2), suggesting these particles are fully crystalline. Thus, we also find that the Ni_2P particle size depends on the amount of oleylamine used; However, in contrast to Carenc and co-workers, more oleylamine yields larger sizes.

We attribute the unexpected size increase with increasing oleylamine quantity in part to the large amount of TOP used in our reaction. We maintained a TOP:Ni ratio of 5.6, in which the resulting intermediate particles are not crystalline Ni but amorphous Ni-P particles. Since incorporation of “P” is needed for the phase to form, TOP must react with Ni during formation of the nuclei. As the reaction mixture consists of both oleylamine and TOP, mass transfer of TOP to the Ni-P species can be slowed down by the presence of oleylamine; as the oleylamine amount is increased, the binding ability and reaction rate of TOP with Ni(0) would be decreased. Thus, the rate of generation of Ni-P would be slower, resulting in bigger particles as we increase the amount of oleylamine. Indeed, size analysis of these precursor particles is consistent with this analysis (Figure 3.1). 5 mL of oleylamine yields precursor particles of 7.2 nm whereas 20 mL of oleylamine gives a size of 15.4 nm. As previously noted, there is a strong size correlation between precursor Ni-P amorphous particles and the crystalline Ni_2P particles that result from reaction with more TOP at high temperature. Thus 10.5 ± 0.7 nm precursor particles result in 10.8 ± 0.7 nm product particles. The slight increase in size is attributed to the increased unit cell size due to incorporation of P.

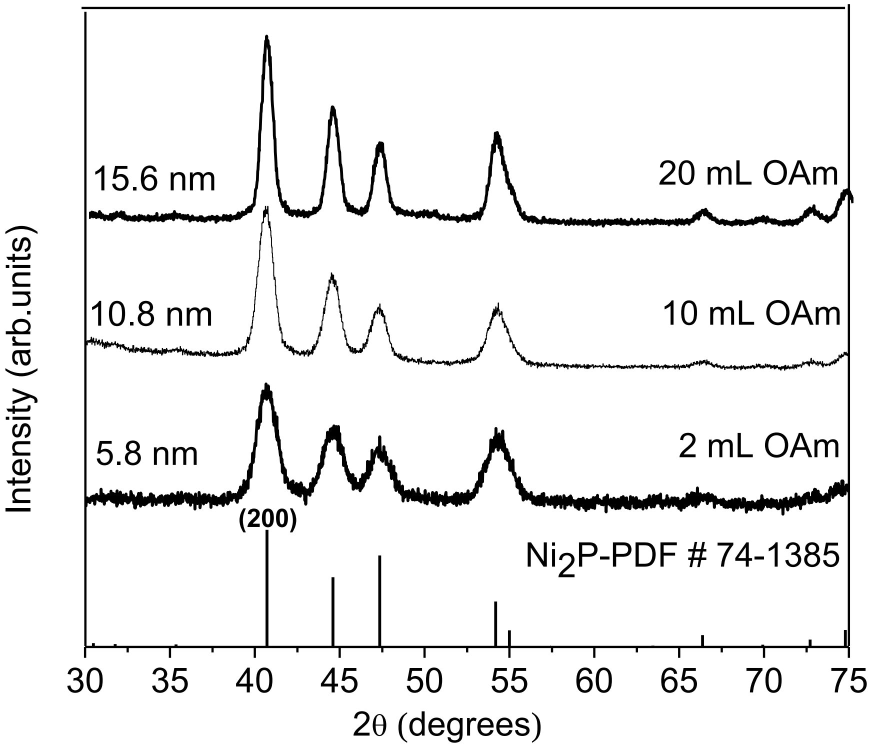

Figure 3.2. PXRD patterns of Ni_2P nanoparticles prepared using different amounts of oleylamine (2, 10, and 20 mL) compared to the Ni_2P reference pattern (PDF # 74-1385). The crystallite sizes of each sample were calculated using the Scherrer equation.

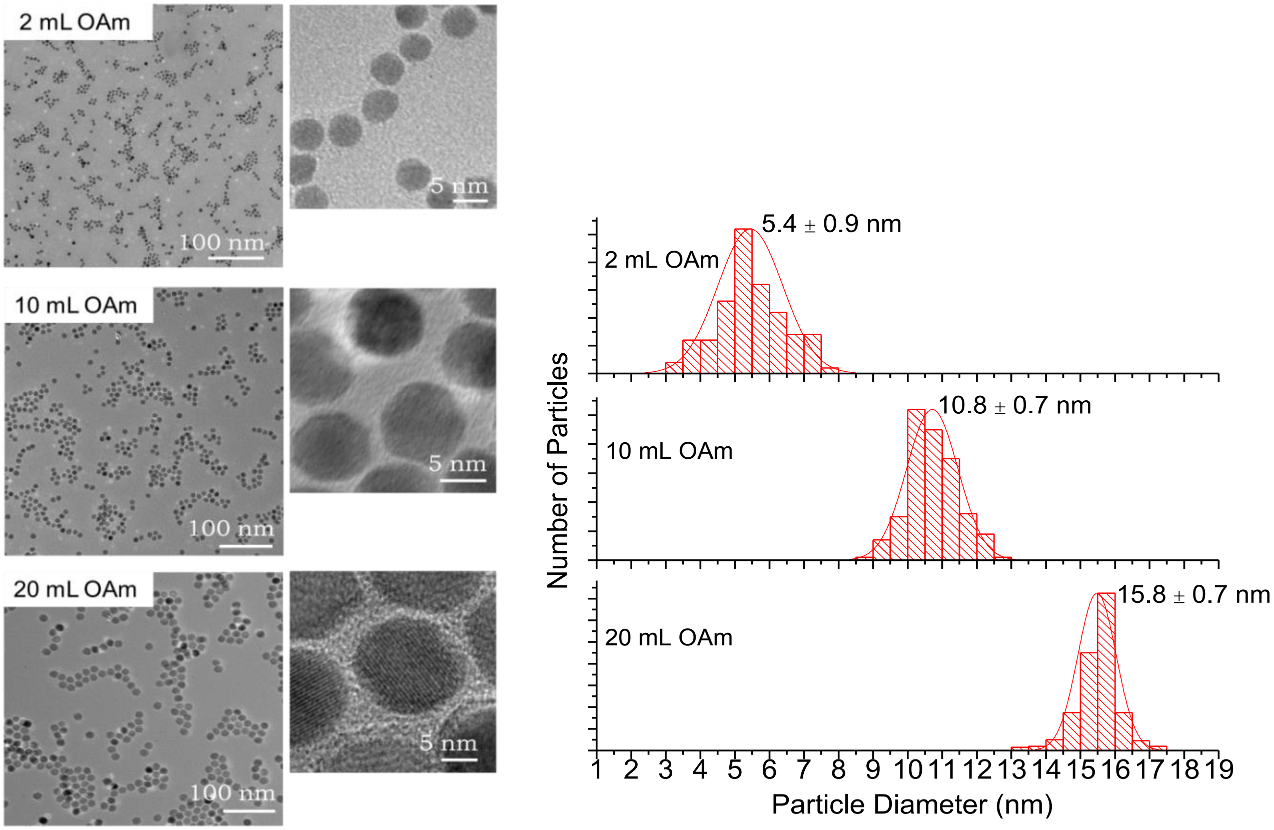

Figure 3.3. TEM images (left) and particle size histograms of Ni_2P particles (right) prepared with varying amounts of oleylamine (OAm).

3.3.2. Preliminary Size Dependent DBT HDS Activity and Product Selectivity of Ni_2P/SiO_2 Catalysts

In order to perform catalytic testing, the Ni_2P nanoparticles were dispersed in ethanol and introduced onto a silica support dropwise, followed by evaporation of ethanol at 80 °C. TEM images of Ni_2P/SiO_2 composites (Figure 3.4) suggest that Ni_2P nanoparticles (high contrast) remain discrete and are distributed throughout the silica matrix (low contrast).

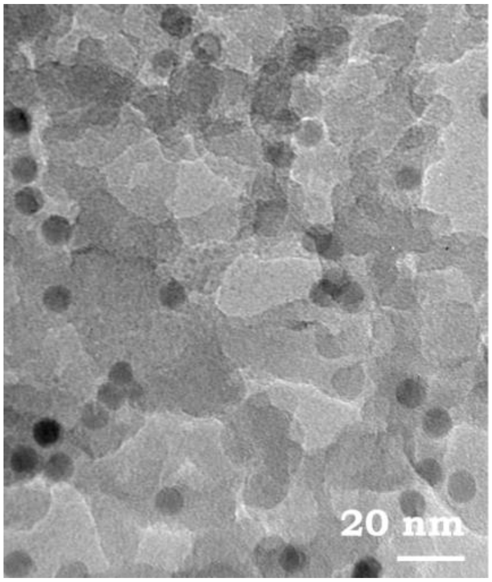

Figure 3.4. TEM image of Ni_2P (11 nm)/SiO_2 precatalyst.

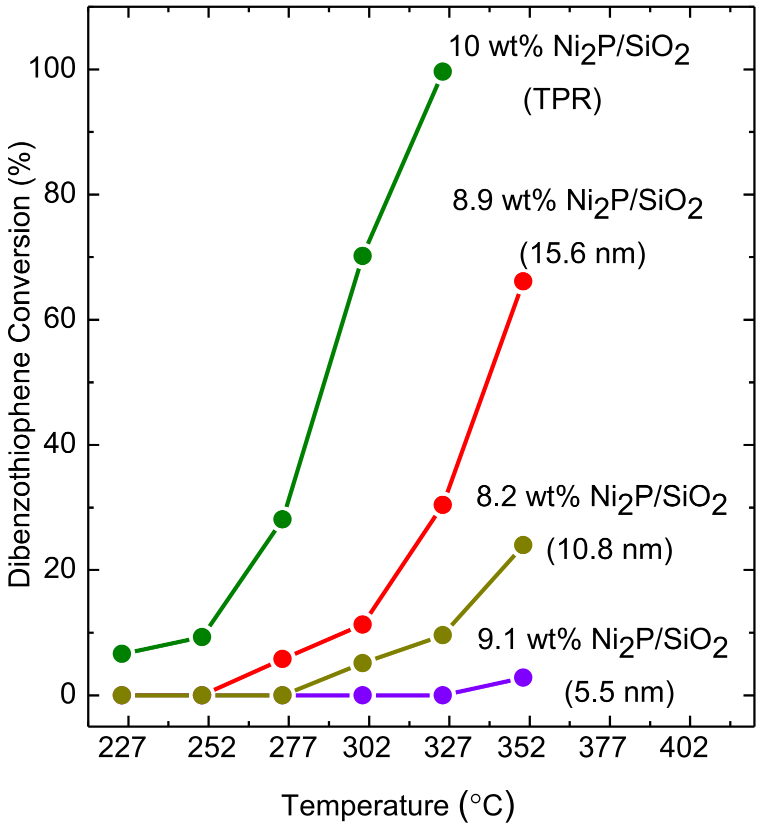

Figure 3.5. Dibenzothiophene HDS conversion of Ni_2P/SiO_2 catalysts with varying particle size as a function of the reaction temperature.

HDS activity of Ni_2P/SiO_2 samples preheated at 377 °C for 2 h under flowing H_2 was measured using a fixed-bed flow reactor in the temperature range of 25-350 °C (Figure 3.5). The products of the dibenzothiophene HDS catalytic reaction were collected in 25 °C intervals. It was presumed that smaller particles would show higher HDS catalytic activity, because the surface to volume ratio (active site density) is increased as particle size decreases. However, our preliminary data shows the exact opposite (Figure 3.5). Moreover, even the most active of the pre-formed supported nanoparticles show a lower degree of dibenzothiophene conversion than

TPR prepared Ni_2P catalysts. The product selectivity of nanoparticle-based N_2P/SiO_2 catalysts is similar to that of TPR-generated catalysts and they all favor the direct desulfurization (DDS) pathway leading to biphenyl (BP) as the major product (Figure 1.1 in Chapter 1 and Figure 3.6). In order to understand the unexpected size dependence and low HDS activity, and thereby improve the performance of silica supported Ni_2P nanoparticle catalysts, we characterized the catalysts post-HDS.

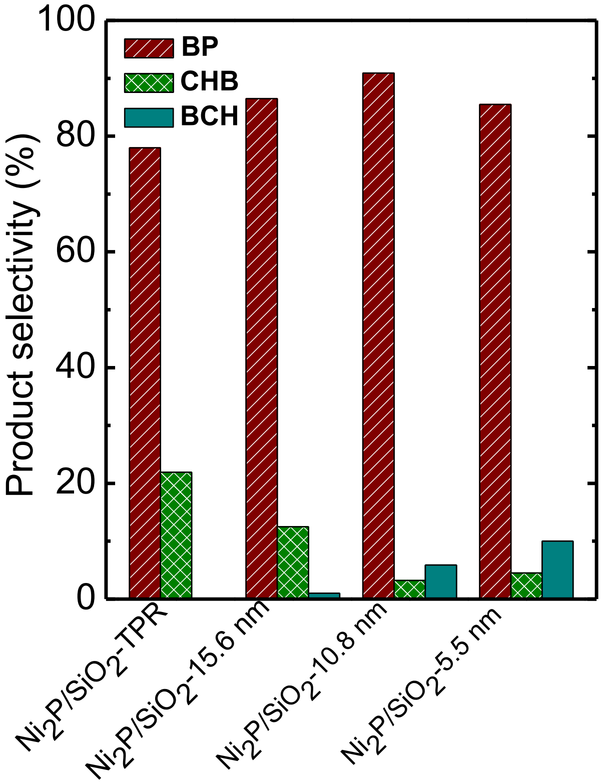

Figure 3.6. Dibenzothiophene HDS product selectivities of Ni_2P/SiO_2 at 352 °C, (BP-biphenyl, CHB-cyclohexanebenzene, and BCH-bicyclohexane).

3.3.3. Study of Post-DBT HDS Ni_2P/SiO_2 Catalyst

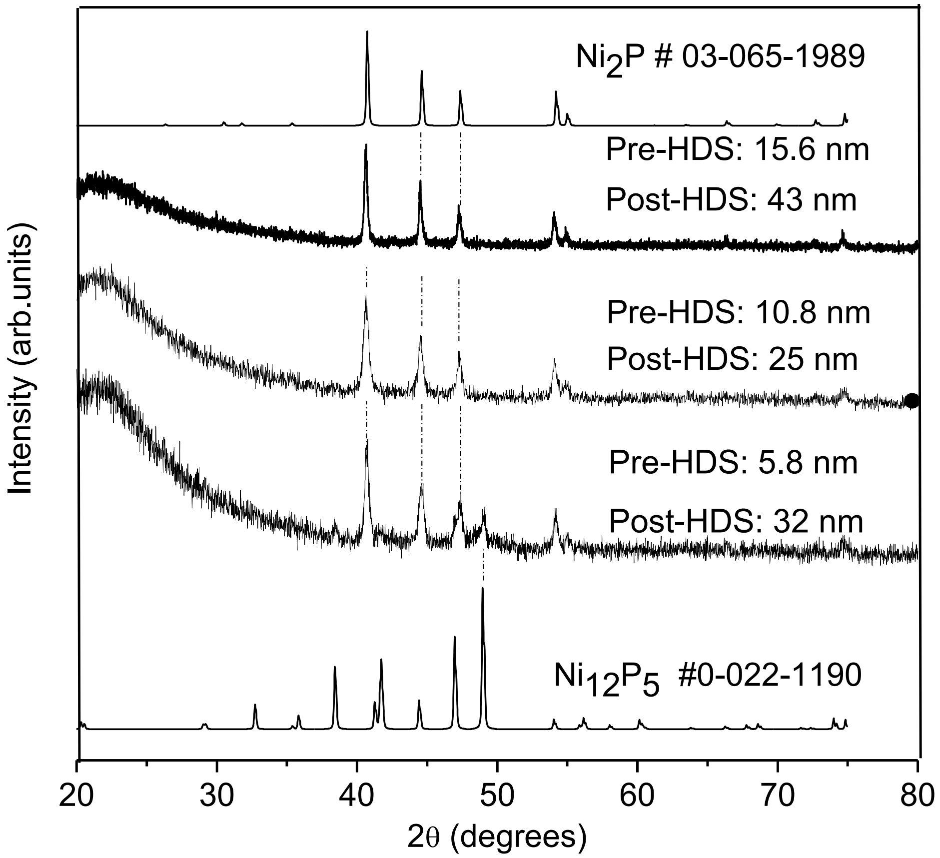

Figure 3.7. PXRD data of post-HDS Ni_2P/SiO_2 samples with Scherrer analyzed crystallite sizes for pre- and post-HDS.

PXRD analysis of catalyst samples post-HDS (Figure 3.7) reveals a substantial increase in the crystallite size as probed by the Scherrer equation. Therefore, it can be concluded that Ni_2P nanoparticles are sintered on the silica support under catalytic conditions (hydrogen atmosphere and high temperature/pressure). Moreover, the smallest size Ni_2P pre-catalyst also shows some degree of conversion to the metal rich $Ni_{12}P_5$ phase, indicating a loss of some phosphorous under these reducing conditions.

3.3.4. Preliminary Size Dependent DBT HDS Activity of Ni_2P/ASA and Ni_2P/γ-Alumina Catalysts

We assumed that sintering of Ni_2P nanoparticles occurs due to the weak interaction between Ni_2P nanoparticles and the silica support. Therefore, we explored the use of two other supports, γ-Alumina and ASA (hybrid of γ-Alumina and silica), assuming better interaction between particles and support would occur through $AlPO_4$ linkages. However, DBT-HDS catalytic activity of Ni_2P nanoparticles with average size of 15.8 nm supported on γ- alumina and ASA are significantly lower than that of Ni_2P/silica catalyst with average size of 15.6 nm as shown in Figure 3.8. Evaluation of the catalysts by PXRD after HDS testing suggests a degree of sintering comparable to or greater than that observed with silica as a support (Figure 3.9). Thus, interaction between Ni_2P nanoparticles and the alumina containing supports generated by incipient wetness is even weaker than with silica. Accordingly, all further studies focused on Ni_2P/SiO_2 composites.

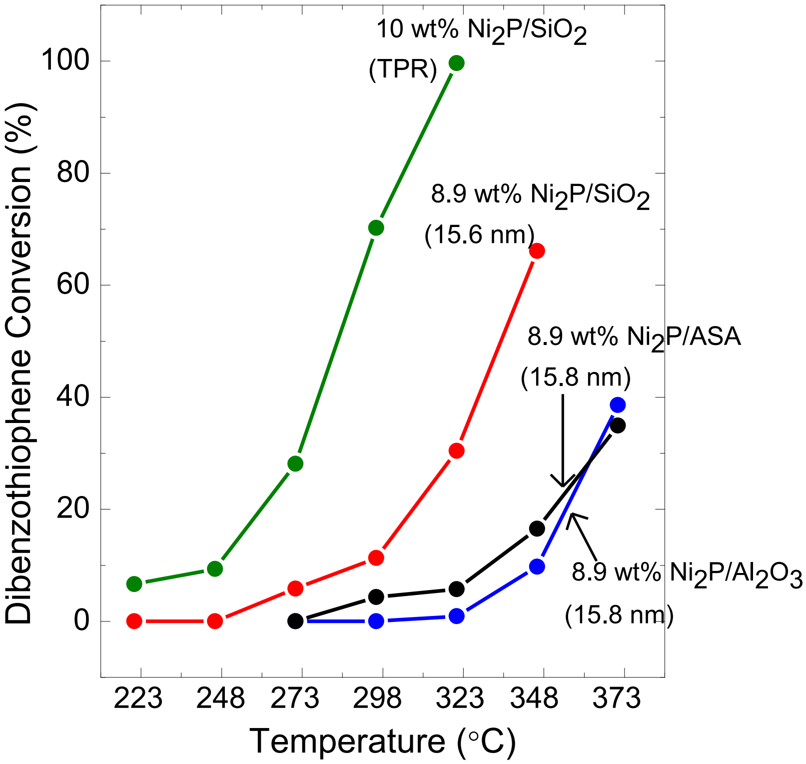

Figure 3.8. Dibenzothiophene HDS conversion of Ni_2P/ASA and Ni_2P/γ-alumina nanoparticle catalysts compared to Ni_2P/SiO_2 nanoparticle catalyst and TPR generated Ni_2P/SiO_2 catalysts.

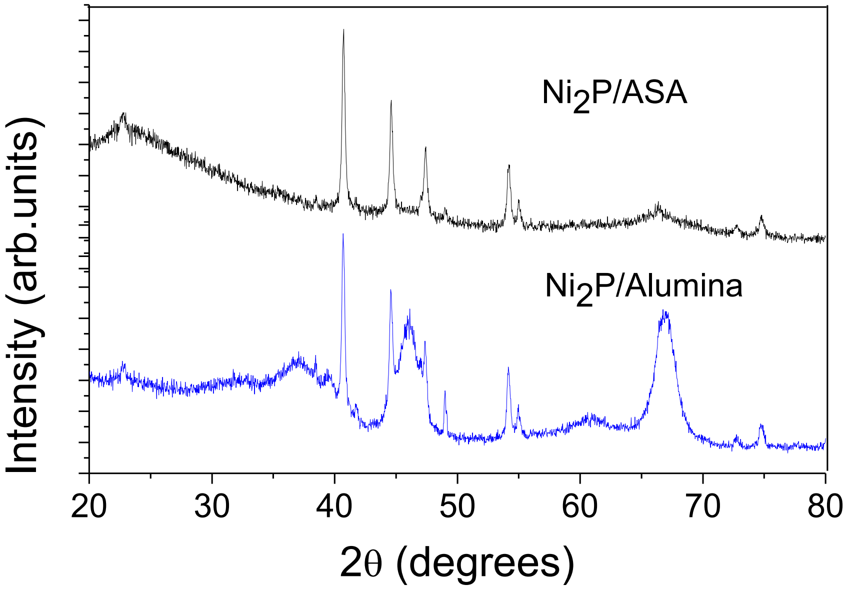

Figure 3.9. PXRD data of post-HDS Ni_2P/ASA and Ni_2P/γ-alumina catalysts.

3.4. Sintering Behavior of Ni_2P/SiO_2 Nanoparticle CatalystS

In order to discern the mechanism of sintering, en route to shutting this pathway down, we studied particle ripening as a function of synthesis and processing conditions. Specifically, we varied impregnation conditions, weight loading, time, and temperature for a ~ 10 nm diameter sample of Ni_2P nanoparticles.

3.4.1. Effect of Impregnation Method on Sintering

The Ni_2P/SiO_2 samples used for preliminary HDS experiments were prepared by a one-step impregnation method where 100 mg of Ni_2P (10 nm) dispersed in 5 mL of ethanol was impregnated onto 900 mg of silica in one-step. However, one step impregnation might have caused the incipient wetness point of silica to be exceeded (for water, 2.4 cm^{-3}/g) resulting in aggregation of a fraction of Ni_2P nanoparticles on the silica surface. This fraction of Ni_2P nanoparticles could be responsible for the sintering effect observed during HDS. Therefore, we prepared a Ni_2P/SiO_2 (10 nm) precatalyst using stepwise impregnation, where only 1 mL of Ni_2P/ethanol was impregnated into silica per cycle for 5 cycles to achieve complete impregnation. Ethanol was evaporated at 80 °C for 1 hour between subsequent cycles. Stepwise impregnation assures that the incipient wetness point was not exceeded, reducing the possibility of particle aggregation on the silica surface during drying. However, Ni_2P/SiO_2 samples prepared using the two different impregnation methods showed the same degree of sintering (peak sharpening in the PXRD (Figure 3.10)) when they were heated to 400 °C in the presence of a 5% H_2/Ar mixture in a flow furnace for 2.5 h. The average crystallite size (Scherrer equation) increased in each case from 10 nm to > 20 nm upon heating. This is confirmed by TEM taken for the sample made by stepwise impregnation, where a majority of particles have grown from their original size to a larger size (in this case from ca. 10 nm to ca. 20 nm) as seen in Figure 3.11**.**

In addition, a few particles have grown to even larger size (ca. 32 nm) and some particles have not grown or sintered and retain their original size of ca. 10 nm. TEM imaging of samples prepared by one-step impregnation and heated at 400 °C revealed similar behavior.

These data suggest that sintering of particles occurred due to the physical transport of particles (not due to aggregation or close proximity of particles in the pre-catalyst) throughout the silica matrix, and thus the impregnation method has little or no effect on the resultant sintering. As observed in post-HDS samples, there is also some degree of phosphorus loss in the one-step impregnated Ni_2P/SiO_2 sample as reveled by the appearance of a small PXRD peak due to $Ni_{12}P_5$ upon heating under H_2 at 400 °C for 150 minutes (Figure 3.10).

In order to improve the interaction between the Ni_2P nanoparticles and the silica substrate, $Ni^{2+}$and HPO_4^{2-} ions were deposited onto the silica surface using the incipient wetness method prior to the introduction of Ni_2P nanoparticles. It was expected that the ions would serve to link the phosphide to the oxide support and thus prevent particle transport. However, upon treating at high temperature in a reducing atmosphere, we observed a similar extent of sintering of Ni_2P nanoparticles relative to samples without introduction of Ni^{2+} and HPO_4^{2-} ions was observed (Figure 3.12).

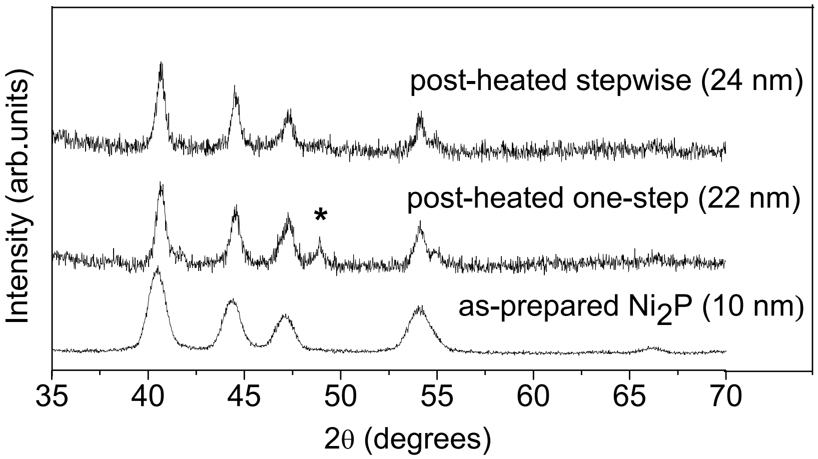

Figure 3.10. PXRD patterns of Ni_2P/SiO_2 samples prepared by stepwise and one-step impregnation methods after heating at 400 °C in the presence of a 5% H_2/Ar flow for 2.5 h. * denotes a peak due to $Ni_{12}P_5$.

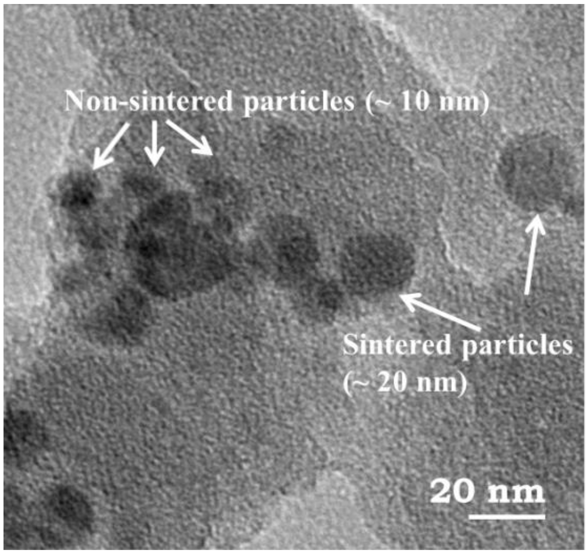

Figure 3.11. TEM image of a Ni_2P/SiO_2 (10 nm) sample (prepared by step-wise impregnation) after heating at 400 °C under H_2 flow for 2.5 h.

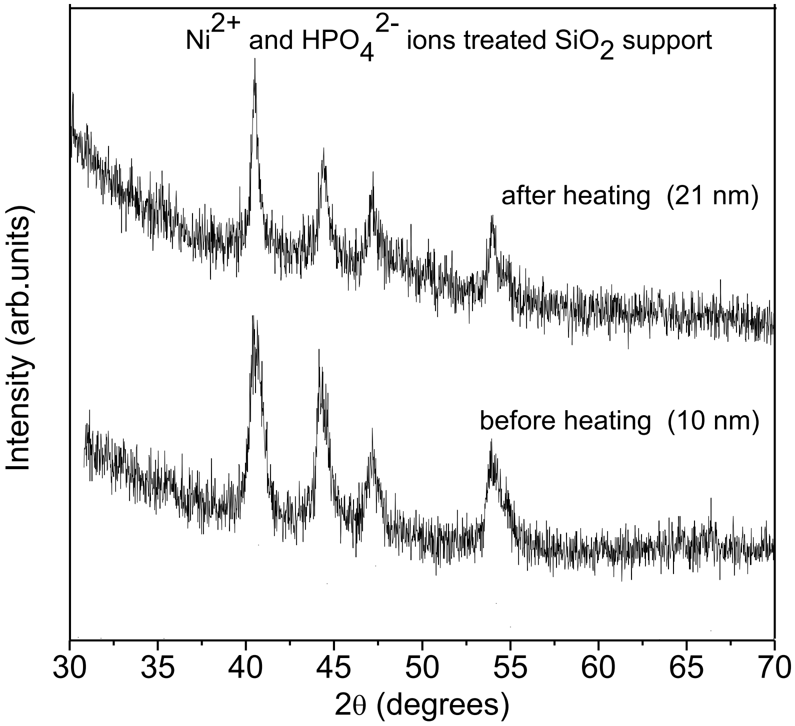

Figure 3.12. PXRD patterns of Ni_2P/SiO_2 precatalyst sample before heating and after heating at 400 °C for 2.5 h. the silica support was treated with Ni^{2+} and HPO_4^{2-} ions before introducing Ni_2P nanoparticles.

3.4.2. Effect of Weight Loading, Time, and Temperature on Sintering

We prepared Ni_2P/SiO_2 precatalysts with varying Ni_2P weight loadings ranging from 2.5 to 20%, in order to study the dependence of the extent of dispersion (loading) of Ni_2P nanoparticles on the sintering behavior under simulated HDS conditions (heating the precatalyst samples at 400 °C for 2 hours under 5%H_2/Ar flow). It was assumed that low wt % of Ni_2P would result in a lesser degree of sintering compared to high wt % samples. However, similar crystallite sizes were obtained for each sample, suggesting that the final crystallite size arising from sintering does not depend on the degree of the loading (Figure 3.13).

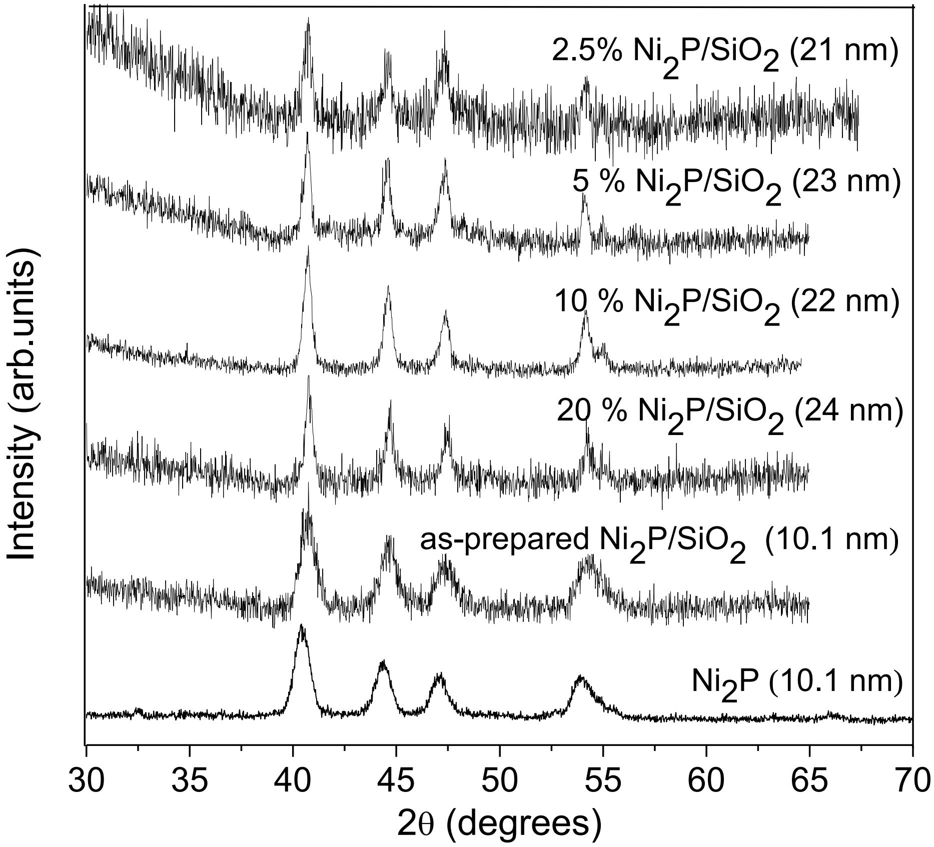

Figure 3.13. PXRD patterns of as-prepared Ni_2P and Ni_2P/SiO_2 precatalyst samples with varying loading percentages before and after heating at 400 °C for 2.5 h under 5% H_2/Ar mixture.

Likewise, sintering does not depend on the amount of time the catalyst is subjected to a reducing atmosphere at high temperature. A 10 wt% Ni_2P/SiO_2 sample was divided into three portions and heated under our simulated HDS conditions for different time intervals ranging from 30 minutes to 6 hours. The PXRD patterns of the samples after reduction indicate that particles have grown from 10 nm to 20-25 nm in each case (Figure 3.14). The similar crystallite sizes of samples heated for 30 minutes and 6 hours suggest that the sintering of particles happens quickly and acquires its energy-minimized size within 30 minutes. Therefore, it can be concluded that time is not a determining factor in the sintering.

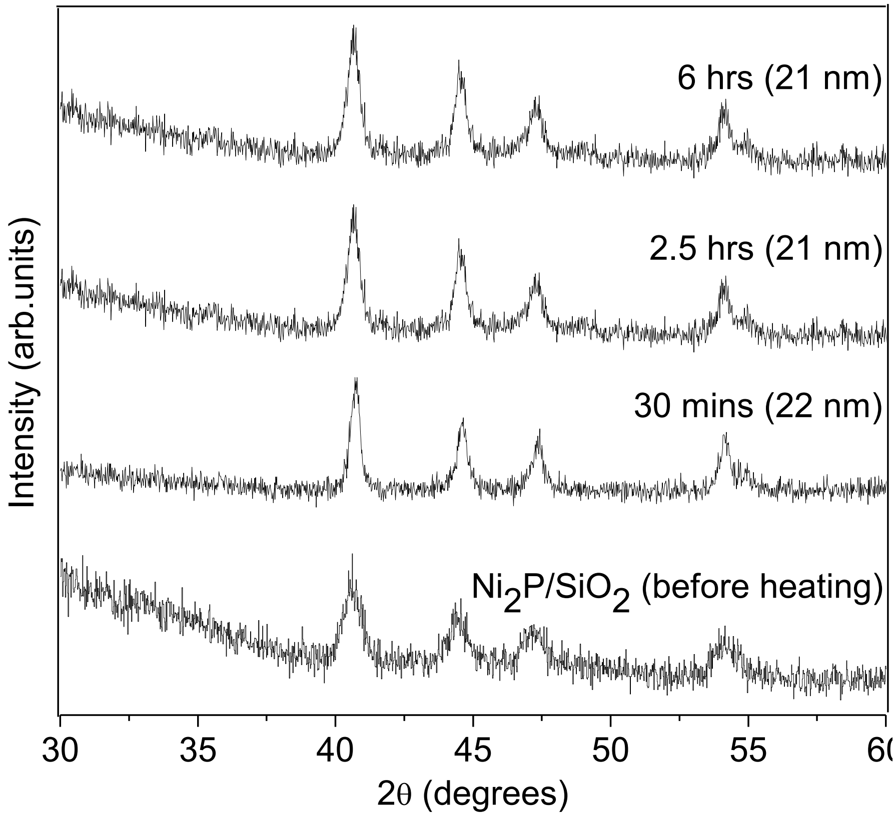

Figure 3.14. PXRD patterns of a Ni_2P/SiO_2 precatalyst sample before heating and after heating at 400 °C under a 5% H_2/Ar flow mixture at varying time intervals.

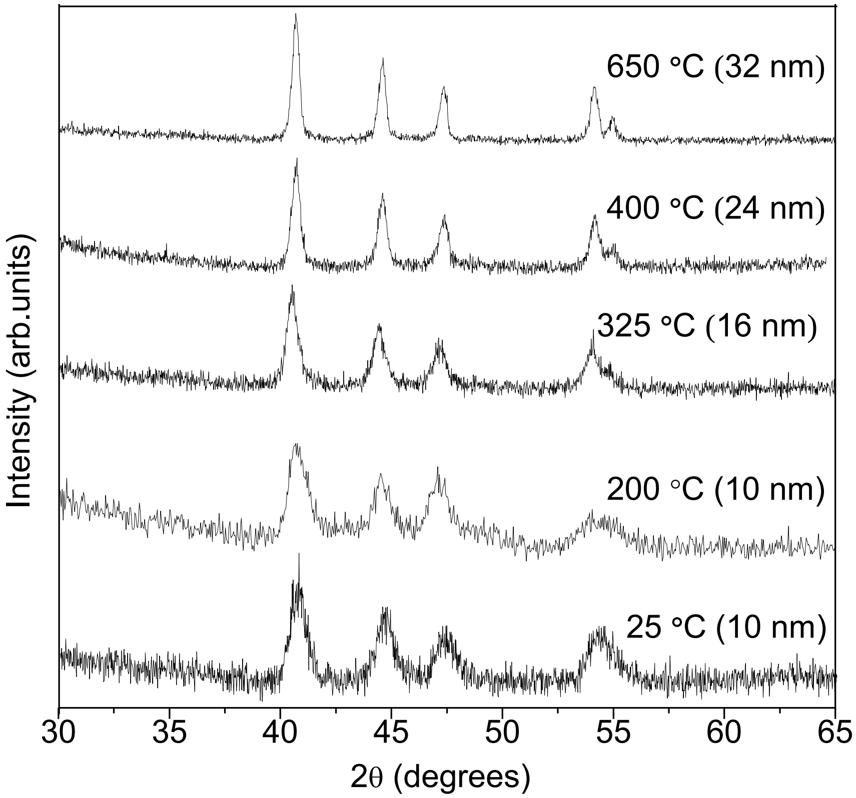

Figure 3.15. PXRD patterns of a Ni_2P/SiO_2 precatalyst sample after heating at varying temperatures ranging from 200 °C to 650 °C for 2.5 h.

Temperature appears to be the only factor capable of controlling sintering in the reaction. Figure 3.15 shows PXRD patterns obtained for a Ni_2P/SiO_2 sample after heating at varying temperatures (200 °C – 650 °C) for 2.5 h in the presence of a 5% H_2/Ar flow. It was hypothesized that the particle size would increase as the temperature increases due to the fact that the particles are more mobile (kinetics). As expected, an increase of the crystallite size can be observed from the temperature series shown in Figure 3.15. In addition to the Ni_2P nanoparticles being more mobile, the high surface potential energy gain at high temperature may drive the small particles to grow into bigger particles. [71,72] Apparently, at 200 °C there is limited mobility, or the surface energy of the system is not high enough to exceed the activation energy barrier of sintering for Ni_2P nanoparticles, since no increase in crystallite size is observed. The gradual increase in final crystallite size between 200 °C and 650 °C is consistent with thermal energy being the driving force in the sintering phenomena. These data suggest that sintering cannot be avoided during HDS catalysis for Ni_2P nanoparticles incorporated on to silica using the incipient wetness method because catalytic conditions require a reducing atmosphere and for the temperature to be in the range 300-400 °C.

3.5. Shape Dependent HDS Activity Ni_2P Nanorods

The goal of this part of the project is to study the effect of crystal facets of Ni_2P on the HDS activity. Different shapes of single crystal Ni_2P particles (rods), as well as Ni_2P nanorods with different aspect ratios, were prepared to study the effect of a greater surface area of one facet over another on HDS activity.

3.5.1. Synthesis and Characterization of Ni_2P Nanorods with Varying Aspect Ratios

Figure 3.16 shows a PXRD spectrum of a Ni_2P nanorods sample. As nanorod growth takes place, Ni_2P is nucleated/deposited along the growth axis (perpendicular to the c axis) as indicated by sharpening of the (002) peak in the PXRD spectrum.[19] The extent of nanorod growth primarily depends on the available Ni source as shown by TEM in Figure 3.17; the higher the amount of $Ni(acac)_2$ used, the greater the length of the nanorods. The width of the Ni_2P nanorods remains similar in all cases, suggesting that the amount of $Ni(acac)_2$ has no effect in determining the average width (~ 4.5-5.5 nm) of the rods. Therefore, the average length is directly proportional to the average aspect ratio (length to width ratio) of a given nanorod sample. Accordingly, the average aspect ratio could be easily changed from 5-8 to 13-16 nm by changing the amount of $Ni(acac)_2$ used at the beginning of the reaction from 0.5 to 2 mmol (Figure 3.17).

Thus, it is now possible to investigate the crystal facet effects on HDS activity once the ideal support and supporting conditions are understood.

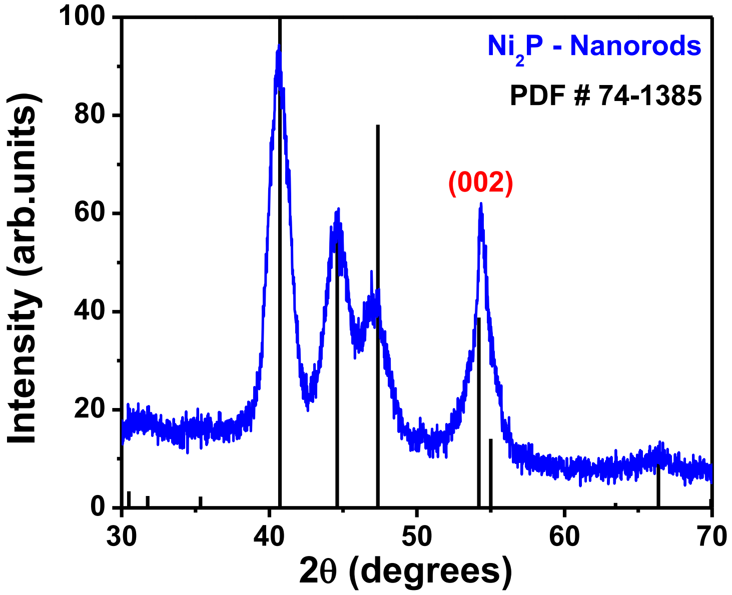

Figure 3.16. PXRD pattern of a Ni$_2$P nanorods sample.

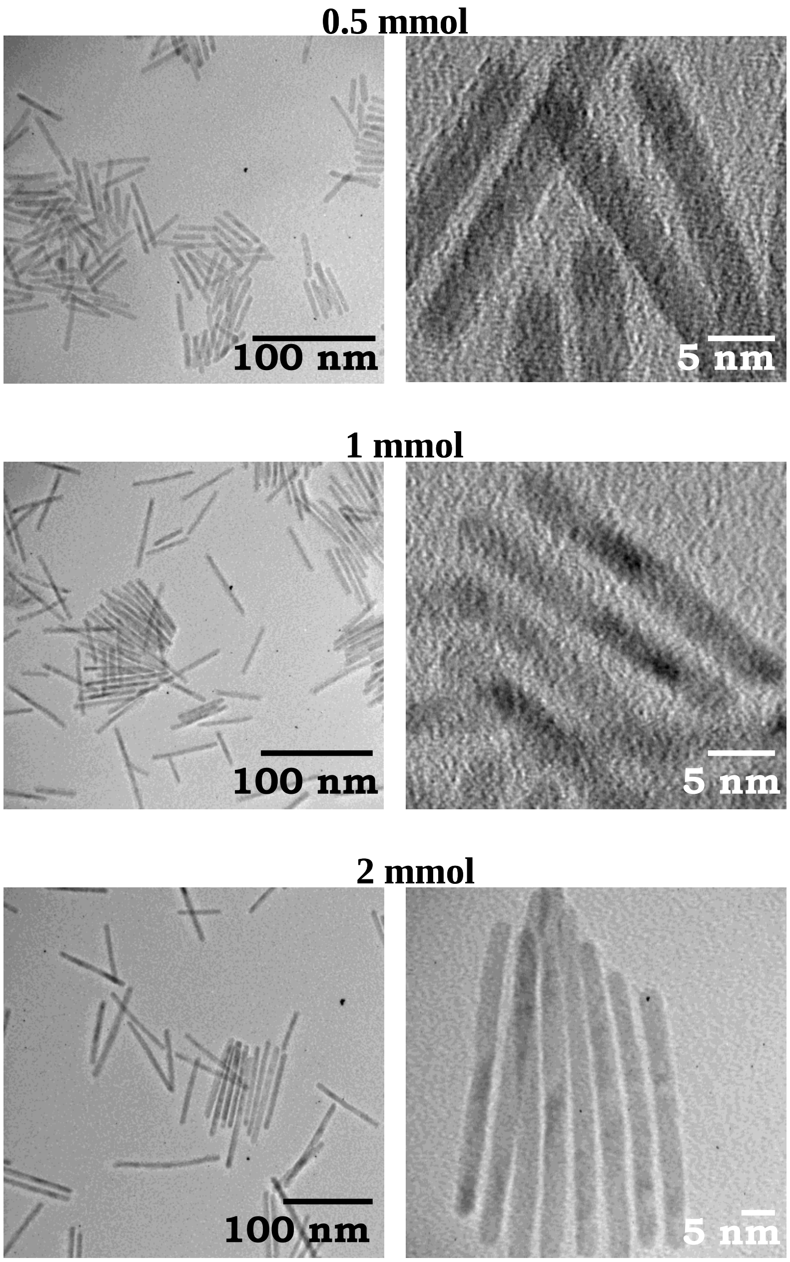

Figure 3.17. Ni_2P nanorods with varying lengths by varying the amount of $Ni(acac)_2$ used (lengths are 29-38, 43-52, and 70-85 nm for 0.5, 1, and 2 mmol of $Ni(acac)_2$ respectively).

3.5.2. HDS Activity of Ni_2P Nanorods

To conduct preliminary HDS activity of a Ni_2P nanorod sample and compare data to nanospheres, rods were dispersed on to the silica support using the incipient wetness method. In this measurement, a Ni_2P nanorod sample with an average aspect ratio of 14.5 was used (average length ~80 and average width 5.5) to target a weight loading of 10% Ni_2P/SiO_2 pre-catalyst. As shown in Figure 3.17, these nanorods tend to arrange parallel to each other in the solution making it difficult to disperse them on to the silica support as discrete rods. TEM images collected for silica supported Ni_2P nanorods also indicate that these rods are severely aggregated on the silica support (Figure 3.18).

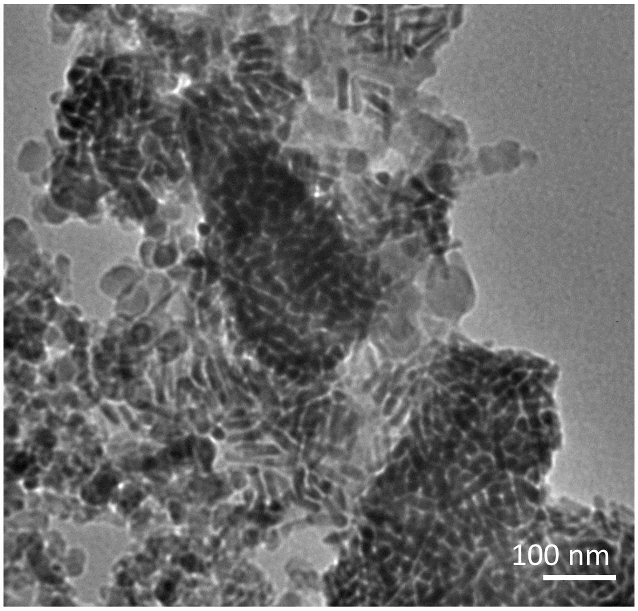

Figure 3.18. TEM image of 10 wt% Ni_2P/SiO_2 nanorods sample prepared by the incipient wetness method.

Figure 3.19 shows the preliminary HDS collected for a 10 wt% Ni_2P/SiO_2 nanorod sample where dibenzothiophene conversion starts at a temperature around 325 °C and increases up to 16% when the temperature reaches 400 °C. This activity is intermediate between that obtained for the 5.5 nm and 10.8 nm spheres (Figure 3.5). The relatively low activity may be due in part to a lower actual wt % loading (this nanorod sample was not quantified by AA) or to sintering.

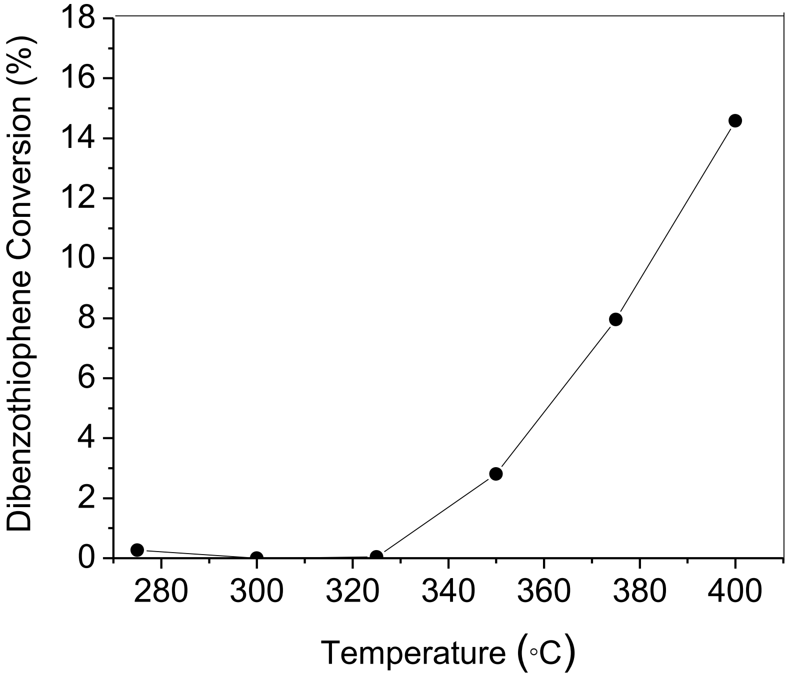

Figure 3.19. HDS data for a 10 wt% Ni_2P/SiO_2 nanorods sample prepared by the incipient wetness method.

3.6. Conclusion

The solution-phase arrested-precipitation method allows for the formation of monodisperse samples of Ni_2P nanoparticles with controlled size selection. The binding and reducing ability of oleylamine has a clear effect on the nucleation rate of Ni-P amorphous precursor particle formation, thus governing the average particle size of the resultant Ni_2P particles. Unfortunately, Ni_2P nanoparticles form only weak interactions with amorphous silica, alumina, or ASA (silica alumina hybrid) supports, resulting in sintering under conditions required to achieve HDS catalysis and consequently in poor activity. Attempts to limit sintering by varying loading, time, incipient wetness steps and ionic attachment were unsuccessful.

With respect to generation of anisotropic Ni_2P nanoparticles, the synthesis of unidirectional Ni_2P nanorods was achieved. The change of length (aspect ratio) is controlled by changing the amount of NiO available for the reaction. This should enable future studies of lattice facet effects on activity once appropriate conditions are identified for supporting the catalyst.

CHAPER 4

LARGE-SCALE SYNTHESIS OF MESOPOROUS SILICA ENCAPSULATED NANOPARTICLES

4.1 Introduction

The application of mesoporous silica shell coatings to chemically different nanoparticles has shown great benefits in applications in the areas of catalysis,[13, 73-75] bioimaging,[76-83] drug delivery,[76,80,83] and nanocomposite formation.[81, 8484-88,89-91,92,89] With respect to heterogeneous catalysis, a key problem is aggregation/sintering of catalytic particles at high temperature, resulting in loss of activity.[71] Encapsulation of nanoparticles in a mesoporous silica shell provides thermal protection to metallic nanoparticles such as Pt, used for ethylene hydrogenation and CO oxidation reactions, avoiding sintering at high temperature (~ 700 °C), yet facilitating the movement of reactant and product molecules to and from the catalytic surface through the porous shell.[13, 75] Given the issues encountered with sintering of Ni_2P nanoparticles, we sought to use mesoporous silica to enable size dependent HDS to be studied. As Ni_2P nanoparticles are capped with organic ligands such as oleylamine and TOP, Ni_2P nanoparticles dispersed in chloroform are transferred in to an aqueous medium using cetyltrimethylammonium bromide (CTAB) dissolved in water. The CTAB acts as a pore templating agent. After basifying the medium using NaOH, the silica encapsulation reaction is carried out using tetraethylorthosilicate (TEOS) as the Si source.

There are several challenges for the successful encapsulation of nanoparticles within a mesoporous silica shell. Usually, in-situ silica polymerization around nanoparticles is a slow process requiring hours to days to go to completion. For example, Gorelikov et. al also showed that Au nanorods and CdSe/ZnS can be coated with mesoporous silica by using concentrated

CTAB solutions, but this takes up to 500 hours.[90] In addition, this approach can be challenging for nanocrystals that are susceptible to dissolution at the high pHs needed for silica formation. Moreover, existing literature preparations employ small concentrations of silica source and nanoparticles, yielding small amounts of the product.[84,89, 90] Finally, to date there is no report describing the control of the weight percentage of core particles in the in-stu mesoporous silica encapsulation, which is a very important parameter in heterogeneous supported catalysts where the catalytic activity depends on the active catalyst weight percentage.

In order to exploit this methodology for development of catalysts or other applications (e.g., combined imaging and drug delivery agents), a systematized, general methodology that enables large-scale, rapid production of material with controlled loading is needed. In this dissertation study, we carried out a series of small scale reactions by varying conditions such as pH, time, and TEOS concentration to understand the in-situ silica encapsulation process around Ni_2P nanocrystals. This is be the first study showing the in-situ mesoporous silica encapsulation of any kind of metal phosphide particles. Moreover, a strategy to extend the small scale mesoporous silica supported particles route to a large scale synthesis (milligrams to grams) will also be discussed. Most importantly, the control of the weight percentage of core nanoparticles is also achieved with the large scale synthesis. The effect of size on HDS catalytic activity is probed for the first time. The generality of the method is demonstrated by application to CdSe and Au nanoparticles.

I collected all data in this chapter with the exception of HDS catalytic data which were collected in Bussell lab in department of chemistry at western Washington University.

4.2 Experimental Section

All chemicals used for the synthesis described in this chapter are listed in Chapter 2.1.

4.2.1 Synthesis of Ni_2P Nanoparticles

The synthesis of Ni_2P nanoparticles was carried out by following the procedure described in Chapter 3.2.1.

4.2.2 Synthesis of CdSe Nanoparticles

A mixture of 0.4 mmol of cadmium oxide, 0.56 mmol of 1-tetradecylphosphonic acid and 20 mmol of trioctylphosphine oxide were heated to 330 °C under argon flow. After the solution became colorless, the temperature was reduced to 150 °C and a solution of selenium containing 0.52 mmol of selenium powder in 10 mL of trioctylphosphine was injected. The temperature of the mixture was then increased up to 250 °C at a rate of 10 °C per 10 minutes and the QDs were grown for four hours.

4.2.3. Synthesis of Au Nanoparticles

5 mL of 1mM $HAuCl_4$ solution and 5 mL of 1mM sodium citrate ($Na_3C_6H_5O_7$) was mixed in a 50 mL beaker. An aqueous solution of 0.1 M of $NaBH_4$ was prepared and cooled in an ice bath. 2 mL of freshly prepared $NaBH_4$ was then added to the Au^{3+}-containing solution under vigorous stirring to yield Au nanoseeds.

4.2.4. Optimization of Mesoporous Silica Encapsulated Ni_2P ($Ni_2P@mSiO_2$)

Wet Ni_2P nanoparticles (~ 150 mg dry weight) produced from 2 mmol $Ni(acac)_2$ using the synthesis method described in Chapter 3.2.1 were dispersed in 10 mL of $CHCl_3$ and sonicated for 20 minutes. 1 mL (~ 15 mg) of the $CHCl_3$ dispersed Ni_2P nanoparticles was added to 5 mL of an aqueous CTAB solution drop-wise under vigorous stirring at room temperature. The $CTAB/H_2O/Ni_2P/CHCl_3$ mixture (brownish-cloudy) was then heated slowly to 75 °C and kept for 20-30 minutes to remove the $CHCl_3$ from the system. Upon removing $CHCl_3$, the dispersion appeared a black and more transparent. The CTAB/H_2O/Ni_2P mixture was then diluted with 10 mL of nanopure H_2O. The pH of the reaction mixture was adjusted/optimized by adding 0.1 mL of varying concentrations (0.25, 0.5, and 1 M) of NaOH solutions. Then a varying amount of TEOS (0.1, 0.3, and 1 mL) was added to the 15 mL volume of the CTAB/H_2O/Ni_2P mixture at 50 °C. The in-situ mesoporous silica encapsulation of Ni_2P nanoparticles was then carried out for different time intervals.

4.2.5. Scaled-up Ni_2P@$mSiO_2$ Synthesis with Controlled Loading

Wet Ni_2P nanoparticles (~ 150 mg (dry weight)) were dispersed in 5 mL of $CHCl_3$ and slowly added to 40 mL of a 0.1 M CTAB solution. $CHCl_3$ was evaporated by heating the mixture at 75 °C for 20-30 minutes until the dispersion became clear and black. The CTAB/H_2O/Ni_2P mixture was then diluted by adding an extra 160 mL of nanopure H_2O. The diluted CTAB/H_2O/Ni_2P mixture was then basified by adding 2.5 mL of 1 M NaOH. The Ni_2P weight loading was changed by injecting varying amount of TEOS (2, 2.5, 3, and 4 mL). The in-situ mesoporous silica encapsulation of Ni_2P nanoparticles was carried out for 10-15 minutes at 50 °C.

4.2.6. Scaled-up CdSe@$mSiO_2$ Synthesis

Wet CdSe nanoparticles (~ 75 mg (dry weight)) formed from 4 mmol of CdO were dispersed in 5 mL of $CHCl_3$ using sonication. $CHCl_3$-dispersed CdSe nanoparticles were slowly added to 20 mL of a 0.1 M CTAB solution while vigorously stirring. After evaporation of $CHCl_3$ from the system, the CTAB/H_2O/CdSe mixture was then diluted by adding an extra 160 mL of nanopure H_2O. The in-situ silica encapsulation was carried out as described in Chapter 4.2.5.

4.2.7. Scaled-up Au@mSiO_2 Synthesis

The Au nanoseeds solution prepared as described in Chapter 4.2.3 was added to 20 mL of a 0.1 M CTAB solution under vigorous stirring. The CTAB/H_2O/Au mixture was then diluted by adding an extra 160 mL of nanopure H_2O. The in-situ silica encapsulation was carried as described in Chapter 4.2.5.

4.2.8. HDS Activity Measurements for Ni_2P@mSiO_2 Catalyst

Dibenzothiophene HDS activity of Ni_2P@mSiO_2 catalysts were measured by the Bussell group at Western Washington University using the method described in Chapter 3.2.4.

4.3 Result and Discussion

A Ni_2P nanoparticle sample with an average size of 10.7 nm was prepared by our reported synthetic procedure for the purpose of making Ni_2P@mSiO_2 on a small scale. In order to make Ni_2P@mSiO_2, we adapted and modified the original synthetic protocol reported by Gorelikov et. al to synthesize CdSe/ZnS@mSiO_2. They showed that the thickness of the silica coating is time dependent; thus, it takes a few days for the completion of silica polymerization. Moreover, the synthesis of CdSe/ZnS@mSiO_2 was done on a small scale while the particle concentration and the successful phase transfer of CdSe/ZnS into the aqueous medium containing CTAB are two crucial factors affecting the successful formation of CdSe/ZnS@mSiO_2.[90]

To encapsulate the Ni_2P nanoparticles, organic ligand capped Ni_2P nanoparticles dispersed in $CHCl_3$ are mixed with a surfactant (CTAB) dissolved in H_2O. Upon evaporating $CHCl_3$ at 75-80 °C, Ni_2P nanoparticles are trapped in the CTAB micelles by nonpolar-nonpolar interactions between the non-polar chains of CTAB located inside the micelle and the non-polar surface ligands (TOP, oleylamine) on the particle surfaces, while the polar (N^+) group is located outside of the micelle interacting with polar H_2O molecules. Once the Ni_2P-dispersed CTAB/H_2O solution is basified, the silica polymerization is carried out by introduction of TEOS. The $Ni_2P@mSiO_2$ product is purified by washing with nanopure water and methanol to remove excess base and byproducts, such as ethanol.

4.3.1. Effect of CTAB Concentration

The concentration of aqueous CTAB plays a major role in the successful phase transfer of Ni_2P nanoparticles capped with oleylamine and TOP from the $CHCl_3$ (non-polar) to the aqueous (polar) medium. When we used low concentration CTAB solutions (< 0.05 M), no Ni_2P nanoparticles were incorporated into CTAB micelles, and hence no Ni_2P particles were detected in the silica matrix once the silica polymerization was carried out. However, use of a high concentration CTAB solution (0.1 M), enabled dispersion of Ni_2P nanoparticles in the aqueous medium contributing to successful in-situ silica polymerization around the Ni_2P nanoparticles.

4.3.2. pH Dependence on Silica Polymerization and Stability of Ni_2P Nanoparticles

Silica polymerization is a pH dependent process that proceeds faster at higher pH. However, Ni_2P nanoparticles are susceptible to etching at high pH. In order to understand the optimum pH needed for the formation of $Ni_2P@mSiO_2$ and the stability of Ni_2P nanoparticles, we varied the pH of the medium and studied $Ni_2P@mSiO_2$ using TEM.

The CTAB/H_2O/Ni_2P mixture prepared from ~ 15 mg nanoparticles and 5 mL of aqueous CTAB was diluted with 10 mL of nanopure H_2O. The pH of the reaction mixture was adjusted/optimized by adding 0.1 mL of varying concentration (0.25, 0.5, 1, and 2M) NaOH solutions and the reactions were performed for 3 h at 50 °C.

As shown in Figure 4.1, it is not just the formation of $Ni_2P@mSiO_2$, but also the dispersion and stability of Ni_2P nanoparticles that depends on the pH of the reaction medium. At the lowest pH studied, 11.2, most of the Ni_2P nanoparticles were arranged in a very ordered and two dimensional pattern within silica cages. Aside from these Ni_2P assemblies, the majority of silica has been formed without any Ni_2P nanoparticle incorporation. However, Ni_2P nanoparticles are quite stable at pH=11.2; the particles remain spherical and very similar in size (10.7 nm) to the original as-prepared Ni_2P nanoparticles. As the pH of the medium is increased to 11.5, more and more discrete Ni_2P particles are incorporated into the silica matrix. However, we still observe regions where a number of Ni_2P particles are packed very close to each other in the silica. As we further increased the pH to 11.8, complete dispersion of Ni_2P nanoparticles (no Ni_2P particle aggregates) into the silica matrix is observed. Furthermore, Ni_2P nanoparticles are distributed evenly throughout the mesoporous silica matrix. However, we notice a slight reduction of the particle size to ~ 8 nm and deformation of the spherical shape, when compared to the original 10.7 nm Ni_2P nanoparticles employed in the reaction. This observation suggests that even though we achieved successful incorporation of Ni_2P nanoparticles at pH = 11.8, our Ni_2P nanoparticles are dissolving to some extent at this high pH. This hypothesis is further supported by the TEM analysis done on the reaction carried out at pH=12.2 where no Ni_2P nanoparticles were detected inside or outside the silica matrix. In this reaction, we visually observed the disappearance of the black color (ascribed to Ni_2P) after 3 hours, and the product we recovered is exclusively silica (white).

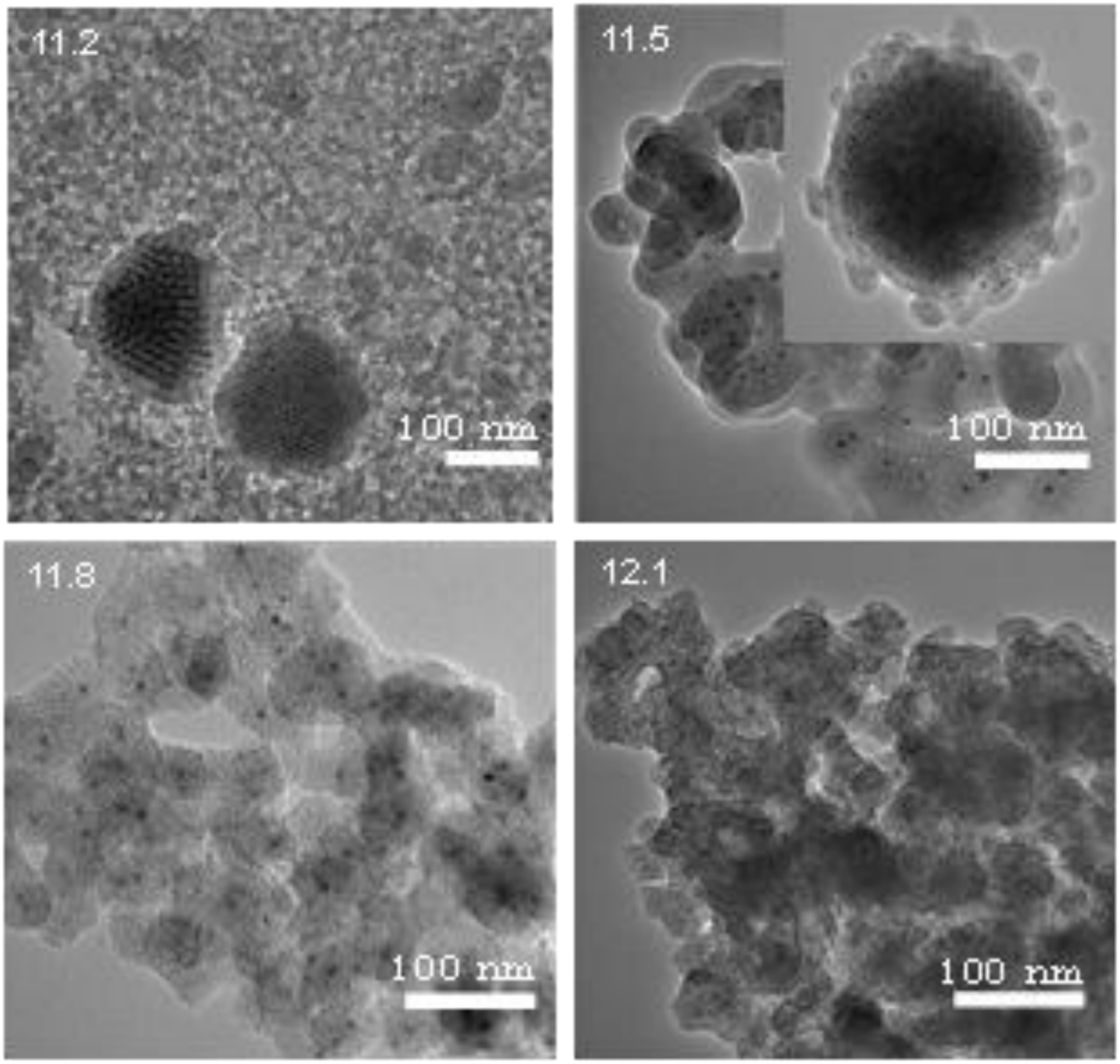

Figure 4.1. A series of TEM images showing the formation of in-situ mesoporous silica around Ni_2P nanoparticles performed at 50 °C for 3 hours at varying pH values (noted in the upper left hand corner of each panel) in the medium.

4.3.3 Effect of Time

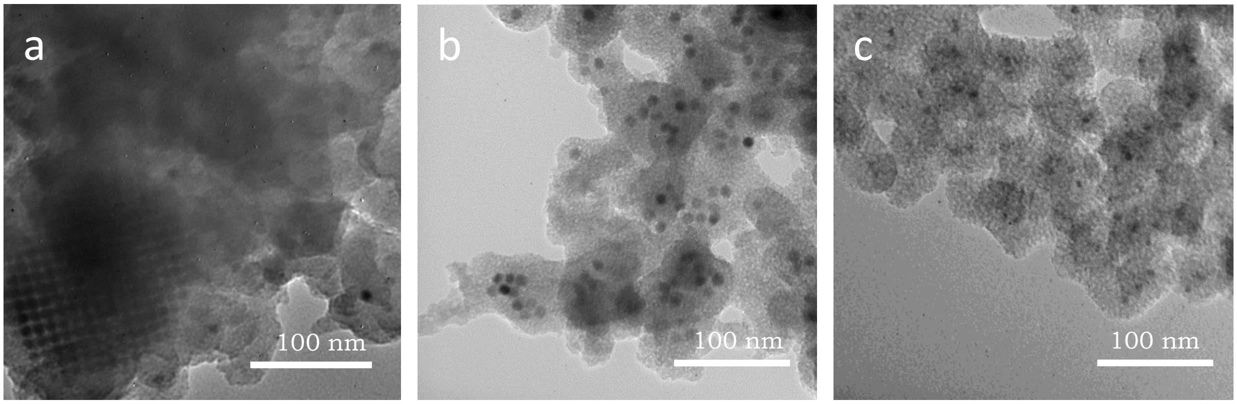

Figure 4.2. TEM images of the reactions carried out for different time intervals at pH=11.82: 15 mins (a), 1 hour (b), and 3 hours (c).

In order to reduce the etching, we next studied the effect of shorter times on $Ni_2P@mSiO_2$ formation and Ni_2P dissolution at pH = 11.8 at 50 °C. As shown in Figure 4.2, Ni_2P nanoparticles are stable, and maintain their spherical morphology and the original size (10.7 nm) up to 1 hour. However, they form large scale aggregates at shorter times (15 min) and begin to dissolve and lose their spherical morphology at 3 hours. Therefore, it can be concluded that in order to maintain the stability of Ni_2P nanoparticles without dissolution and achieve complete dispersion of Ni_2P nanoparticles throughout the matrix, mesoporous silica encapsulation should be conduct at pH=11.8 for ~ 1 hour. The observation of highly ordered Ni_2P nanoparticles in a silica cage even at pH=11.8 suggests that the mesoporous silica formation proceeds through these big, compact and ordered structures prior to dispersion within the mesoporous silica matrix. Indeed, when we carried out the reaction at pH=12.22, it first forms these highly ordered Ni_2P structures (Figure 4.3) within a few minutes. However, before Ni_2P nanoparticles are distributed throughout the silica matrix, they are rapidly dissolved. Based on these data, we can conclude that dispersion of ordered aggregates is both a time and pH-dependent phenomena.

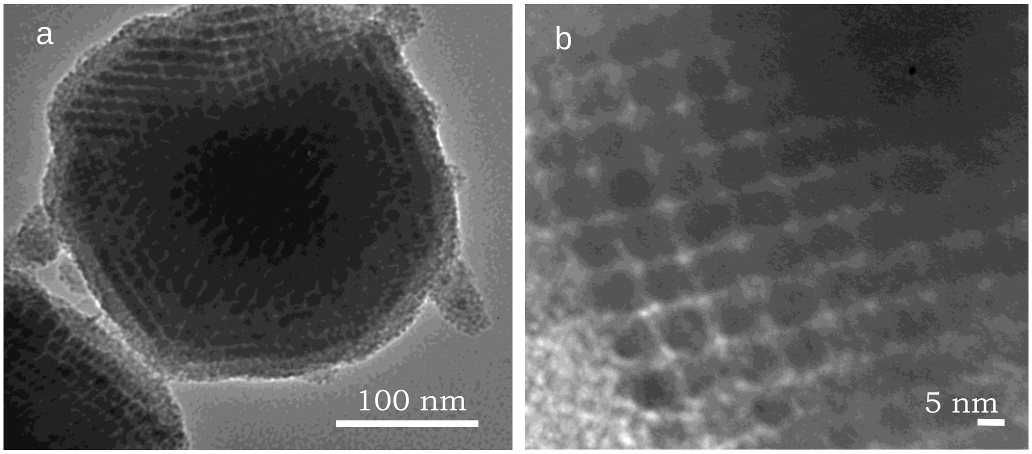

Figure 4.3. Low magnification (a) and high magnification (b) TEM images of highly ordered, compact, and large assemblies of Ni_2P nanoparticles formed at pH = 12.2 after 10-15 minutes.

4.3.4 Scaling up the Ni_2P@$mSiO_2$ Synthesis with Controlled Ni_2P Loading

As we learned from our systematic study of the small scale Ni_2P@$mSiO_2$ synthesis, various parameters such as CTAB concentration (optimally 0.1 M), pH (optimally 11.82), and time (optimally 1 hour) affect the stability of Ni_2P nanoparticles and the formation of Ni_2P@$mSiO_2$. In order to test these in-situ mesoporous silica supported materials for HDS catalysis, it is necessary to make them on a large scale. In addition, for heterogeneous catalysis, it is also important to make catalysts with predetermined weight loadings of the active component (Ni_2P) within the support.

As a first attempt to scale up the Ni_2P@$mSiO_2$ synthesis, we tried to increase all the reactants by a factor of 8-10. However, silica polymerization was incomplete (i.e., the yield was low). We observed that the extent of silica polymerization increased with increasing H_2O volumes used to dilute the CTAB/H_2O/Ni_2P mixture after the phase transfer from $CHCl_3$ to the aqueous medium. The addition of H_2O also lowers the concentrations of organic ligand-capped Ni_2P nanoparticles and bulky CTAB. Therefore, we can conclude that lowering of the CTAB and Ni_2P nanoparticle concentration has a pronounced effect on the rate of silica polymerization. Accordingly, we optimized this large scale synthesis while protecting the Ni_2P nanoparticles by adding 160 mL of water for dilution (final volume ~ 200 mL) and 1.5 mL of 1M NaOH solution (pH of the mixture = 11.9). Under these reaction conditions, complete polymerization was achieved after ~ 1 h. A further improvement in the large scale synthesis of $Ni_2P@mSiO_2$ was achieved by using 2.5 mL of 1M NaOH (pH of the mixture = 12.1) for basification, enabling the reaction time to be reduced from 1 hour to 15 min without dissolution of Ni_2P nanoparticles. This observation suggests that the dilution of Ni_2P/CTAB mixture favors the dispersion Ni_2P nanoparticles in the solution since Ni_2P aggregates were not observed even at 15 min.

The reactions listed in Table 1 show that the final yield of $Ni_2P@mSiO_2$ and the weight percentage of Ni_2P can be precisely controlled by changing the amount of Ni_2P nanoparticles and TEOS introduced to the reaction medium. Under these conditions, the Ni_2P nanoparticles are stable; the morphology and shape of the Ni_2P nanoparticles in $Ni_2P@mSiO_2$ are similar to the starting Ni_2P nanoparticles used for this reaction. The weight loading of Ni_2P can also be tuned (~ 10% and ~ 5%) by varying the amount of Ni_2P introduced and maintaining similar amounts of silica formed around the Ni_2P nanoparticles as shown in reactions 1 and 5 in Table 1. Weight loading of Ni_2P can also be tuned by maintaining the amount of TEOS injected and changing the concentration of Ni_2P as shown in reactions 4 and 6 in Table 1.

Table 4.1. Comparison of actual yield and weight percentage (as determined by AAS) with theoretical yield and weight loading.

Reaction number	TEOS (mL)	Theoretical SiO_2 mass (mg)	Introduced Ni_2P mass (mg)	Theoretical $Ni_2P@mSiO_2$ mass (mg)	Actual $Ni_2P@mSiO_2$ mass (mg)	Targeted wt% of Ni_2P	Actual wt% of Ni_2P
1	2.0	540	60	600	580	10	9.7
2	2.5	670	75	745	720	10.1	9.3
3	3.0	820	90	910	880	9.9	9.6
4	4.0	1080	120	1200	1160	10	9.8
5	2.0	540	30	570	540	5.3	5.0
6	4.0	1080	60	1140	1125	5.2	5.0

To our knowledge, this is the first study that enables exquisite control of the catalyst loading onto a support with a yield (~ 100%) of final product by in-situ mesoporous silica encapsulation. Moreover, we can generate the final mesoporous silica supported catalyst in quantities from milligrams to grams easily.

To our knowledge, this is the first study that enables exquisite control of the catalyst loading on to a support with a predetermined yield of final product by in-situ mesoporous silica encapsulation. Moreover, we can generate the final mesoporous silica supported catalyst in quantities from milligrams to grams easily.

4.3.5 Dependence of Ni_2P Weight Loading on $Ni_2P@mSiO_2$ Morphology

Figure 4.4 shows the TEM images collected for $Ni_2P@mSiO_2$ samples having 5 and 10% of Ni_2P weight loading produced using different amounts of TEOS and constant amount of Ni_2P nanoparticles. As the Ni_2P loading (particle concentration) increases, we observe that the morphology of $Ni_2P@mSiO_2$ changes. At lower weight loading, Ni_2P nanoparticles tend be incorporated within discrete mesoporous particles (one Ni_2P nanoparticle in one mesoporous silica particle). In general, as the Ni_2P weight loading is increased, the Ni_2P nanoparticles remain discrete, but are incorporated within a more disperse and matrix-like mesoporous silica. The same is observed when the TEOS concentration is fixed and the Ni_2P nanoparticle concentration varied.

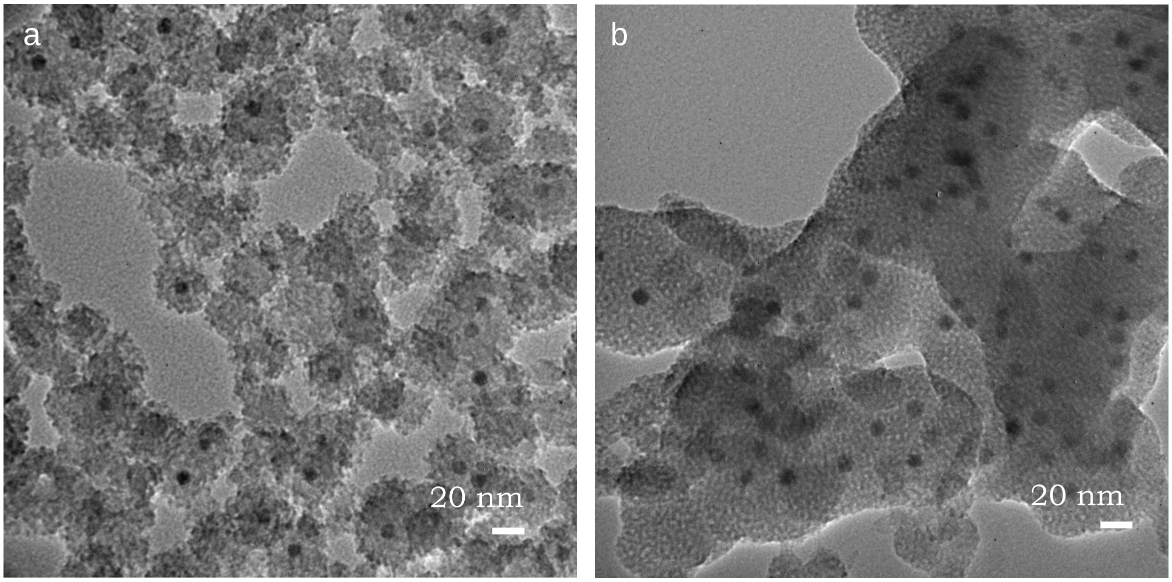

Figure 4.4. TEM images of $Ni_2P@mSiO_2$ (large scale synthesis) with varying percentages of Ni_2P weight loading, 6th reaction -5% (a), and 4th reaction - 10% (b).

4.3.6 Extending the Scaled-up Silica Encapsulation to Other Systems (CdSe and Au NPs)

Importantly, the large-scale synthesis strategy reported here is not limited to Ni_2P but can be extended to the encapsulation of other chemically different nanoparticles (CdSe and Au). Using conditions employed in Table 4.1 reaction number 2 with nanoparticle masses of 100 mg and 75 mg for Au and CdSe, respectively, encapsulation was successfully achieved in high yields. Figure 4.5 (a and b) shows TEM images of CdSe@mSiO_2 and Au@mSiO_2, respectively, prepared using this method. CdSe@mSiO_2 is morphologically similar to Ni_2P@mSiO_2, whereas Au@mSiO_2 produces silica aggregates with the nanoparticles embedded within a continuous silica matrix.

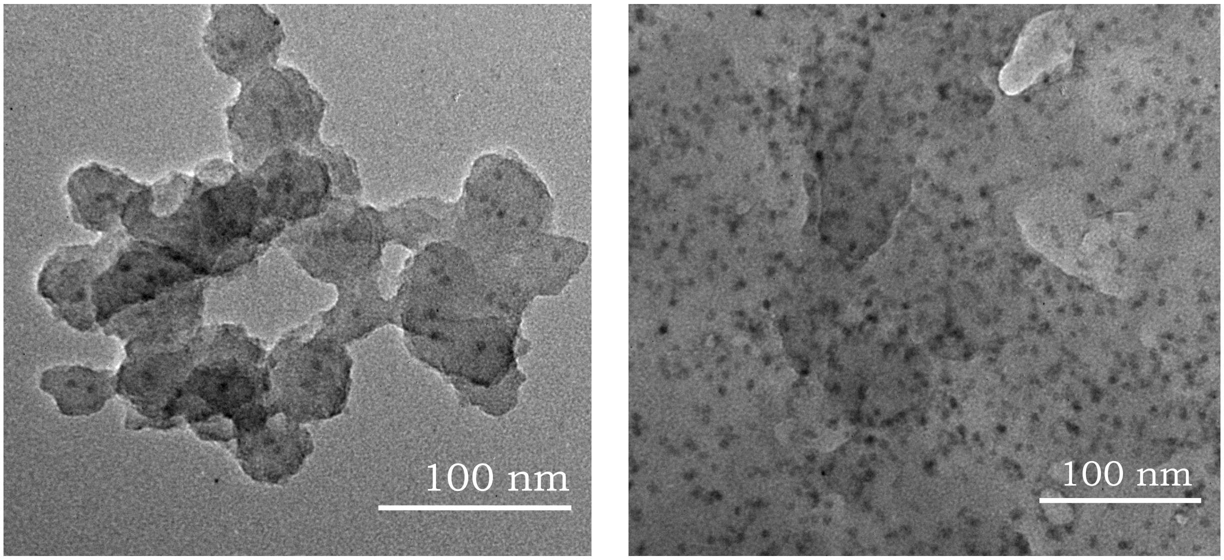

Figure 4.5. TEM images of CdSe@mSiO_2 (left) and Au@mSiO_2 (right).

4.3.7. Template Removal of Ni_2P@mSiO_2

To provide access to the Ni_2P nanoparticle surface, as-prepared Ni_2P/mSiO_2 particles were calcined at 425 °C for 2 hours to remove the CTAB template and any residual organic ligands (oleylamine and TOP) bound to the Ni_2P nanoparticles. TGA analysis of the as-prepared (dried) Ni_2P@mSiO_2 sample shows a weight loss of nearly 35% (Figure 4.6). The calcination step removes the organic component present in the Ni_2P@mSiO_2 sample as evident by the lack of a weight loss above 150 °C (the 4-5% weight loss for the calcined sample up to 100 °C is attributed to adsorbed moisture)

.

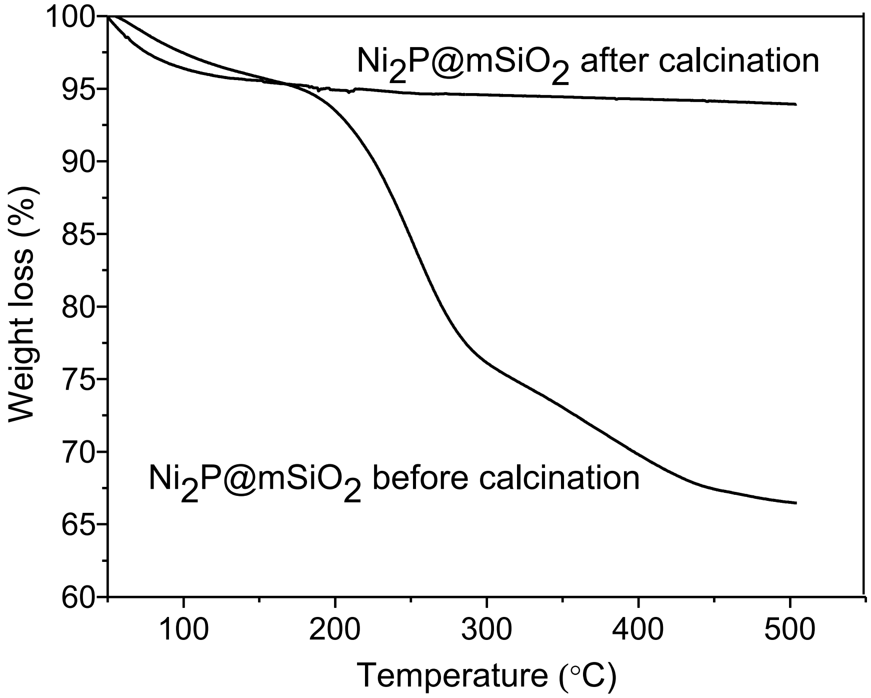

Figure 4.6. TGA data on $Ni_2P@mSiO_2$ samples before and after calcination, collected under oxidizing conditions (air).

In the calcination process, the Ni_2P/SiO_2 sample is significantly oxidized, producing NiO, as revealed by PXRD (Figure 4.7). Importantly, we don't observe any particle sintering during the calcination, as assessed by TEM analysis of the as-prepared and calcined Ni_2P/SiO_2 samples, and the Ni_2P particles maintain their morphology (Figure 4.8). The lack of crystalline reflections corresponding to Ni_2P (Figure 4.7) in calcined $Ni_2P@mSiO_2$ is attributed to the oxidation of Ni_2P to form amorphous NiO and corresponding phosphate/phosphite species.

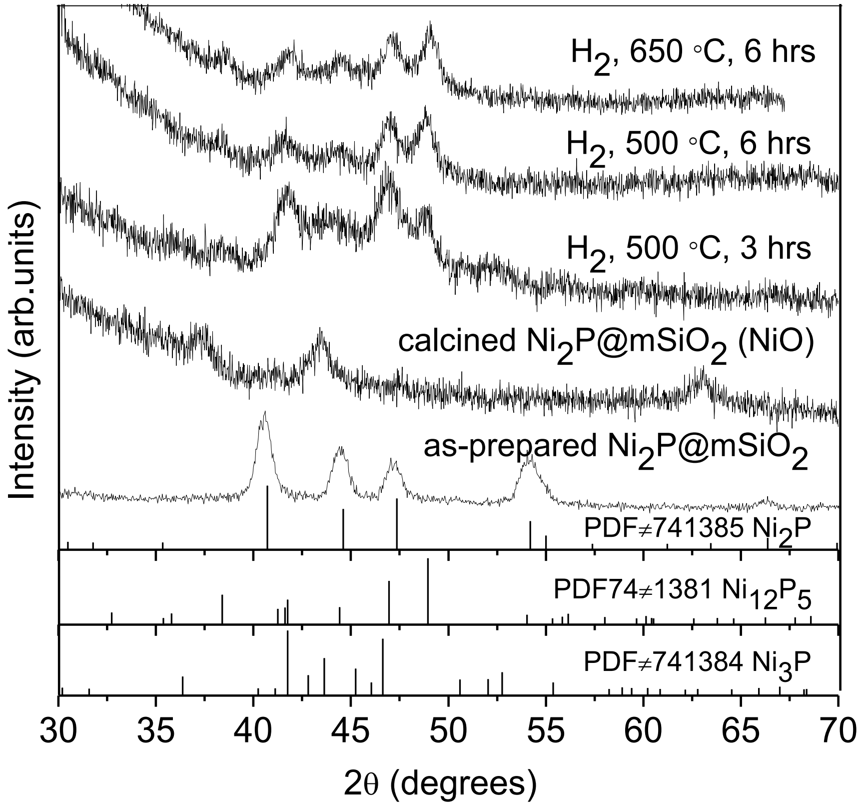

Figure 4.7. PXRD patterns of an as-prepared Ni_2P/SiO_2 (10 nm) precatalyst sample, calcined $Ni_2P/mSiO_2$ sample (converted to NiO), and various post-treated (reduced) calcined samples under 5% H_2/Ar mixture at high temperatures (500 – 650 °C) for varying time intervals (3-6 hours).

4.3.8. Recovery of the Catalytically Active Ni_2P Phase

In order to reduce NiO and the phosphate species back to the Ni_2P phase, we treated the calcined samples at high temperatures (500-650 °C) for 3 to 6 hours under a 5%H_2/Ar flow. However, we observed only a partial conversion of oxidized materials, and the phases formed were a Ni_3P and $Ni_{12}P_5$ mixture (Figure 4.7). The extent of the conversion to more-phosphorous-rich nickel phosphide phases is increased when the calcined samples were reduced at 500 °C for 6 h, resulting in exclusively the $Ni_{12}P_5$ crystalline phase and no Ni_3P (Figure 4.7). Attempts to reduce the samples at higher temperature (650 °C) did not result in any further changes. This suggests a fraction of phosphorus is lost during the calcination step. Attempts to directly remove CTAB and organic ligands bound to the Ni_2P nanoparticles by reducing as-prepared Ni_2P@$mSiO_2$ at 400-500 °C in a 5% H_2/Ar flow were also not successful, resulting in nickel rich phases such as Ni_3P and $Ni_{12}P_5$.

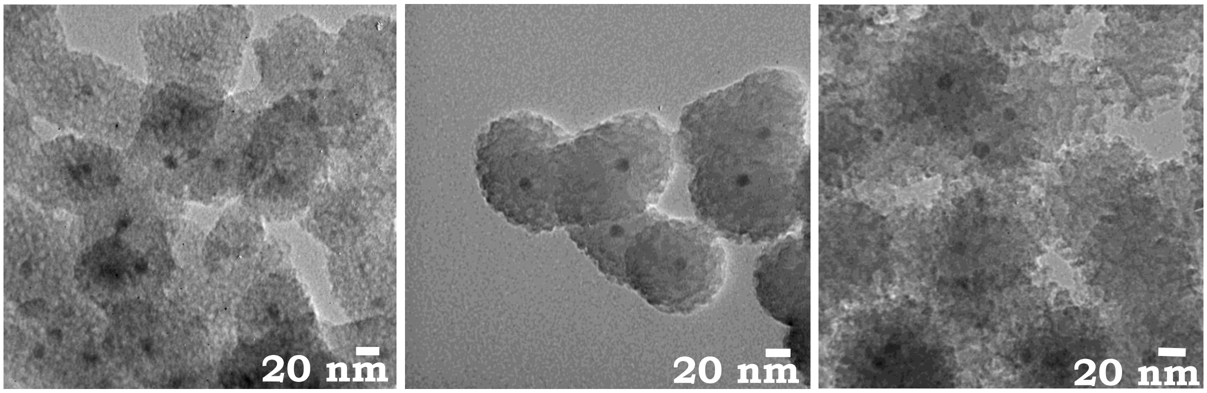

Figure 4.8. TEM images of as-prepared Ni_2P (10.9 nm) @$mSiO_2$ (left), calcined Ni_2P@$mSiO_2$ at 425 °C for 2 hours (middle), and after post-treatment of calcined sample by PPh_3 and 5%H_2/Ar mixture at 400 °C for 150 minutes (right). Note that post treated samples were further heated under a 5%H_2/Ar mixture at 400 °C for 2 hours.

In order to restore the desired phase (Ni_2P), we undertook a post-treatment step. Triphenylphosphine (PPh_3) has previously been shown to act as a phosphorous source under relatively mild conditions in metal phosphide formation.[50, 93-95] Accordingly, PPh_3 vapor was introduced by placing a sample of solid PPh_3 upstream from the calcined $Ni_2P@mSiO_2$ sample under a flow of 5% H_2/Ar at 400 °C for 2.5h. As shown in Figure 4.9, Ni_2P is generated as the only crystalline phase and the crystallite size calculated by the Scherrer equation for post-treated samples (11.2 nm) closely matches the crystallite size calculated for as-prepared $Ni_2P@mSiO_2$ samples (10.9 nm). Intriguingly, regardless of the quantity of PPh_3 used, no phases that are more P-rich (e.g. NiP_2) are observed, suggesting that Ni_2P represents the maximum incorporation of P under these conditions. The TEM images collected for a post-treated sample reveals that Ni_2P particles remain discrete in the mesoporous silica network and the size of the particle remains similar to that of as-prepared $Ni_2P@mSiO_2$ (Figure 4.8). Therefore, encapsulation of Ni_2P nanoparticles within a mesoporous silica matrix enables particle migration and sintering to be significantly limited by physically separating the particles from each other.

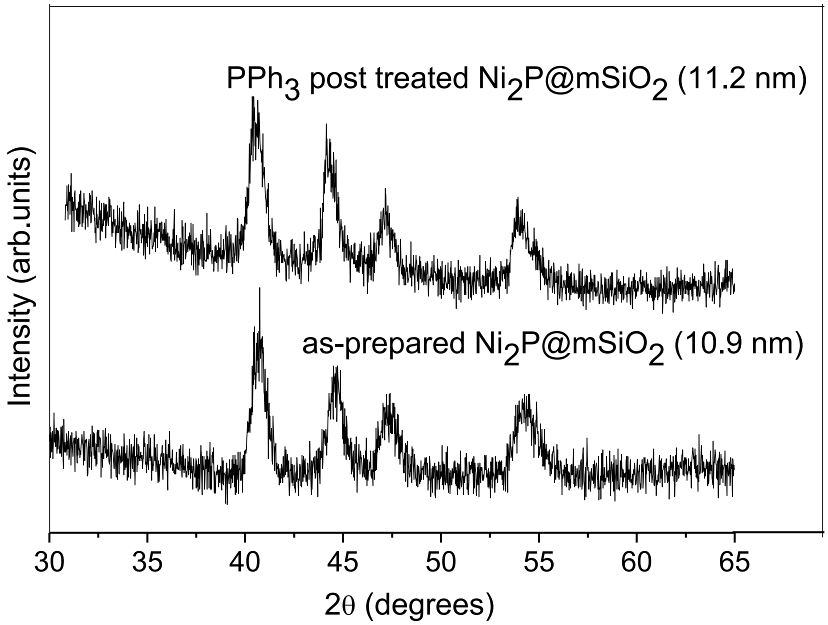

Figure 4.9 PXRD patterns of as-prepared (top) and calcined, post-treated with PPh_3 (bottom) 10 wt% $Ni_2P@SiO_2$ samples.

4.3.9 Physical Properties of the $Ni_2P@mSiO_2$ Catalyst

In catalytic applications, it is very important for reactants and products to have access to the catalysts' surface. The CTAB template and organic ligands can be removed by calcination at 450 °C for 2 hours. After the Ni_2P phase was recovered by performing post treatment using PPh_3. BET surface area and BJH pore size analyses were performed to confirm the mesoporous nature of the silica matrix (Figure 4.10). The BET surface area values are 715 and 610 m^2/g for 5% $Ni_2P@mSiO_2$ and 10% $Ni_2P@mSiO_2$, respectively. The calculated BJH average pore diameter is 5.0 nm for 5 wt% $Ni_2P@mSiO_2$ and 4.8 nm for 10 wt% $Ni_2P@mSiO_2$.

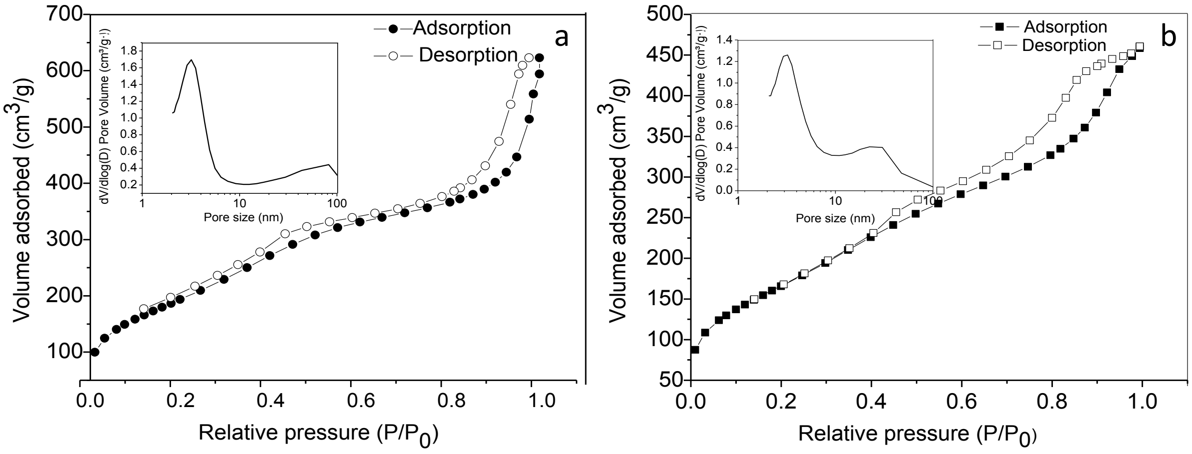

Figure 4.9. Adsorption/desorption isotherms and BJH pore size distributions, calculated using the adsorption branch, of Ni_2P@mSiO_2 prepared by large scale synthesis, 5% wt Ni_2P@mSiO_2 - 6th reaction (a) and 10% wt Ni_2P@mSiO_2 - 4th reaction (b).

4.3.10 Comparison of HDS Activity between Ni_2P/SiO_2 and Ni_2P@mSiO_2

Because sintering of Ni_2P nanoparticles is dramatically reduced for Ni_2P@mSiO_2 catalysts relative to Ni_2P/SiO_2, we expected to achieve enhanced HDS activity relative to the TPR prepared Ni_2P/SiO_2 catalysts described in Chapter 3. As shown in Figure 4.10, the HDS activity of Ni_2P@mSiO_2 nanoparticle catalyst with a particle size of 11.2 nm is dramatically higher than that of the Ni_2P/SiO_2 nanoparticle catalyst (10.8 nm) tested previously. This observation suggests that the minimized sintering enables us to achieve enhanced HDS activity. PXRD analysis on samples after HDS testing reveals minimal sintering (crystallite size increases to 13 nm (Figure 4.11)), vs. 25 nm for incipient-wetness deposited particles (Figure 3.7)).

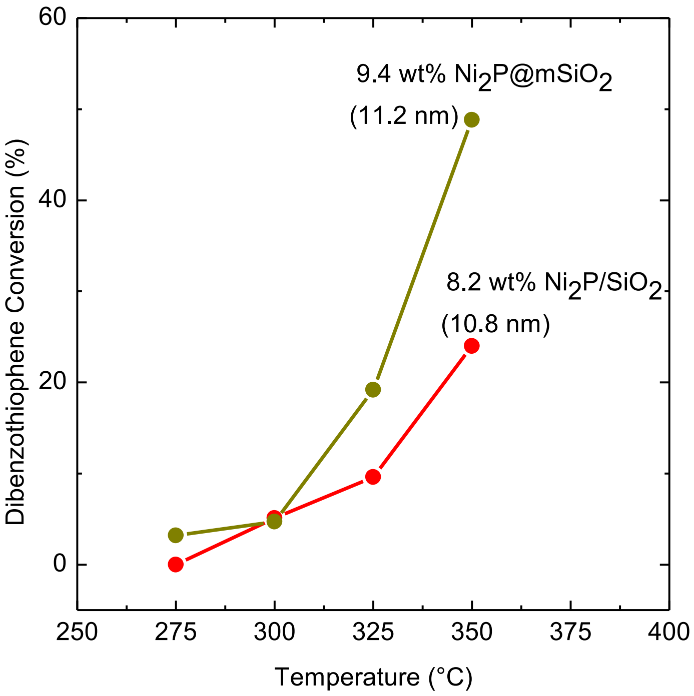

Figure 4.10. Dibenzothiophene HDS conversion, as a function of temperature, of ca 11 nm diameter Ni_2P catalysts encapsulated in mesoporous silica ($Ni_2P@mSiO_2$) or deposited onto a silica support (Ni_2P/SiO_2).

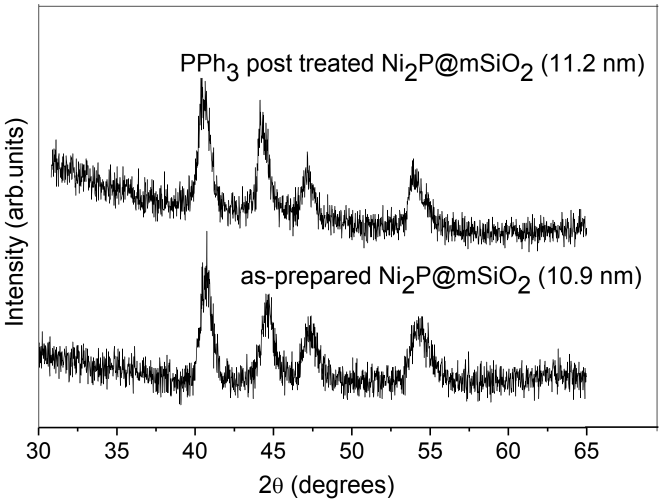

Figure 4.11. PXRD patterns of as-prepared and calcined, post-treated with PPh_3 10 wt% $Ni_2P@SiO_2$ samples.

4.3.11 Size Dependent HDS Catalytic Data for Ni_2P@mSiO_2

In contrast to incipient wetness prepared materials, the trend of size dependent HDS activity shown by Ni_2P@mSiO_2 can be related to the surface area to volume ratio; the HDS activity increases as the particle size decreases (Figure 4.12). Dibenzothiophene (DBT) conversion is ~ 60% for 17.1 nm Ni_2P@mSiO_2 catalyst at 375 °C. At the same temperature, DBT conversion increases to ~ 77% and 95% for 11.2 nm Ni_2P@mSiO_2 and 5.9 nm Ni_2P@mSiO_2 catalysts, respectively.

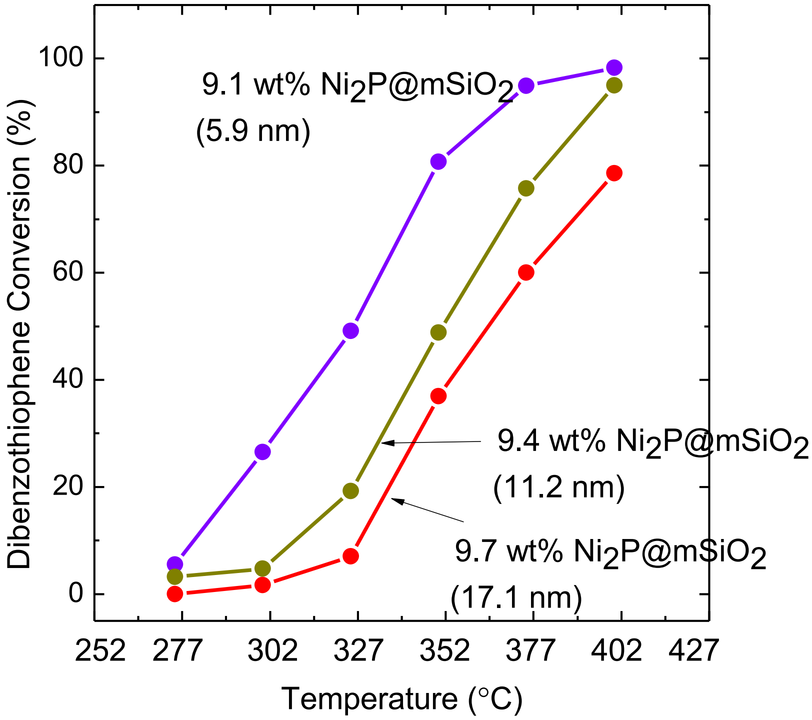

Figure 4.12. Size dependent HDS data of Ni_2P@mSiO_2 catalyst.

Table 4.2 summarizes the crystallite sizes calculated for as-prepared and post-HDS $Ni_2P@mSiO_2$ catalysts employed in measuring size dependent HDS activity of Ni_2P. The Ni_2P average crystallite sizes after HDS indicate no significant particle growth for the 11.2 and 17.1 nm $Ni_2P@mSiO_2$ samples. However, the Ni_2P average crystallite size after HDS for the 5.9 nm $Ni_2P@mSiO_2$ sample indicates substantial particle growth occurs; the crystallites post HDS are even larger than for the other two samples. TEM images taken for post-HDS 5.9 nm $Ni_2P@mSiO_2$ sample also confirms that particle size growth occurred during HDS (Figure 4.13). This could be due to the fact that the average pore size (5-6 nm) of mesoporous silica network is in same range as the smallest sized Ni_2P nanoparticles (5.9 nm), allowing particles to migrate during the HDS testing. However, the fact these remain the most active, even after sintering suggest that activity is not a simple function of surface area.

Table 4.2. Crystallite size measured by application of the Scherrer equation to powder diffraction data of as-prepared and post-HDS $Ni_2P@mSiO_2$ catalysts.

Catalyst	As-prepared (nm)	Post-HDS (nm)
$Ni_2P@mSiO_2$	5.9	20
$Ni_2P@mSiO_2$	11.2	13
$Ni_2P@mSiO_2$	17.1	18

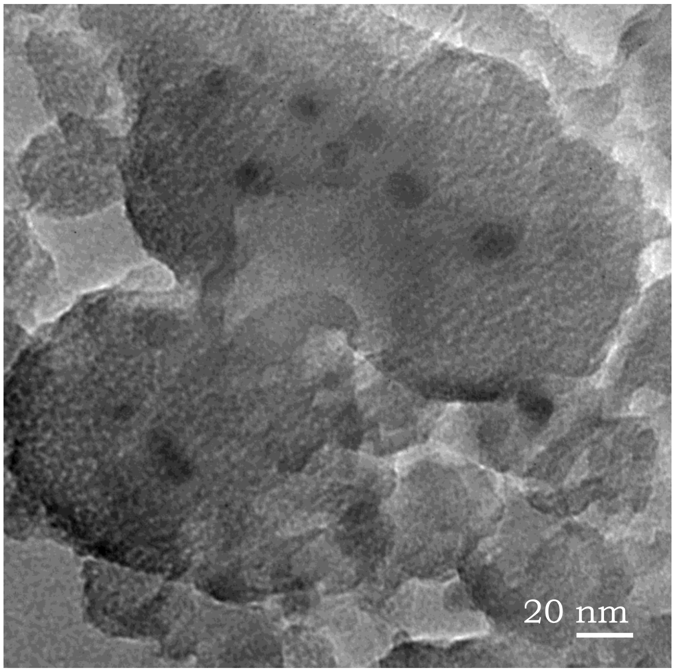

Figure 4.13. TEM image of 5.9 nm $Ni_2P@mSiO_2$ post-HDS.

4.6 Conclusion

We optimized the formation conditions of $Ni_2P@mSiO_2$ with respect to pH, time, and TEOS concentration to yield $Ni_2P@mSiO_2$ within 10-15 minutes and with controlled loading. This is the first example of Ni_2P nanoparticles encapsulation within a mesoporous silica shell. This method also represents a significant improvement over previously reported methods for nanoparticle encapsulation and appears to be generally applicable to a wide range of chemically different nanoparticles.

Sintering of Ni_2P nanoparticles was minimized by incorporation of Ni_2P nanoparticles into a mesoporous silica network, resulting in a vast improvement in activity. This enables quantitative size-dependent mechanistic HDS studies of Ni_2P catalysts.

CHAPTER 5

SYNTHESIS OF NOBLE METAL PHOSPHIDE NANOPARTICLES (Rh_2P, Pd_5P_2): STUDY OF DEEP-HDS ACTIVTY

5.1 Introduction

The goal of the third part of the dissertation research is to synthesize noble metal phosphides (Rh_2P, Pd_5P_2) on the nanoscale in order to study their deep HDS catalytic activity. Substituted dibenzothiophenes are harder to remove from crude oils using commercially available catalysts due to steric hindrance, which renders the direct desulfurization (DDS) pathway difficult. Therefore, the HYD pathway wherein hydrogenation of a phenyl group occurs first, de-planarizing the ring and enabling access to the sulfur center should be perused in order to achieve ultra-low S levels (i.e. deep HDS) in fuel. As a result, noble metals such as Pd, Pt, and Rh, which are excellent hydrogenation catalysts, show high activity for deep-HDS when dispersed as nanoscale particles on an oxide support.[28, 29, 51] However, noble metals are susceptible to sulfur poisoning, causing the activity to drop over time. This problem has been addressed by the use of noble metal phosphides (Rh_2P,[30] Ru_2P,[96, 97] Pd_5P_2[31]) prepared by the temperature programmed reduction method (TPR). Phosphides are more resistant to sulfur poisoning while maintaining good HDS activity. For example, Rh_2P catalysts showed higher dibenzothiophene (DBT) HDS activity compared to commercial Ni-Mo/Al_2O_3 and Rh/SiO_2 catalysts and are sulfur tolerant (stable over 100 h of DBT HDS).[30]

However, these TPR prepared silica-supported catalysts suffer from the same problems as TPR-prepared Ni_2P, a limited ability to control the size and a large degree of polydispersity. Therefore, in the dissertation research, a method for the synthesis of Rh_2P and Pd_5P_2 nanoparticles using arrested precipitation reactions to generate low-polydispersity discrete nanoparticles is reported and their HDS activity as a function of particle size and support (SiO_2 vs. $mSiO_2$) is evaluated.

I collected all data in this chapter with the exception of HDS catalytic data which were collected in Bussell lab in department of chemistry at western Washington University.

5.2 Experimental Section

All chemicals used for the syntheses described in this chapter are listed in Chapter 2.1.

5.2.1 Synthesis of Rh_2P nanoparticles

Rh_2P nanoparticles were synthesized using a modification of a literature procedure developed by Schaak and co-workers.[12] A mixture of $RhCl_3 \cdot xH_2O$ (60 mg) and hexadecylamine (2 g) was dissolved in oleylamine (3 mL). The flask was degassed for 15 minutes at room temperature and then the temperature was increased to 110 °C and was maintained for 30 minutes under Ar flow. The temperature was then increased to 260 °C and maintained for 2h to generate Rh nanoparticle precursors. The reaction mixture was brought to room temperature and then 10 mL of TOP was added. The mixture containing Rh and TOP was then cannulated into TOPO (4 g) at 360 °C. The reaction was heated at 360 °C for 3 hours. The product was isolated as a black precipitate by dispersion in chloroform (3 mL) and precipitation with ethanol (5 mL).

5.2.2. Preparation of 2 wt% Rh_2P/SiO_2 Precatalyst

2 wt% Rh_2P/SiO_2 precatalyst was prepared using the incipient wetness method as described in Chapter 3.2.2.

5.2.3 Palladium Phosphide Nanoparticles

0.33 mmol (100 mg) of $Pd(acac)_2$, 5 mL of oleylamine, 1-5 mL of TOP and 10 mL of octylether were mixed in a Schlenk flask. The system was degassed under partial vacuum at 110

°C for 20 minutes, purged with Ar and then the temperature was raised to 270 - 360 °C. The reaction time was varied from 30 minutes to 12 hours. The isolation of the resultant black precipitate was achieved with excess ethanol followed by centrifugation. Purification was achieved by sonicating the solid with 2-5 mL of $CHCl_3$ and re-precipitating with excess ethanol.

5.2.4 Three step synthesis of Pd_5P_2 (5 wt %-targeted) @mSiO_2 nanoparticles

5.2.4.1 Pd-P amorphous nanoparticle synthesis

0.33 mmol (100 mg) of $Pd(acac)_2$, 5 mL of oleylamine, 5 mL of TOP, and 10 mL of octylether were combined in a Schlenk flask. The reaction mixture was degassed at 110 °C for 15 minutes, purged with Ar and then the reaction mixture was heated at 280-300 °C for 2 hours. Pd-P nanoparticles were isolated by adding excess ethanol followed by centrifugation.

5.2.4.2 Incorporation of Pd-P nanoparticles into a mesoporous silica matrix (Pd-P@mSiO_2)

The entire Pd-P product formed in step I was dispersed in 5 mL of $CHCl_3$ and added to 20 mL of a 0.1 M CTAB solution dropwise. The temperature of the Pd-P/$CHCl_3$/CTAB/H_2O mixture was raised to 75 °C and kept for 20-30 minutes while stirring vigorously to remove $CHCl_3$ from the mixture. Then ~ 20 mL of the Pd-P/CTAB/Hi_2O mixture was diluted with 130 mL of nanopure H_2O followed by 3 mL of a 1 M NaOH solution. The base-catalyzed silica polymerization was then performed by injecting 2.75 mL of TEOS (in order to target 5% wt loading of final Pd_5P_2) using a syringe pump at rate of 0.5 mL/min. The reaction was carried out for 15 minutes at 50 °C. The isolation of Pd-P@mSiO_2 was achieved by centrifugation at 4000 ppm for 5 minutes. The isolated Pd-P@mSiO_2 product was washed three times with nanopure water and 3 times with methanol, followed by centrifugation. The purified Pd-P/mSiO_2 samples were vacuum dried overnight to get rid of any solvent left during the isolation and purification steps.

5.2.4.3 Conversion of Pd-P@mSiO_2 to Pd_5P_2@mSiO_2 (with and without calcination in air)

(a) with calcination in air: As-prepared Pd-P@mSiO_2 samples were air calcined in an oven at 430 °C for 150 minutes to burn off CTAB and organic ligands bound to the Pd-P nanoparticles. The oxidized Pd-P@mSiO_2 nanoparticles were then reduced by heating under 5% H_2/Ar at 500-650 °C in the presence of PPh_3 vapor from solid PPh_3 loaded upstream of the calcined Pd-P@mSiO_2 particles.

(b) without calcination in air: As-prepared Pd-P@mSiO_2 was directly hearted under 5% H_2/Ar flow at 500 °C for 2 hours in a flow furnace.

5.2.5. HDS Activity Measurements for Rh_2P/SiO_2 and Pd_5P_2@mSiO_2 (Acquired by the Bussell Group at Western Washington University)

Thiophene HDS activity of Rh_2P/SiO_2 was measured as a function of time using an atmospheric pressure flow reactor. 0.1 g of Rh_2P/SiO_2 precatalyst was placed in the reactor and preheated at 377 °C for 2 h under 5% H_2/He mixture. Then 3.2 mol% thiophene/H_2 mixture was sent through the precatalyst at 375 °C and thiophene activity measured as the function of time.

Dibenzothiophene activity of Pd_5P_2@mSiO_2 was measured as described in Chapter 3.2.4.

5.3 Results and Discussion

5.3.1 Synthesis and Characterization of Rh_2P nanoparticles

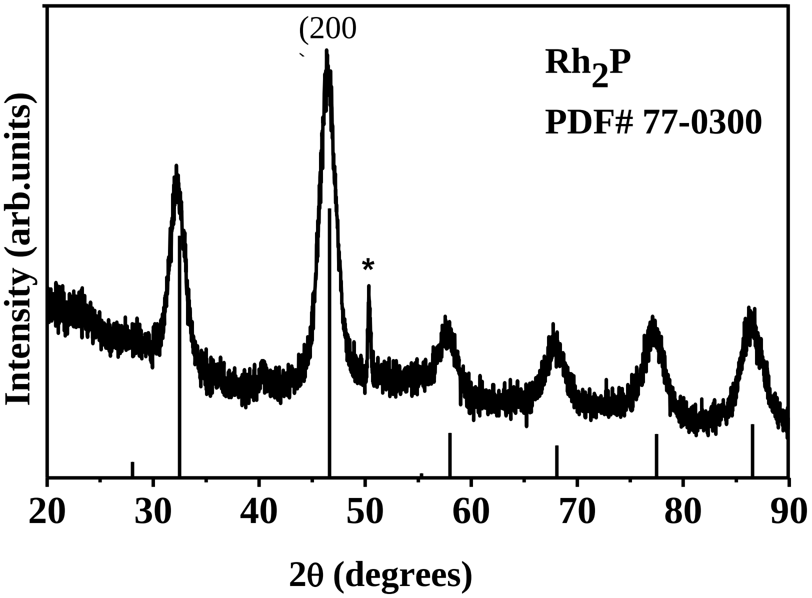

Figure 5.1. PXRD pattern of Rh_2P nanoparticles and the corresponding reference pattern (PDF # 17-0300). The peak around 50° (denoted by *) is due to the sample holder.

Rh_2P nanoparticles were synthesized using a modification of a literature procedure developed by Schaak and co-workers.[53] In the first step, Rh nanoparticles are formed at 260 °C, as indicated by the sudden change of the reaction mixture from a clear solution to a black colloidal solution. The conversion of Rh to Rh_2P subsequently takes place at 360 °C in the presence of TOP. As shown in the PXRD pattern, this reaction leads to the formation of phase-pure Rh_2P nanoparticles with a crystallite size of 4-5 nm as assessed by application of the Scherrer equation to the (200) peak (Figure 5.1).

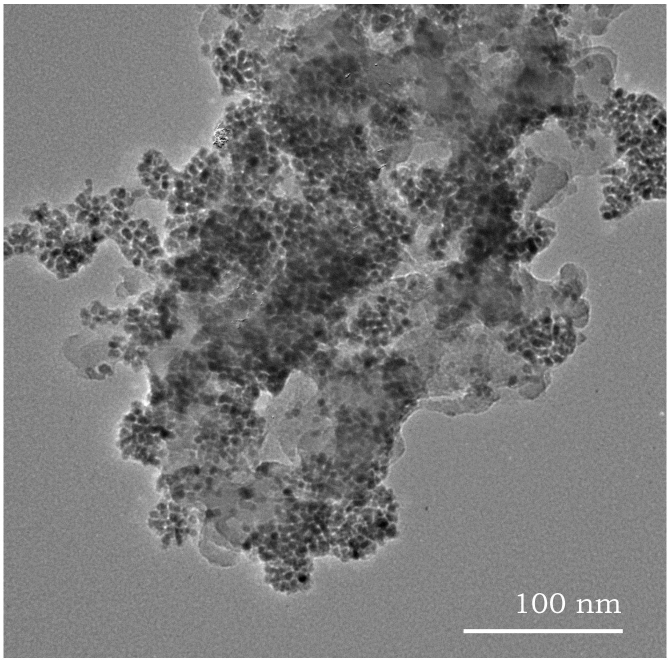

Figure 5.2. TEM image of Rh_2P nanoparticles.

Even though we were able to make phase-pure Rh_2P nanoparticles using this method, these particles were found to be significantly aggregated as shown by TEM (Figure 5.2). In addition, a low contrast amorphous component is intimately mixed with the particles. The origin of the amorphous layer is unclear. EDS data suggests that the Rh: P ratio is 2:1 as expected (Figure 5.3).

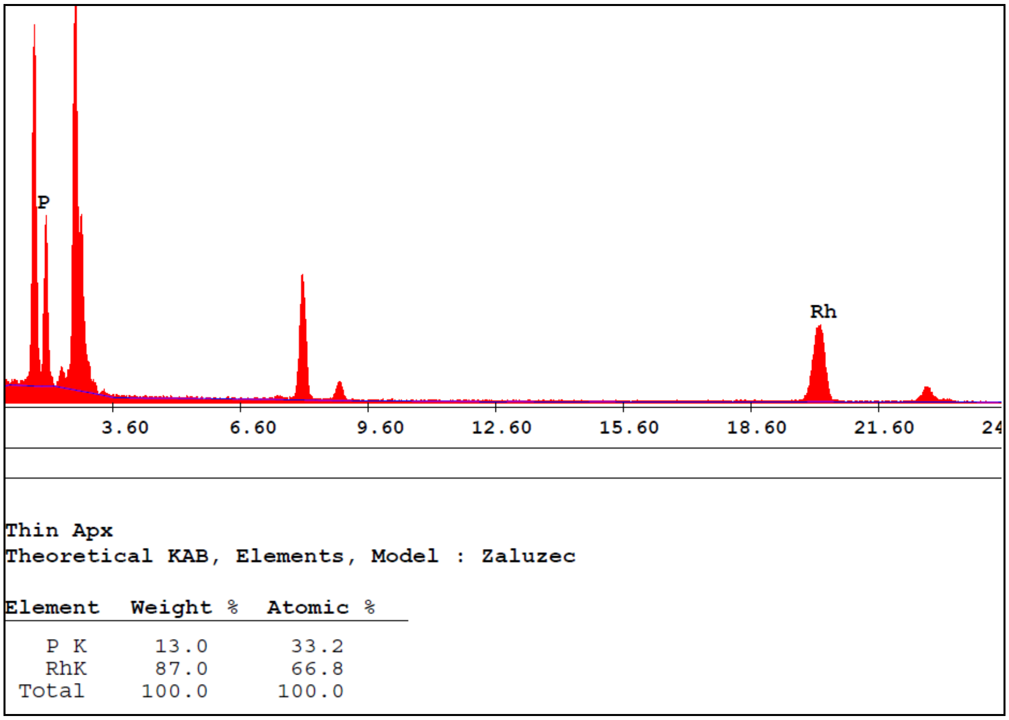

Thin Apx
Theoretical KAB, Elements, Model : Zaluzec

Element	Weight %	Atomic %
P K	13.0	33.2
RhK	87.0	66.8
Total	100.0	100.0

Figure 5.3. EDS spectrum of a Rh_2P nanoparticle sample.

As the Rh_2P nanoparticles were not discretely separated from each other, it was difficult to disperse them in a polar solvent (water or ethanol) in order to introduce them to the silica support to make the pre-catalyst. Nevertheless, we targeted a 2 wt% Rh_2P/SiO_2 composite by the incipient wetness method to investigate the catalytic activity of Rh_2P nanoparticles. A thiophene activity test was performed to investigate the reactivity of these aggregated particles towards more accessible sulfur sources (i.e. thiophene in lieu of dibenzothiophene). As shown in Figure 5.4, thiophene conversion of 2 wt% Rh_2P/SiO_2 nanoparticle sample is extremely low compared to a 10 wt% Ni_2P/SiO_2 nanoparticle sample, but remains steady over time. This low activity is probably due to the lack of exposure of active sites due to the aggregated nature of the particles and consequently the difficulty for the thiophene molecules to access the Rh_2P active sites. This may be exacerbated by the presence of the amorphous layer. In order to achieve the maximum potential activity of Rh_2P nanoparticles, the synthesis will need to be improved to yield well dispersed Rh_2P nanoparticles. Given the poor performance with thiophene, DBT HDS was not studied with this system.

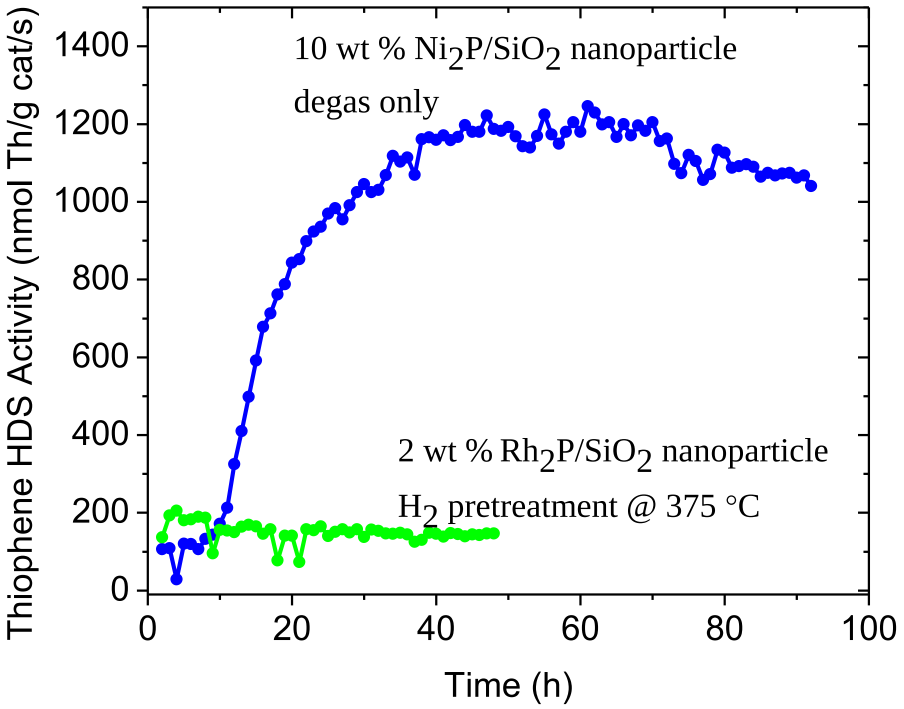

Figure 5.4. Thiophene conversion of 2 wt % Rh_2P/SiO_2 and 10 wt % Ni_2P/SiO_2 nanoparticle catalysts as a function of time on stream.

5.3.3 Synthesis and Characterization Pd_5P_2 Nanoparticles

Due to the difficulties encountered in the synthesis of Rh_2P, it was decided that focusing on efforts on Pd_5P_2 would be more productive. The direct synthesis of monodisperse, spherical, small (5-10 nm) noble metal phosphide nanoparticles has also proven challenging to achieve by solution phase arrested precipitation. For the case of Pd_5P_2, it has been shown that pre-made Pd nanoparticles will react with TOP at 330 °C resulting in a mixture of Pd_5P_2 and PdP_2.[53] Phase-pure Pd_5P_2 particles were successfully prepared from the direct reaction between palladium (II) acetylacetonate ($Pd(acac)_2$) and TOP.[53] However, the particle size and distribution were not quantified. To achieve a discrete, monodisperse and small nanoparticles of Pd_5P_2, amorphous Pd-P nanoparticles were formed at relatively low temperature, encapsulated into mesoporous silica to prevent particle growth, and then converted to crystalline Pd_5P_2 via a high temperature treatment under reducing conditions.

Precursor amorphous Pd-P particles were prepared by reaction of 0.33 mmol of $Pd(acac)_2$ with 5 mL of TOP (P:Pd = 34) in the presence of 2-5 mL of oleylamine and 10 mL of octylether at varying temperatures (270-300 °C) for 0.5-12 h. Two broad peaks in the powder X-ray diffraction (PXRD) pattern reveal the amorphous nature of the resultant product even after 12 h at 300 °C (Figure 5.5a). EDS analysis performed on these amorphous products reveals that these particles have a significant level of P (the Pd:P ratio varies between 50:50 and 70:30) incorporated into the palladium lattice (Figure 5.6). This observation is in agreement with the nickel phosphide system where Ni-P amorphous nanoparticles are generated when a large amount of TOP is used at moderately high temperatures (230-260 °C).[50, 98] The Pd-P amorphous nanoparticles are spherical and nearly monodisperse, self-assembling into a hexagonal pattern (Figure 5.5b). The average particle size of Pd-P can be tuned by varying the amount of oleylamine; the average particle size increases from 6 to 9 nm when the amount of oleyalmine in the reaction is increased from 2 to 5 mL (Figure 5.7). This Pd-P amorphous particle size dependency on amount of oleylamine is consistent with the Ni-P amorphous particle system.[59]

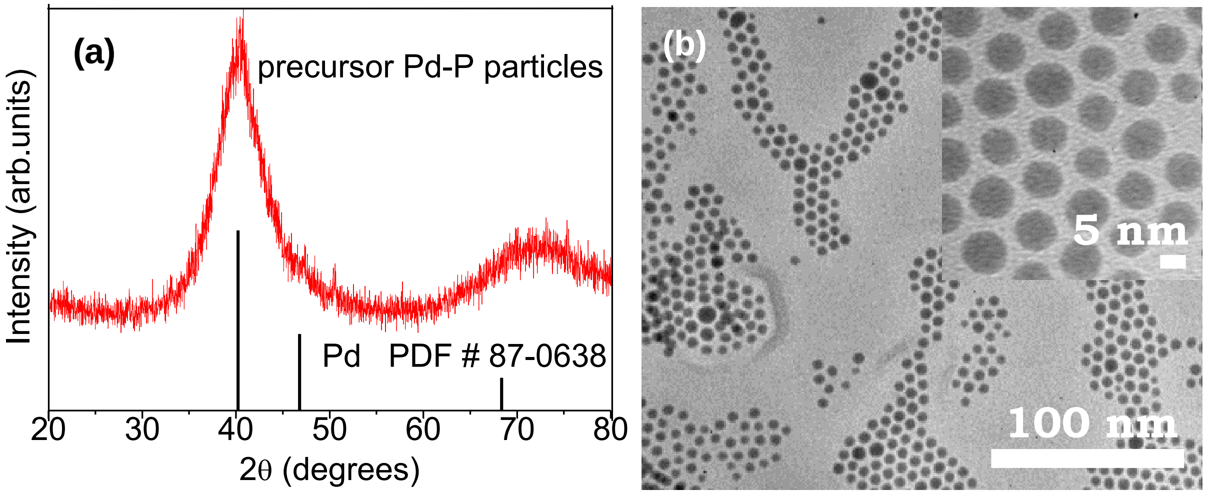

Figure 5.5 (a) PXRD pattern and (b) TEM image of Pd-P nanoparticles formed using 5 mL oleylamine at 300 °C for 2h.

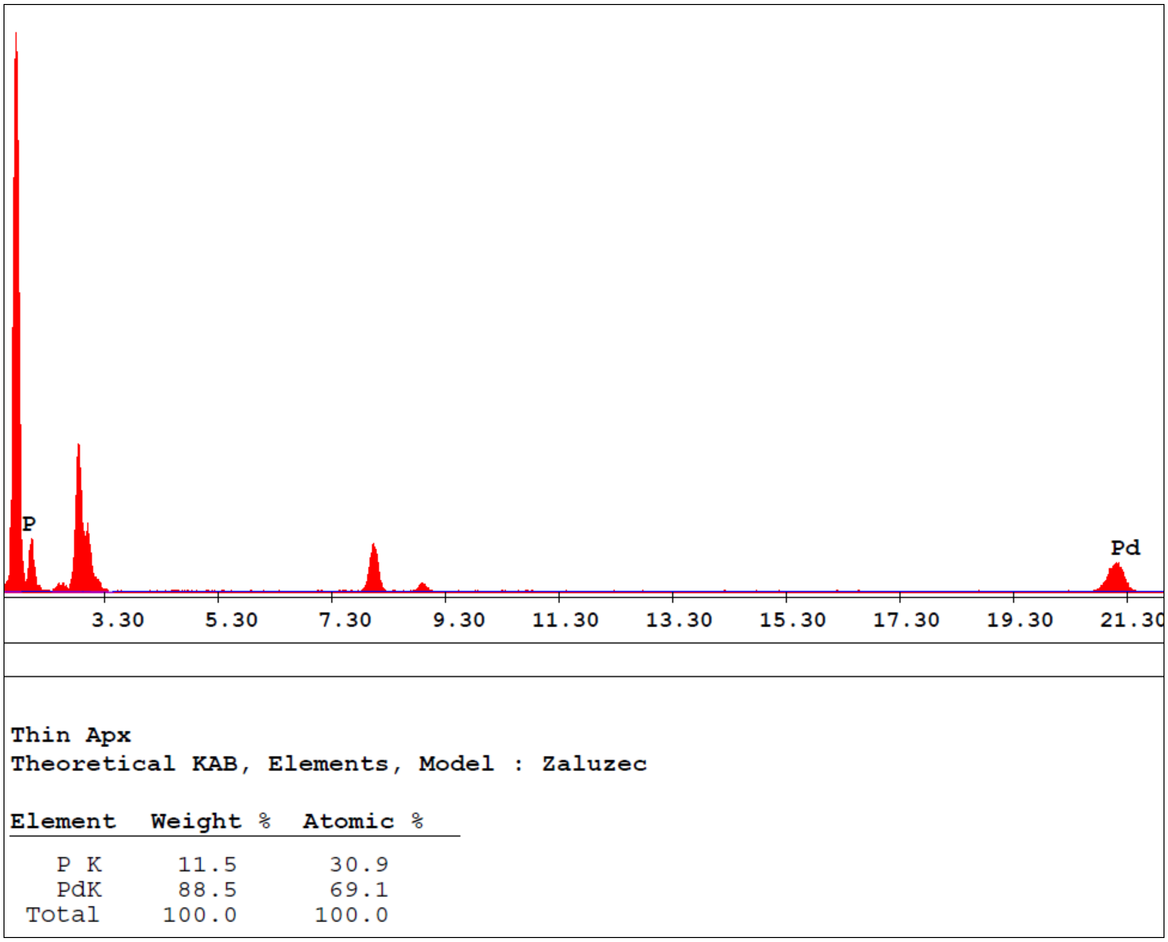

```
Thin Apx
Theoretical KAB, Elements, Model : Zaluzec

Element   Weight %   Atomic %

   P K      11.5       30.9
   PdK      88.5       69.1
 Total     100.0      100.0
```

Figure 5.6. Representative EDS pattern and Pd:P ratio of Pd-P nanoparticles formed at 300 °C from the reaction between 0.33 mmol of Pd(acac)$_2$ and 5 mL of TOP.

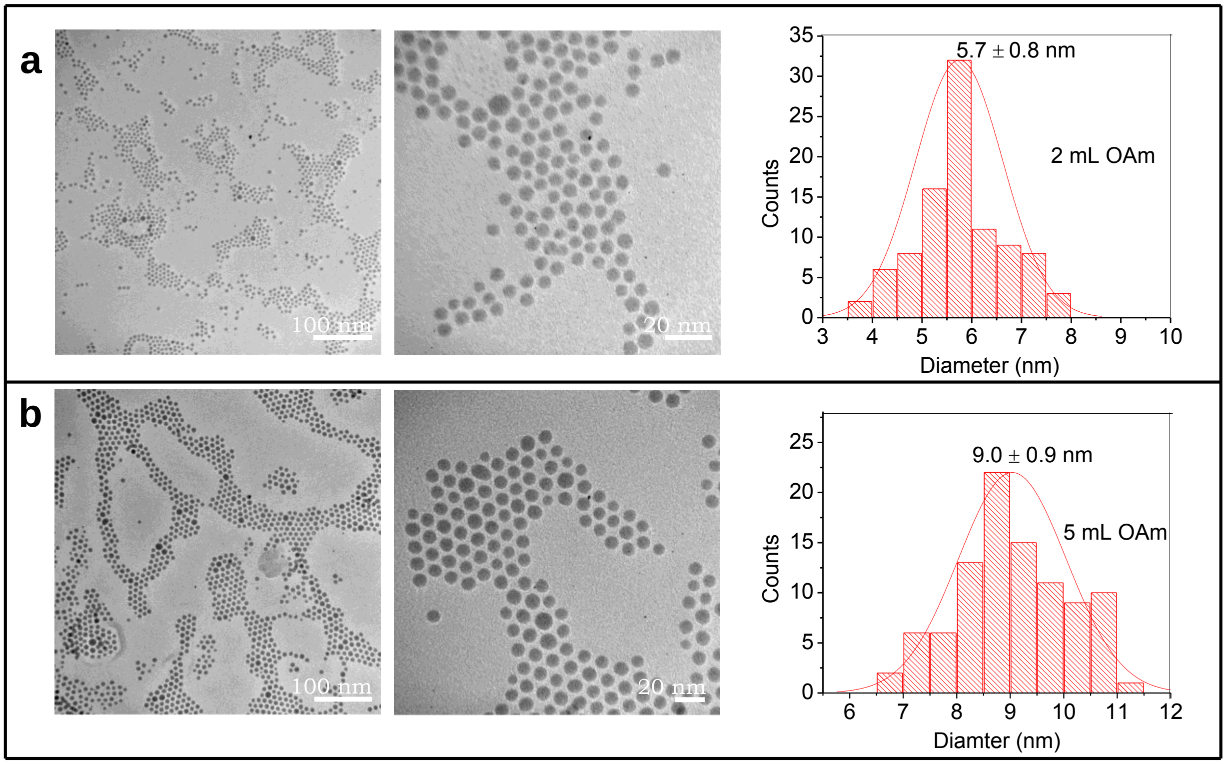

Figure 5.7. TEM images of varying sizes of Pd-P nanoparticles formed at 300 °C from the reaction between 0.33 mmol of Pd(acac)$_2$ and 5 mL of TOP in the presence of 2 mL (a) and 5 mL (b) of oleylamine.

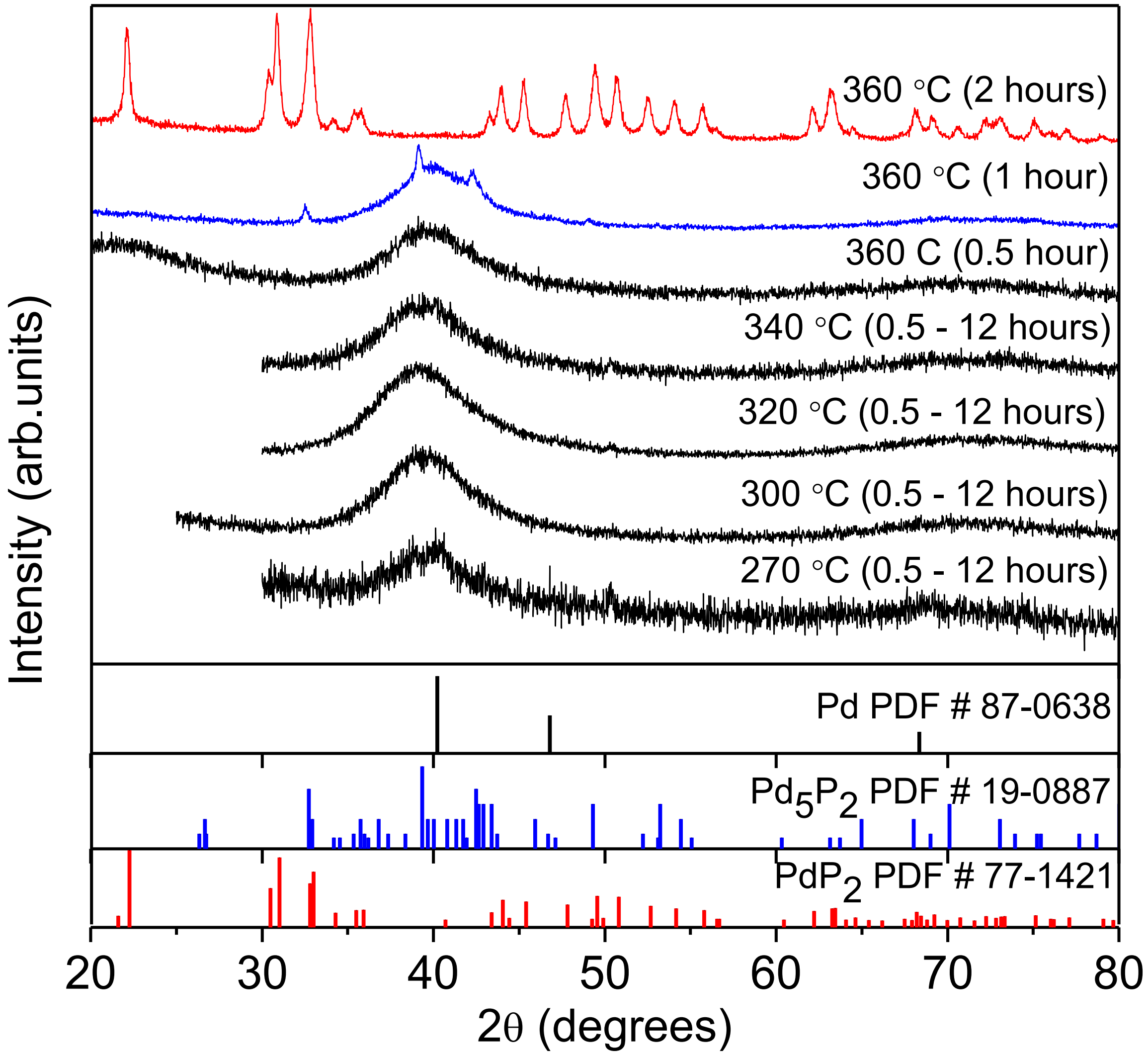

Figure 5.8. PXRD pattern of the products resultant from the reaction between 0.33 mmol of Pd(acac)$_2$ and 5 mL of TOP in the presence of oleylamine and octylether at varying temperatures (270-360 °C) for 0.5-12 hours of reaction time.

When the reaction was carried out at 360 °C for 1 h, the presence of crystalline Pd_5P_2 was observed by PXRD (Figure 5.8). However, a broad feature was present beneath the sharp Pd_5P_2 peaks, suggesting that amorphous Pd-P was also present. If instead heated for 2 h at 360 °C, phase-pure PdP_2 was formed and the PXRD peaks are sharp, indicating that the crystallites are quite large in size. To prevent formation of the phosphorous-rich Pd_5P_2 phase, we reduced the amount of TOP systematically and found that phase-pure Pd_5P_2 is formed when only 1 mL (P:Pd = 6.8) instead of 5 mL of TOP (P:Pd = 34) is employed at a reaction temperature of 360 °C after 4 h (Figure 5.9a). Under these conditions, nucleation (as probed by a change in color of the solution) did not take place below 360 °C suggesting Pd-P amorphous particles were not formed as intermediates. Instead formation of crystalline Pd_3P occurs first (dominant phase) at 360 °C (within 1 h of the reaction) followed by the conversion to Pd_5P_2 as shown in Figure 5.10. However, the resultant Pd_5P_2 crystallites were large and aggregated, yielding clusters a few hundred nm in diameter as shown by TEM analysis (Figure 5.9b), and as reflected in the narrow peak widths in the PXRD pattern (Figure 5.9a).

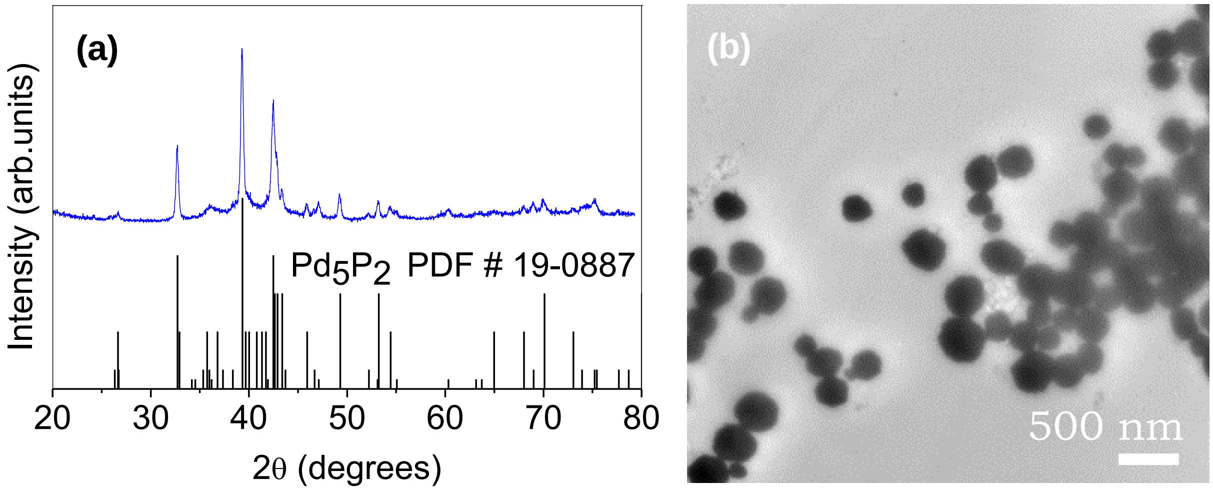

Figure 5.9. (a) PXRD pattern and (b) TEM image of Pd_5P_2 particles made by direct reaction of $Pd(acac)_2$ and TOP (P:Pd = 6.8) at 360°C for 4 h.

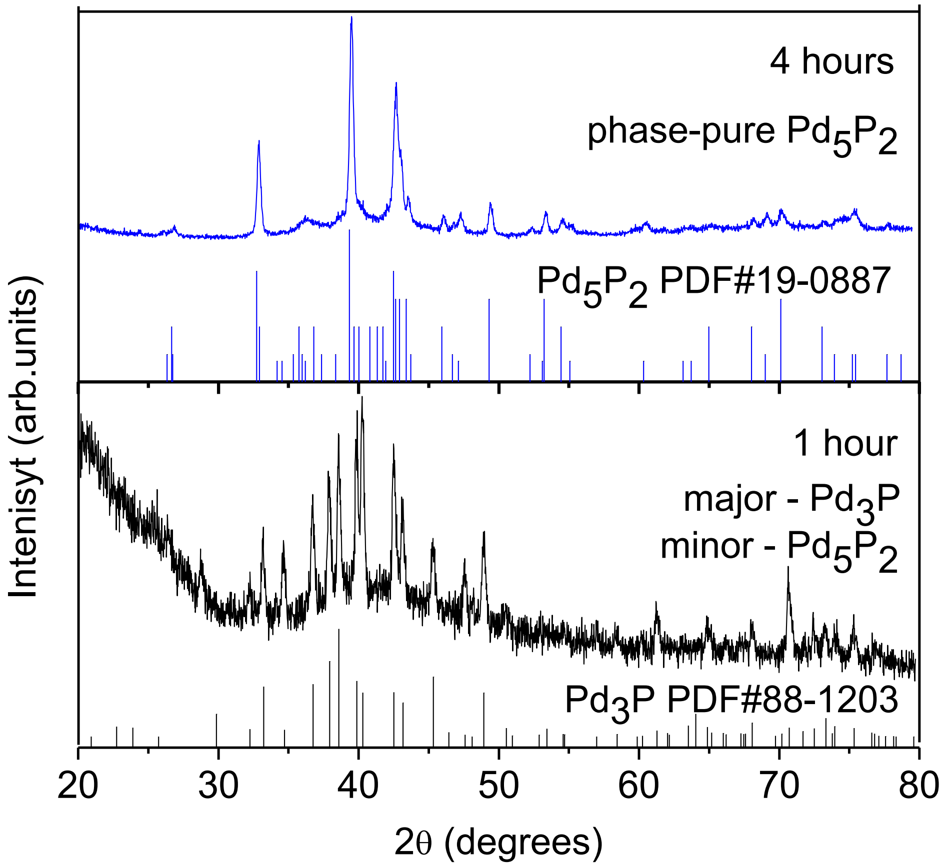

Figure 5.10. PXRD data of the palladium phosphide products from the reaction between 0.33 mmol of $Pd(acac)_2$ and 1 mL of TOP in the presence of 5 mL of oleylamine and 10 mL octylether at 360 °C after 1 hour and 4 hours.

In order to prevent sintering in the formation of Pd_5P_2, we developed a novel synthetic strategy in which intermediate monodisperse discrete Pd-P nanoparticles formed at 300 °C (avoiding the formation of PdP_2) were trapped in a mesoporous silica network and then converted to the catalytically interesting phase, Pd_5P_2, by heating under reducing conditions in a flow furnace.

5.3.4. Synthesis of Pd-P@mSiO$_2$ and Conversion of Pd-P@mSiO$_2$ to Pd$_5$P$_2$@mSiO$_2$

Phase transfer of Pd-P nanoparticles to water was achieved by addition of chloroform-dispersed Pd-P nanoparticles into a concentrated cetyltrimethylammonium bromide (CTAB) aqueous solution followed by evaporation of chloroform at 75 °C for 20-30 min. Subsequently, base-catalyzed silica polymerization was performed by injecting tetraethylorthosilicate (TEOS) to the basified Pd-P/CTAB/H$_2$O solution resulting in Pd-P@mSiO$_2$. TEM reveals discrete, spherical and monodisperse Pd-P particles embedded in a mesoporous silica matrix (Figure 5.11b) and the particles remain amorphous during the encapsulation process (compare Figure 5.5a and 5.11a).

The Pd-P@mSiO$_2$ was subsequently calcined at 430 °C in air for 2.5 h to remove the CTAB template and organic ligands bound to the nanoparticle surface. This resulted in formation of PdO@mSiO$_2$ in which PdO is the only crystalline product detected (Figure 5.12b). Attempts to recover the phosphide by heating PdO@mSiO$_2$ in a flowing 5% H$_2$/Ar mixture at temperatures up to 650 °C for 2 h yielded only the Pd phase (Figure 5.12c). These data suggest that either the oxidized phosphorous species do not convert to a more reduced state under these conditions or that phosphorus is lost during calcination. Since PPh$_3$ has proven to be a useful phosphorus source in metal phosphide synthesis, including to achieve Ni$_2$P in Ni$_2$P@mSiO$_2$,[50, 59, 93-95] we introduced PPh$_3$ vapor by placing a sample of solid PPh$_3$ upstream in the flow furnace and, under reducing conditions, varying the temperature and time. As the temperature was increased to 650 °C, the phase transformation from Pd to Pd$_5$P$_2$ took place gradually via the intermediate Pd-P amorphous phase (Figure 5.12d-f). However, the peaks remain very broad, suggesting the majority of the sample remains amorphous.

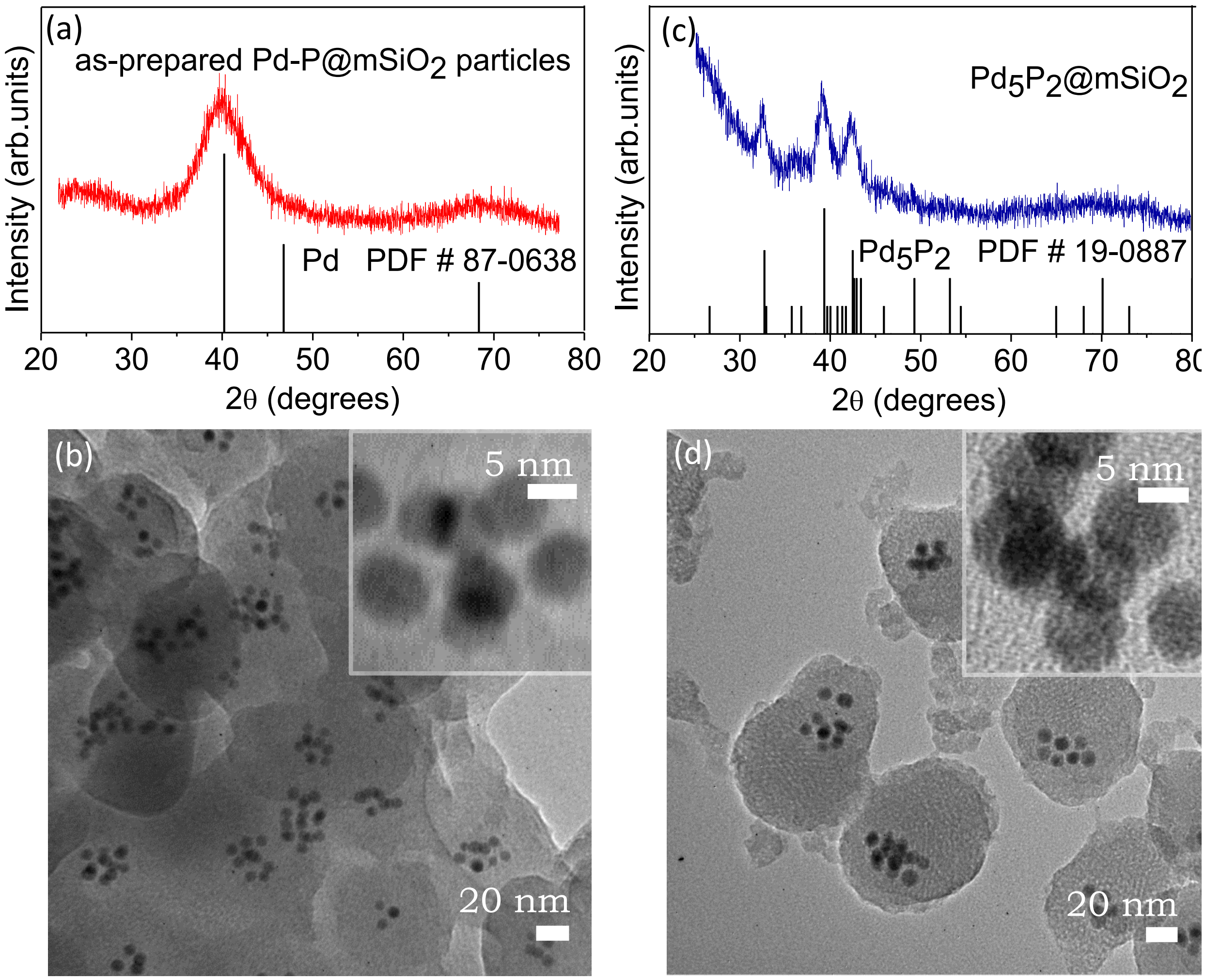

Figure 5.11. PXRD patterns of (a) as-prepared Pd-P@mSiO$_2$ nanoparticles and (c) 5 wt% Pd$_5$P$_2$@mSiO$_2$ nanoparticles formed after treating as-prepared Pd-P@mSiO$_2$ nanoparticles under 5% H$_2$/Ar mixture at 500 °C for 2 hours; corresponding TEM images (b) Pd-P@mSiO$_2$ and (d) Pd$_5$P$_2$@mSiO$_2$.

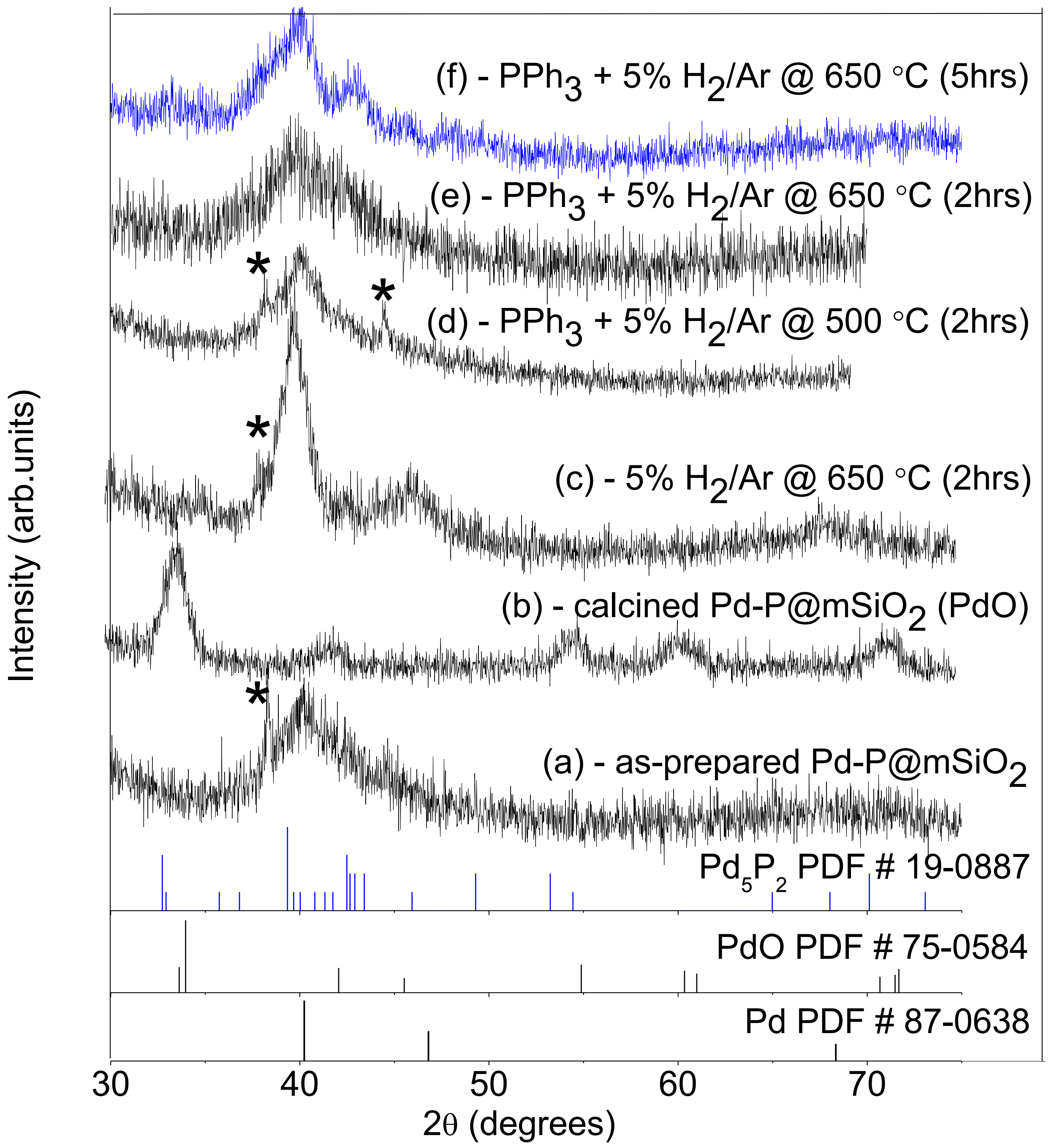

Figure 5.12. PXRD patterns of (a) as-prepared Pd-P@mSiO$_2$; (b) product calcined at 430 °C for 2.5 h; (c), (d), (e), (f) products resulting from heating at varying temperatures under different reducing and post-treatment conditions. * denotes peaks from the sample holder.

We next attempted directly heating as-prepared Pd-P@mSiO_2 particles under a 5 % H_2/Ar mixture at 500 °C for 2 hours in a flow furnace. Surprisingly, a complete transformation from amorphous Pd-P to phase-pure Pd_5P_2 was observed (Figure 5.11c). This is attributed to the solid state transformation (reduction) and reorganization (crystallization) of phosphorous present in Pd-P particles to Pd_5P_2. Most importantly, the particles retain their morphology (spherical) and do not appear to sinter (Figure 5.11d); rather the particles are localized /embedded at different levels within the mesoporous silica particles. EDS analysis performed on this sample revealed that the Pd:P ratio (71.2:28.8) is in close agreement with the theoretical ratio (71.4:28.6) of Pd_5P_2. Moreover, the final Pd_5P_2@mSiO_2 weighed ~ 750-800 mg, indicating that silica polymerization goes to completion (theoretical yield of silica ~ 740 mg and Pd_5P_2 ~ 39 mg). Notably, even when the precursor Pd-P particles are P-rich relative to the targeted product (e.g. P:Pd = 50:50 in Pd-P), Pd_5P_2 is the only phase obtained after H_2 treatment at 500 ºC, suggesting that this phase is the most phosphided phase that can be accessed under high temperature, reducing conditions.

5.3.5. Physical Characterization of Pd_5P_2@mSiO_2

Thermal gravimetric analysis (TGA analysis) carried out in air on Pd_5P_2@mSiO_2 indicates a weight loss of less than 0.5 wt% is occurring up to 500 ºC (Figure 5.13). This suggests that the direct reduction method successfully eliminates the organic matter in Pd-P@SiO_2, enabling accessible Pd_5P_2 particles to be prepared in a single step. The elimination of surfactant is also evident in the nitrogen porosimetry data (Figure 5.14). The Brunauer-Emmett-Teller (BET) surface area was determined to be 1040 m^2g^{-1} while the Barrett-Joyner-Halenda BJH adsorption average pore size was 3.7 nm. Mesopores are also evident in high resolution TEM images (Figure 5.15a) and are of appropriate size for introduction of molecules such as DBT.

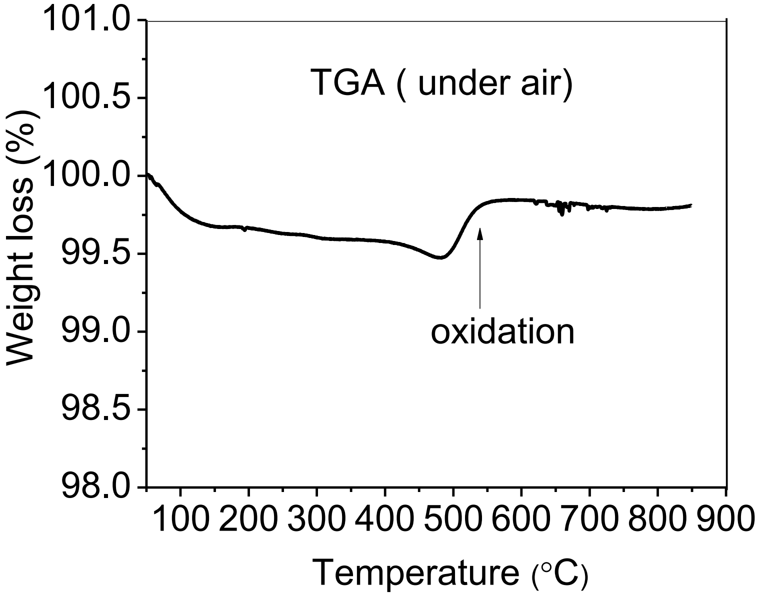

Figure 5.13. Thermal Gravimetric Analysis (TGA) of Pd_5P_2@mSiO_2 conducted under air. The slight weight gain from 475-575 °C might be due to surface oxidation of the Pd_5P_2 nanoparticles.

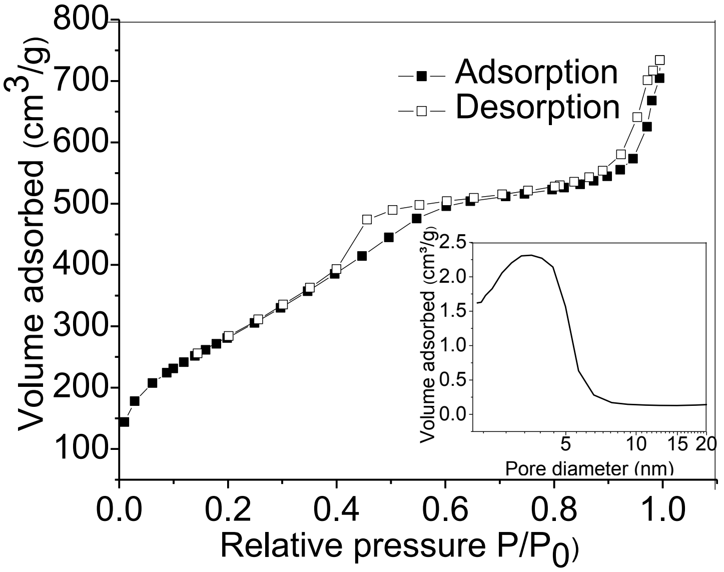

Figure 5.14. Nitrogen adsorption–desorption isotherms and pore size distribution calculated from the adsorption branch of the isotherms of Pd_5P_2@mSiO_2 nanoparticles formed after heating Pd-P@mSiO_2 nanoparticles under 5% H_2/Ar mixture at 500 °C for 2 hours in a flow furnace.

5.3.6. Sintering Behavior of Pd_5P_2/SiO_2

In order to demonstrate the importance of the mesoporous silica matrix to prevent sintering, Pd-P nanoparticles were introduced onto an amorphous silica support ((Cab-O-Sil, M-7D grade, 200 m^2/g) using the incipient wetness method and heated under the same conditions with which the Pd-P@$mSiO_2$ samples were treated (5% H_2/Ar, 500 °C for 2 h). The resultant particles are significantly sintered, resulting in large crystalline aggregates (Figure 5.15b). Moreover, the product is not pure; Pd_3P is present as a secondary phase (Figure 5.16).

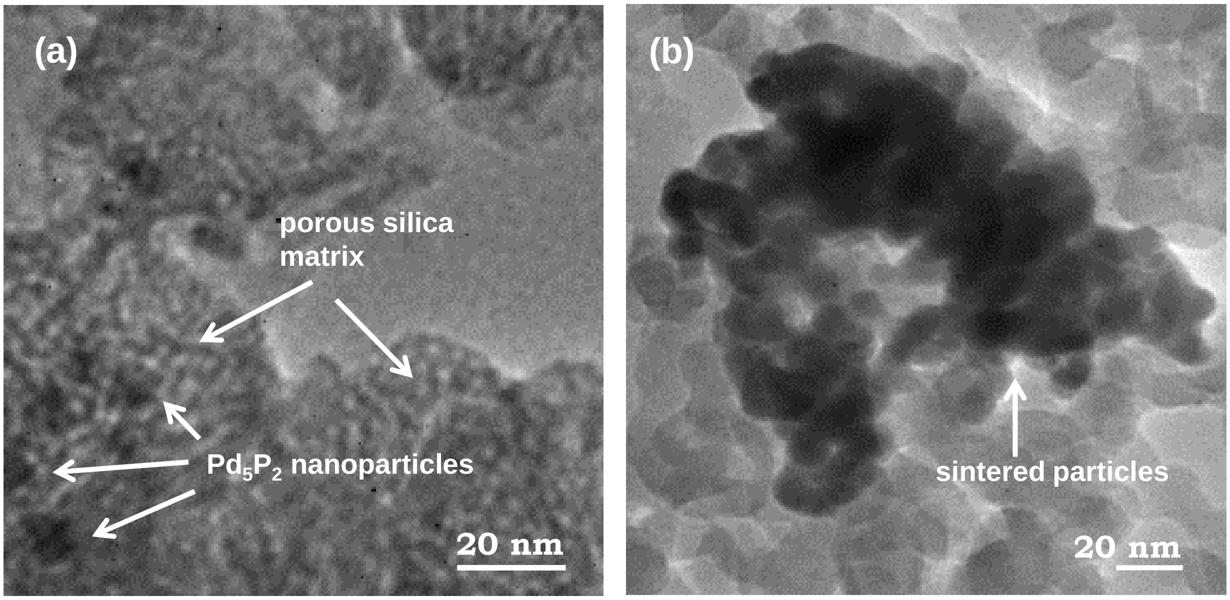

Figure 5.15. TEM image of (a) Pd_5P_2@$mSiO_2$ showing the presence of discrete Pd_5P_2 particles in a porous silica matrix, still present after heating under a reducing environment at 500 ºC; (b) sintered particles resultant from heating unencapsulated Pd-P nanoparticles impregnated on to silica by the incipient wetness method under the same conditions as for (a).

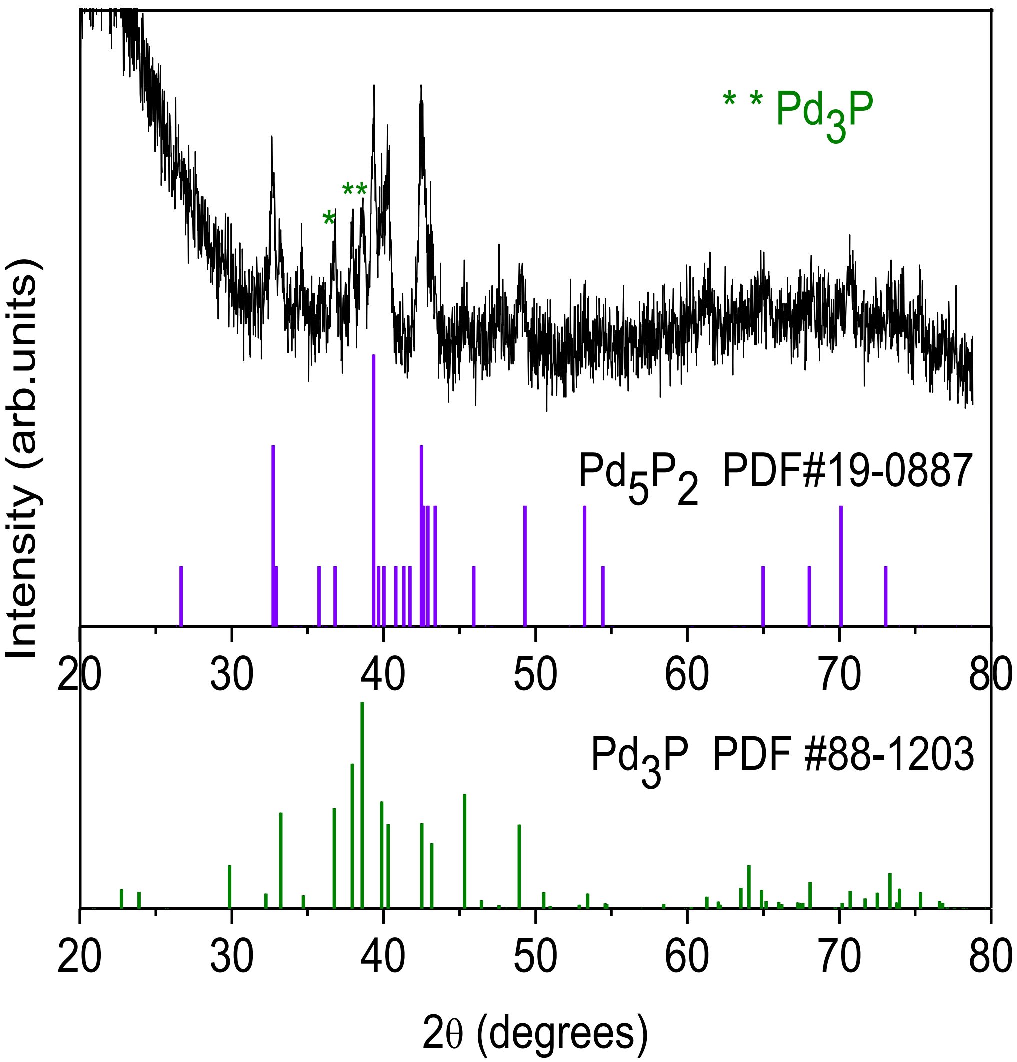

Figure 5.16. PXRD pattern of the product resulting from heating Pd-P/SiO_2 (made by the incipient wetness method) under 5% H_2/Ar flow at 500 °C for 2 hours. * denotes the impurity peaks corresponding to Pd_3P.

5.3.7. HDS Activity of Pd_5P_2@$mSiO_2$ Catalyst

Finally, to establish molecule accessibility to the Pd_5P_2 particles in Pd_5P_2@$mSiO_2$, and to demonstrate the activity of the catalyst. DBT HDS studies were conducted on Pd_5P_2@$mSiO_2$ (~9 nm diameter Pd_5P_2) using a fixed-bed flow reactor in the temperature range 250-400 °C. The products of the dibenzothiophene HDS catalytic reaction were collected in 25 ºC intervals as a function of temperature.

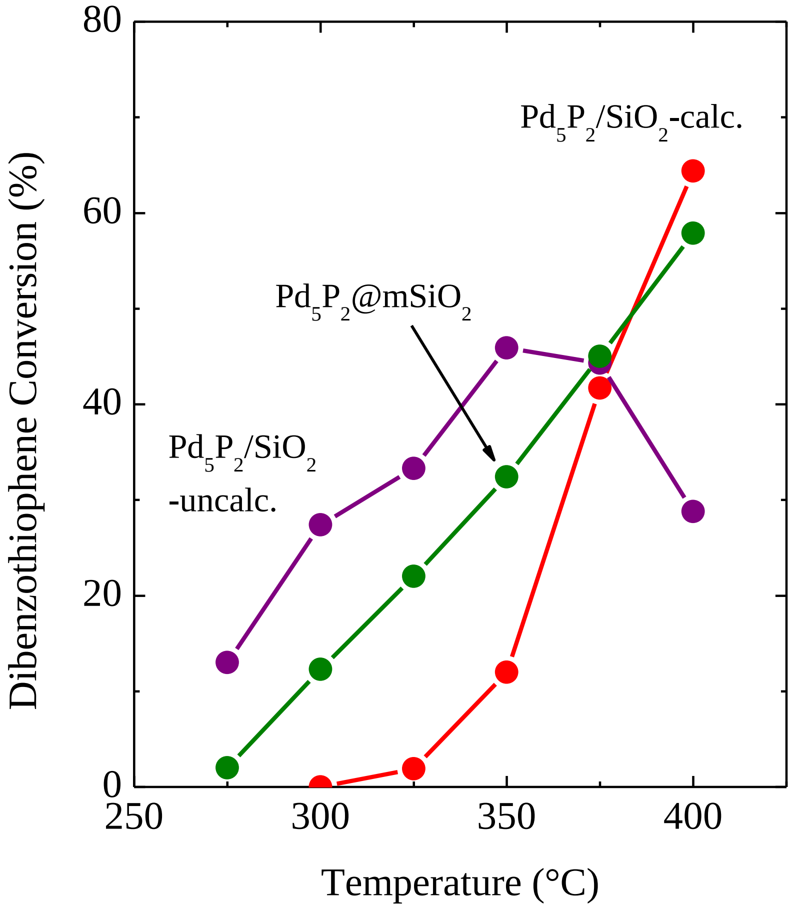

Figure 5.17. Dibenzothiophene HDS activity of 5 wt% Pd_5P_2@$mSiO_2$ and 5 wt% Pd_5P_2/SiO_2 prepared by temperature programmed reduction (calcined and uncalcined).[31]

The activity data are shown in Figure 5.17 for 5 wt% Pd_5P_2@$mSiO_2$ as well as for two 5 wt% Pd_5P_2/SiO_2 catalysts prepared by the conventional TPR method utilizing either calcined or uncalcined precursors.[31] The DBT conversion catalyzed by 5 wt% Pd_5P_2@$mSiO_2$ increases gradually and consistently with temperature. This activity proves that active sites on the Pd_5P_2 particles can be accessed by DBT within the mesoporous silica. In addition, the dibenzothiophene conversion of Pd_5P_2@$mSiO_2$ is significantly greater than that of a Pd_5P_2/SiO_2 catalyst (calcined precursor) at lower temperatures (<375 ºC) and the catalytic activity of the two catalysts is comparable at high temperatures (>375 ºC). While Pd_5P_2/SiO_2 prepared from an uncalcined precursor shows higher HDS activity compared to Pd_5P_2@$mSiO_2$, the activity of this catalyst drops significantly at relatively high temperature (>375 ºC), suggesting stability may be a problem, in contrast to the Pd_5P_2@$mSiO_2$ catalysts produced here. TEM and PXRD analyses done on a post-HDS Pd_5P_2@$mSiO_2$ sample indicates that particles have not sintered and the Pd_5P_2 phase has been recovered after HDS testing (Figure 5.18).

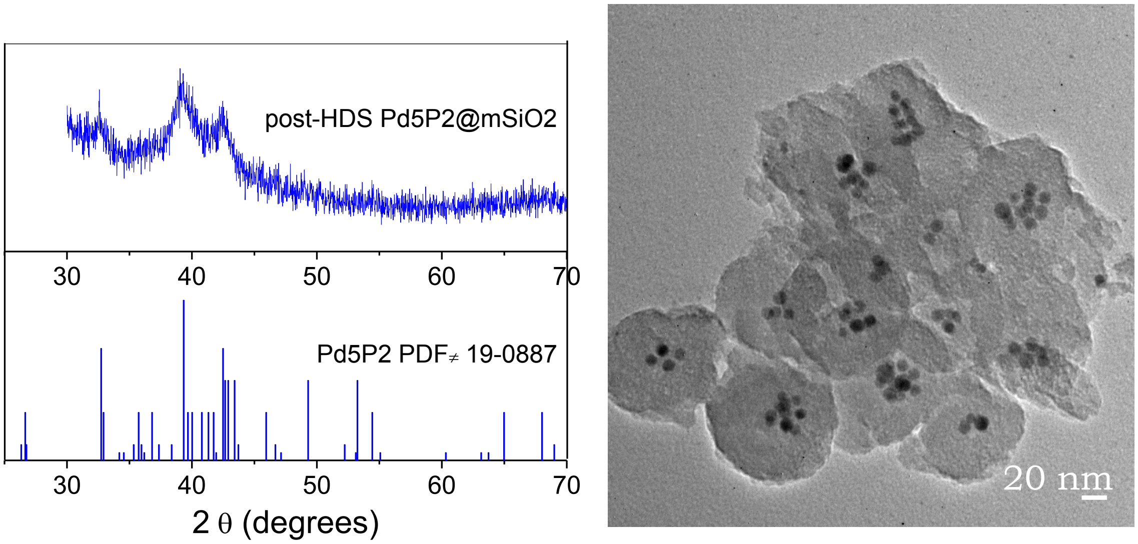

Figure 5.18. Post-HDS PXRD pattern (left) and post-HDS TEM image (right) of Pd_5P_2@$mSiO_2$ catalyst.

5.4 Conclusions

A method to synthesize Rh_2P nanoparticles has been developed, but suffers from aggregation and formation of an amorphous shell. In contrast, phase-pure monodisperse samples of 5-10 nm Pd_5P_2 can be prepared by encapsulation of amorphous Pd-P particles in a mesoporous silica shell prior to crystallization. The encapsulation has the benefit of producing the particles in a mesoporous silica matrix, which reduces sintering at the temperatures needed to crystallize Pd_5P_2, and under the harsh conditions needed to effect hydrodesulfurization of dibenzothiophene. In contrast to the Rh_2P aggregates which show poor HDS activity, the Pd_5P_2@mSiO_2 catalysts are competitive with TPR prepared materials. This study provides the framework for the study of size dependent HDS activity, detailed evaluation of products and study of the mechanism of activity of Pd_5P_2@mSiO_2.

CHAPTER 6

CONCLUSIONS AND PROSPECTUS

6.1 Conclusions

Increasingly stringent regulations on allowable sulfur levels in transportation fuels are placing high demands on the sulfide-based hydroprocessing catalysts used for the removal of sulfur and nitrogen impurities from fossil fuel feedstocks.[18] It is an open question whether the catalytic function of conventional sulfided Co-Mo and Ni-Mo catalysts can be enhanced sufficiently to efficiently process low quality feedstocks, such as those from the Canadian oil sands, to achieve the mandated ultra-low sulfur levels. Limitations on the activity of Mo-based sulfide catalysts can be attributed to the layered structure of MoS_2 wherein metal atoms are exposed only on the edge planes, resulting in low active site density.[99]

Therefore, a substantial research effort is now focused on exploring new catalytic systems based on materials exposing metal atoms on all crystallographic faces. Among them, Ni_2P prepared by the temperature programmed reduction (TPR) method has shown the greatest hydrodesulfurization (HDS) activity for binary metal phosphides. However, the size-dependent catalytic activity of Ni_2P for HDS catalysis remains unstudied because the traditional temperature programmed reduction (TPR) method used in catalyst preparation results in highly polydisperse Ni_2P particles.

The main goal of this dissertation research (aim I, Chapter 1.6) was to study the size and shape dependence of the activity of Ni_2P nanoparticle catalysts. To do this, synthetic methods enabling formation of Ni_2P with different sizes and shapes were developed. The synthesis of Ni_2P nanoparticles was carried out using the solution-phase arrested precipitation route where Ni-P amorphous particles were first formed from the precursor nickel source ($Ni(acac)_2$) and then converted to crystalline Ni_2P particles. In this reaction, oleylamine was used as a reducing agent and capping group. This method allows for the formation of monodisperse Ni_2P (standard deviation < 20%) nanoparticles. Moreover, the average particle size was tuned by changing the amount of oleylamine, which affects the nucleation rate of precursor nanoparticles. Ni_2P nanoparticles were highly crystalline, as revealed by the close agreement between average particle sizes as determined by TEM and crystallite size calculated from the most intense PXRD peak. Thus, the solution-phase arrested precipitation (SPAP) route enabled formation of much higher quality samples relative to the conventional TPR method.

The SPAP route in turn enabled the study of size-dependent HDS catalytic activity of Ni_2P particles. However, preliminary dibenzothiophene (DBT) HDS data collected for three different Ni_2P/SiO_2 samples with varying average particle sizes reveals that activities were lower than that of TPR-generated catalysts with similar loading. Moreover, the resulting activity trend with respect to the particle size was reversed with the trend expected by taking surface area to volume ratio into account (the smallest particle size showed the lowest activity). The post HDS PXRD patterns revealed significant peak sharpening resulting from ripening of particles under HDS conditions. Based on this observation, it was assumed that Ni_2P nanoparticles do not adhere to the silica support strongly enough to withstand aggregation and crystal growth under HDS conditions.

In order to understand the factors governing the sintering of particles, we systematically evaluated the sintering behavior as a function of different variables employed in HDS experiments. Heating experiments conducted under a 5% H_2/Ar mixture for various loadings (2.5, 5, 10, and 20% of Ni_2P on silica), temperatures (from 100 to 650 °C), heating times (from 30 minutes to 6 hrs), and method of impregnation (number of cycles, and amounts of solvent used) were performed. However, attempts to limit sintering by varying loading, time, incipient wetness steps and ionic attachment were unsuccessful. It was found that sintering behavior is a fast process, occurring within 15 minutes when the temperature is above 200 °C. Therefore, we concluded that supporting Ni_2P nanoparticles on silica using the incipient wetness method does not enable sintering to be avoided during HDS.

As an alternative option, the development of novel synthetic protocols for in-situ encapsulation of Ni_2P nanoparticles within a mesoporous silica shell that would avoid physical contact of nanoparticles at high temperature, while maintaining access of thiophenes to the particle surface, was performed. In addition to avoiding sintering, control of loading of Ni_2P nanoparticles was also an objective of this part of the dissertation research. A systematic study was performed to understand the in-situ incorporation of Ni_2P nanoparticles into a mesoporous silica network by changing reaction variables such as pH, time and loading. In contrast to noble metal nanoparticles, Ni_2P nanoparticles were susceptible to etching at higher pH. Therefore, we optimized the pH and time for carrying out the in-situ mesoporous silica encapsulation of Ni_2P nanoparticles. This is the first example of metal phosphide nanoparticle incorporation into a mesoporous silica network ($Ni_2P@mSiO_2$). Moreover, it was found that sintering of $Ni_2P@mSiO_2$ nanoparticles was minimized at high temperature under reducing conditions leading to dramatic improvement of catalytic activity relative to samples prepared by incipient wetness. Thus, $Ni_2P@mSiO_2$ catalysts showed the expected size-dependent HDS activity in contrast to the Ni_2P/SiO_2 catalysts. Most importantly, we showed control of loading of Ni_2P nanoparticles within the mesoporous silica shell with high accuracy in addition to high yield, and that this synthetic approach can be extended to other chemical systems (CdSe and Au NPs).

Noble metal phosphides prepared using the TPR method have shown enhanced deep-HDS activity (removal of sterically bulky thiophenes) due to the ability to favor the hydrogenation (HYD) pathway during HDS. Aim III (Chapter 1.6) of this dissertation research was to synthesize monodisperse noble metal phosphide nanoparticles such as Rh_2P and Pd_5P_2 with controlled sizes in order to study the deep-HDS activity of these systems with respect to particle size. Rh_2P nanoparticles were synthesized by the direct reaction between $RhCl_3$ and TOP in the presence of oleylamine as the reducing agent and octylether as the solvent at 360 °C. However, the Rh_2P nanoparticles formed were significantly aggregated. Accordingly, attention was refocused to Pd_5P_2 and a method was developed to synthesize monodisperse and small-sized spherical Pd_5P_2 nanoparticles that have not been accessible by solution-phase methods. A solid state phase transformation of precursor amorphous Pd-P nanoparticles embedded in a mesoporous silica network by heating under reducing conditions was successfully employed. The resultant Pd_5P_2@mSiO_2 (8-9 nm) showed high surface area and narrow pore size distribution. HDS data collected on Pd_5P_2@mSiO_2 revealed the catalytic nature of the system with comparable activity to TPR-prepared materials, thus showing that small molecules have accessibility to the Pd_5P_2 nanoparticle surfaces.

6.2 Prospectus

There are a number of unresolved issues that provide opportunities for future research, as indicated below.

6.2.1 Sintering in Ni_2P@mSiO_2

Although sintering of Ni_2P@mSiO_2 catalysts with larger Ni_2P nanoparticles (> 10 nm) was significantly reduced, the smallest Ni_2P nanoparticles (5-6 nm) used in Ni_2P@mSiO_2 catalyst showed significant sintering during HDS measurements (Chapter 4). It is assumed that these smaller nanoparticles can migrate through the mesopores of pore diameter (5-6 nm) which is in the same range as the particle size. Therefore, in order to probe the activity of these smallest sized Ni_2P nanoparticles, a mesoporous silica shell with an average pore size lower than the particle size is desired. Intriguingly though, while the smallest particles sinter the most, they are also the most active. More detailed studies are needed to understand how the chemical nature of the surface may be impacting activity, in addition to size.

It has been reported that the catalytic activity can be further improved by mesoporous silica coated catalysts by reducing the thickness of the silica shell. Our lab also will be working on reducing the thickness of this mesoporous shell in order to facilitate the catalytic reaction by reducing the mean free pathway of reactive species.

6.2.2 Ternary Metal Phosphides

As we have successfully developed synthetic methods to generate these catalytically active binary metal phosphide nanoparticles with great control over size and dispersity, our lab is now working on making ternary metal phosphide nanoparticles such as Ni_2P doped with Co or Fe ($Ni_{2-x}Fe_xP$ and $Ni_{2-y}Co_yP$). This is motivated by the fact that TPR-generated $Ni_{2-x}Fe_xP$ and $Ni_{2-y}Co_yP$ catalyts have shown greater HDS activity than TPR-generated Ni_2P. These doping metals have been found to act as promoter atoms in HDS catalysts. Therefore, a future goal of this project is the study of the HDS activity of these ternary phases as a function of size and composition.

6.2.3 Improving Rh_2P Nanoparticle Synthesis

The HDS activity of Rh_2P nanoparticles as a function of size has yet to be determined because of the aggregated nature of Rh_2P nanoparticles made using SPAP method. However, preliminary data suggests that changing the reducing agent from oleylamine to octadecylamine reduces the extent of aggregation. Accordingly, higher quality Rh_2P nanoparticles should be accessible in the near future, enabling a detailed and systematic study of the activity and mechanism (HYD vs. DDS).

REFERENCES

1. Huynh, W. U.; Dittmer, J. J.; Alivisatos, A. P., *Science* **2002,** *295* (5564), 2425-2427.

2. Liu, J.; Tanaka, T.; Sivula, K.; Alivisatos, A. P.; Fréchet, J. M. J., *Journal of the American Chemical Society* **2004,** *126* (21), 6550-6551.

3. Yao, Q.; Brock, S. L., *Nanotechnology* **2010,** *21* (11), 115502.

4. Eustis, S.; El-Sayed, M. A., *Chemical Society Reviews* **2006,** *35* (3), 209-217.

5. Trindade, T.; O'Brien, P.; Pickett, N. L., *Chem. Mater.* **2001,** *13* (11), 3843-3858.

6. Darling, S. B.; Yufa, N. A.; Cisse, A. L.; Bader, S. D.; Sibener, S. J., *Adv. Mater.* **2005,** *17* (20), 2446-2450.

7. Freestone, I.; Meeks, N.; Sax, M.; Higgitt, C., *Gold Bulletin* **2007,** *40* (4), 270-277.

8. Thompson, D., *Gold Bulletin* **2007,** *40* (4), 267-269.

9. Brock, S., L.; Perera, S.; Stamm, K., L., *Chemistry - A European Journal* **2004,** *10* (14), 3364-3371.

10. Brock, S. L.; Senevirathne, K., *Journal of Solid State Chemistry* **2008,** *181* (7), 1552-1559.

11. Schmid, G., *Wiley-VCH* **2004**.

12. Rotello, V., Building Blocks for Nanotechnology. Springer: 2004.

13. Joo, S. H.; Park, J. Y.; Tsung, C.-K.; Yamada, Y.; Yang, P.; Somorjai, G. A., *Nat Mater* **2009,** *8* (2), 126-131.

14. Oyama, S. T.; Wang, X.; Requejo, F. G.; Sato, T.; Yoshimura, Y., *Journal of Catalysis* **2002,** *209* (1), 1-5.

15. Carenco, S.; Boissière, C. d.; Nicole, L.; Sanchez, C. m.; Le Floch, P.; Mézailles, N., *Chemistry of Materials* **2010,** *22* (4), 1340-1349.

16. Ma, X.; Sakanishi, K.; Mochida, I., *Industrial & Engineering Chemistry Research* **1994,** *33* (2), 218-222.

17. Schulz, H.; Böhringer, W.; Ousmanov, F.; Waller, P., *Fuel Processing Technology* **1999,** *61* (1–2), 5-41.

18. Pawelec, B.; Navarro, R. M.; Campos-Martin, J. M.; Fierro, J. L. G., *Cat. Rev. - Sci. Eng.* **2011,** *1* (1), 23-42.

19. Zepeda, T. A.; Pawelec, B.; Fierro, J. L. G.; Halachev, T., *Applied Catalysis B* **2007,** *71* (3–4), 223-236.

20. Whitehurst, D. D.; Farag, H.; Nagamatsu, T.; Sakanishi, K.; Mochida, I., *Catalysis Today* **1998,** *45* (1–4), 299-305.

21. Topsøe, H., *Applied Catalysis A: General* **2007,** *322* (0), 3-8.

22. Hullinger, F., *Crystal Chemistry of the Chalcogenides and Pnictides of the Transition Metals. Struct. Bond*. 1968; Vol. 4, p 83-229.

23. Oyama, S. T., *Journal of Catalysis* **2003,** *216* (1–2), 343-352.

24. Sweeney, C. M.; Stamm, K. L.; Brock, S. L., *J. Alloys Compd.* **2008,** *448* (1–2), 122-127.

25. Sawhill, S. J.; Layman, K. A.; Van Wyk, D. R.; Engelhard, M. H.; Wang, C.; Bussell, M. E., *Journal of Catalysis* **2005,** *231* (2), 300-313.

26. Korányi, T. I., *Appl. Catal., A* **2003,** *239* (1–2), 253-267.

27. Qian, E. W.; Otani, K.; Li, L.; Ishihara, A.; Kabe, T., *Journal of Catalysis* **2004,** *221* (2), 294-301.

28. Röthlisberger, A.; Prins, R., *Journal of Catalysis* **2005,** *235* (1), 229-240.

29. Niquille-Röthlisberger, A.; Prins, R., *Journal of Catalysis* **2006,** *242* (1), 207-216.

30. Hayes, J. R.; Bowker, R. H.; Gaudette, A. F.; Smith, M. C.; Moak, C. E.; Nam, C. Y.; Pratum, T. K.; Bussell, M. E., *Journal of Catalysis* **2010,** *276* (2), 249-258.

31. Bowker, R. H.; Smith, M. C.; Pease, M. L.; Slenkamp, K. M.; Kovarik, L.; Bussell, M. E., *ACS Catalysis* **2011,** *1* (8), 917-922.

32. Oyama, S. T.; Lee, Y.-K., *Journal of Catalysis* **2008,** *258* (2), 393-400.

33. Delannoy, L.; El Hassan, N.; Musi, A.; Le To, N. N.; Krafft, J.-M.; Louis, C., *The Journal of Physical Chemistry B* **2006,** *110* (45), 22471-22478.

34. Ostgard, D. J.; Kustov, L.; Poeppelmeier, K. R.; Sachtler, W. M. H., *J. Catal.* **1992,** *133* (2), 342-357.

35. Wang, L.; Hall, W. K., *J. Catal.* **1983,** *82* (1), 177-184.

36. Chang, F.-W.; Kuo, M.-S.; Tsay, M.-T.; Hsieh, M.-C., *Applied Catalysis A: General* **2003,** *247* (2), 309-320.

37. Jacobs, G.; Ghadiali, F.; Pisanu, A.; Borgna, A.; Alvarez, W. E.; Resasco, D. E., *Applied Catalysis A: General* **1999,** *188* (1–2), 79-98.

38. Oyama, S. T.; Wang, X.; Lee, Y. K.; Bando, K.; Requejo, F. G., *J. Catal.* **2002,** *210* (1), 207-217.

39. Sawhill, S. J.; Phillips, D. C.; Bussell, M. E., *Journal of Catalysis* **2003,** *215* (2), 208-219.

40. Leary, K. J., *AIChE J.* **1987,** *33* (8), 1407-1408.

41. Murray, C. B.; Norris, D. J.; Bawendi, M. G., *J. Am. Chem. Soc.* **1993,** *115* (19), 8706-8715.

42. Yunle, G.; Fan, G.; Yitai, Q.; Huagui, Z.; Ziping, Y., *Mater. Res. Bull.* **2002,** *37* (6), 1101-1105.

43. Kahlweit, M., *Adv. Colloid Interface Sci.* **1975,** *5* (1), 1-35.

44. Lukehart, C. M.; Milne, S. B.; Stock, S. R., *ChemInform* **1998,** *29* (24), no-no.

45. Burnam, K. J.; Carpenter, J. P.; Lukehart, C. M.; Milne, S. B.; Stock, S. R.; Jones, B. D.; Glosser, R.; Wittig, J. E., *Nanostruct. Mater.* **1995,** *5* (2), 155-169.

46. Perera, S. C.; Fodor, P. S.; Tsoi, G. M.; Wenger, L. E.; Brock, S. L., *Chemistry of Materials* **2003,** *15* (21), 4034-4038.

47. Perera, S. C.; Tsoi, G.; Wenger, L. E.; Brock, S. L., *J. Am. Chem. Soc.* **2003,** *125* (46), 13960-13961.

48. Park, J.; Koo, B.; Hwang, Y.; Bae, C.; An, K.; Park, J.-G.; Park, H. M.; Hyeon, T., *Angew. Chem. Int. Ed.* **2004,** *43* (17), 2282-2285.

49. Park, J.; Koo, B.; Yoon, K. Y.; Hwang, Y.; Kang, M.; Park, J.-G.; Hyeon, T., *Journal of the American Chemical Society* **2005,** *127* (23), 8433-8440.

50. Wang, J.; Johnston-Peck, A. C.; Tracy, J. B., *Chem. Mater.* **2009,** *21* (19), 4462-4467.

51. Qian, C.; Kim, F.; Ma, L.; Tsui, F.; Yang, P.; Liu, J., *Journal of the American Chemical Society* **2004,** *126* (4), 1195-1198.

52. Henkes, A. E.; Schaak, R. E., *Chem. Mater.* **2007,** *19* (17), 4234-4242.

53. Henkes, A. E.; Vasquez, Y.; Schaak, R. E., *Journal of the American Chemical Society* **2007,** *129* (7), 1896-1897.

54. Chiang, R.-K.; Chiang, R.-T., *Inorg. Chem.* **2006,** *46* (2), 369-371.

55. Zheng, X.; Yuan, S.; Tian, Z.; Yin, S.; He, J.; Liu, K.; Liu, L., *Materials Letters* **2009,** *63* (27), 2283-2285.

56. Senevirathne, K.; Burns, A. W.; Bussell, M. E.; Brock, S. L., *Advanced Functional Materials* **2007,** *17* (18), 3933-3939.

57. Gregg, K. A.; Perera, S. C.; Lawes, G.; Shinozaki, S.; Brock, S. L., *Chem. Mater.* **2006,** *18* (4), 879-886.

58. Muthuswamy, E.; Kharel, P. R.; Lawes, G.; Brock, S. L., *ACS Nano* **2009,** *3* (8), 2383-2393.

59. Muthuswamy, E.; Savithra, G. H. L.; Brock, S. L., *ACS Nano* **2011,** *5* (3), 2402-2411.

60. Muthuswamy, E.; Brock, S. L., *Chem Commun (Camb)* **2011,** *47* (45), 12334-6.

61. Muthuswamy, E.; Brock, S. L., *Journal of the American Chemical Society* **2010,** *132* (45), 15849-15851.

62. Fultz, B. H., J., Transmission Electron Microscopy and Diffractometry of Materials. Springer: 2000.

63. Dean, J. R., *Atomic Absorption and Plasma Spectroscopy*. John Wiley & Sons, Ltd., 1997.

64. Webb, P. A. O., C, *Analytical Methods in Fine Particle Technology*. Micromeritics Instrument Corporation, 1997.

65. Chiang, R.-K.; Chiang, R.-T., *Inorganic Chemistry* **2007,** *46* (2), 369-371.

66. Carenco, S.; Resa, I.; Le Goff, X.; Le Floch, P.; Mezailles, N., *Chemical Communications* **2008,** (22), 2568-2570.

67. Jana, N. R.; Gearheart, L.; Murphy, C. J., *Langmuir* **2001,** *17* (22), 6782-6786.

68. Niesz, K.; Grass, M.; Somorjai, G. A., *Nano Letters* **2005,** *5* (11), 2238-2240.

69. Baker, C. O.; Shedd, B.; Tseng, R. J.; Martinez-Morales, A. A.; Ozkan, C. S.; Ozkan, M.; Yang, Y.; Kaner, R. B., *ACS Nano* **2011,** *5* (5), 3469-3474.

70. Ji, X.; Song, X.; Li, J.; Bai, Y.; Yang, W.; Peng, X., *Journal of the American Chemical Society* **2007,** *129* (45), 13939-13948.

71. Campbell, C. T.; Parker, S. C.; Starr, D. E., *Science* **2002,** *298* (5594), 811-814.

72. Nanda, K. K.; Maisels, A.; Kruis, F. E.; Fissan, H.; Stappert, S., *Physical Review Letters* **2003,** *91* (10), 106102.

73. Wang, L.; Shi, J.; Zhu, Y.; He, Q.; Xing, H.; Zhou, J.; Chen, F.; Chen, Y., *Langmuir* **2012,** *28* (11), 4920-4925.

74. Wang, S.; Zhang, M.; Zhang, W., *ACS Catalysis* **2011,** *1* (3), 207-211.

75. Lee, I.; Zhang, Q.; Ge, J.; Yin, Y.; Zaera, F., *Nano Research* **2011,** *4* (1), 115-123.

76. Chen, Y.; Chen, H.; Zeng, D.; Tian, Y.; Chen, F.; Feng, J.; Shi, J., *ACS Nano* **2010,** *4* (10), 6001-6013.

77. Han, L.; Lv, Y.; Asiri, A. M.; Al-Youbi, A. O.; Tu, B.; Zhao, D., *Journal of Materials Chemistry* **2012,** *22* (15), 7274-7279.

78. Osseni, S. A.; Lechevallier, S.; Verelst, M.; Dujardin, C.; Dexpert-Ghys, J.; Neumeyer, D.; Leclercq, M.; Baaziz, H.; Cussac, D.; Santran, V.; Mauricot, R., *Journal of Materials Chemistry* **2011,** *21* (45), 18365-18372.

79. Liu, J.; Bu, W.; Zhang, S.; Chen, F.; Xing, H.; Pan, L.; Zhou, L.; Peng, W.; Shi, J., *Chemistry – A European Journal* **2012,** *18* (8), 2335-2341.

80. Lee, J. E.; Lee, D. J.; Lee, N.; Kim, B. H.; Choi, S. H.; Hyeon, T., *Journal of Materials Chemistry* **2011,** *21* (42), 16869-16872.

81. Lee, J. E.; Lee, N.; Kim, T.; Kim, J.; Hyeon, T., *Accounts of Chemical Research* **2011,** *44* (10), 893-902.

82. Kim, T.; Momin, E.; Choi, J.; Yuan, K.; Zaidi, H.; Kim, J.; Park, M.; Lee, N.; McMahon, M. T.; Quinones-Hinojosa, A.; Bulte, J. W. M.; Hyeon, T.; Gilad, A. A., *Journal of the American Chemical Society* **2011,** *133* (9), 2955-2961.

83. Lee, J. E.; Lee, N.; Kim, H.; Kim, J.; Choi, S. H.; Kim, J. H.; Kim, T.; Song, I. C.; Park, S. P.; Moon, W. K.; Hyeon, T., *Journal of the American Chemical Society* **2009,** *132* (2), 552-557.

84. Nooney, R. I.; Dhanasekaran, T.; Chen, Y.; Josephs, R.; Ostafin, A. E., *Advanced Materials* **2002,** *14* (7), 529-532.

85. Khalil; Mahmoud, H. A.; Ali, T. T., *Langmuir* **2008,** *24* (3), 1037-1043.

86. Peng, Y.-K.; Lai, C.-W.; Liu, C.-L.; Chen, H.-C.; Hsiao, Y.-H.; Liu, W.-L.; Tang, K.-C.; Chi, Y.; Hsiao, J.-K.; Lim, K.-E.; Liao, H.-E.; Shyue, J.-J.; Chou, P.-T., *ACS Nano* **2011,** *5* (5), 4177-4187.

87. Lin, K. J.; Chen, L. J.; Prasad, M. R.; Cheng, C. Y., *Advanced Materials* **2004,** *16* (20), 1845-1849.

88. Fan, H.; Leve, E. W.; Scullin, C.; Gabaldon, J.; Tallant, D.; Bunge, S.; Boyle, T.; Wilson, M. C.; Brinker, C. J., *Nano Letters* **2005,** *5* (4), 645-648.

89. Kim, J.; Kim, H. S.; Lee, N.; Kim, T.; Kim, H.; Yu, T.; Song, I. C.; Moon, W. K.; Hyeon, T., *Angewandte Chemie International Edition* **2008,** *47* (44), 8438-8441.

90. Gorelikov, I.; Matsuura, N., *Nano Letters* **2007,** *8* (1), 369-373.

91. Fan, H.; Yang, K.; Boye, D. M.; Sigmon, T.; Malloy, K. J.; Xu, H.; López, G. P.; Brinker, C. J., *Science* **2004,** *304* (5670), 567-571.

92. Kim, J.; Lee, J. E.; Lee, J.; Yu, J. H.; Kim, B. C.; An, K.; Hwang, Y.; Shin, C.-H.; Park, J.-G.; Kim, J.; Hyeon, T., *Journal of the American Chemical Society* **2005,** *128* (3), 688-689.

93. Wang, J.; Yang, Q.; Zhang, Z.; Sun, S., *Chem. Eur. J.* **2010,** *16* (26), 7916-7924.

94. Wang, Z.; Zhou, L.; Zhang, M.; Su, M.; Li, W.; Tao, K., *Chem. Asian. J.* **2009,** *4* (12), 1794-1797.

95. Zafiropoulou, I.; Papagelis, K.; Boukos, N.; Siokou, A.; Niarchos, D.; Tzitzios, V., *J. Phys. Chem. C.* **2010,** *114* (17), 7582-7585.

96. Bowker, R. H.; Smith, M. C.; Carillo, B. A.; Bussell, M. E., *Top. Catal.* **2012,** *55*, 999-1009.

97. Guan, Q.; Sun, C.; Li, R.; Li, W., *Catal. Commun.* **2011,** *14*, 114-117.

98. Muthuswamy, E.; Brock, S. L., *Chemical Communications* **2011,** *47* (45), 12334-12336.

99. Faur Ghenciu, A., *Current Opinion in Solid State and Materials Science* **2002,** *6* (5), 389-399.

ABSTRACT

SYNTHESIS AND CHARACTERIZATION OF SIZE CONTROLLED TRANSITION METAL PHOSPHIDE NANOPARTICLES AND THEIR HYDRODESULFURIZATION CATALYTIC ACTIVITY

by

GALBOKKA HEWAGE LAYAN SAVITHRA

May 2013

Advisor: Dr. Stephanie L. Brock

Major: Chemistry

Degree: Doctor of Philosophy

Transition metal phosphides are promising catalysts for hydrodesulfurization (HDS). The size-dependent catalytic activity of these metal phosphides for hydrodesulfurization (HDS) remains unstudied because the traditional temperature programmed reduction (TPR) method used in catalyst preparation results in highly polydisperse particles.

The main goals of this dissertation research are (1) synthesize metal phosphide nanoparticles (Ni_2P, Rh_2P, and Pd_5P_2) with control of size and morphology using a solution phase arrested precipitation method (SPAP); (2) develop a large scale synthesis of mesoporous silica encapsulated nanoparticles (Ni_2P and Pd_5P_2) with controlled loading to prevent sintering at high temperatures; (3) establish the structure activity relationship of Ni_2P nanoparticles in HDS and study the deep-HDS activity of noble metal phosphides.

The ability to control the Ni_2P particle size on the nanoscale using solution-phase arrested precipitation is reported in this dissertation. Ni_2P particles were introduced to a high surface area silica support (Cab-O-Sil, M-7D grade, 200 m^2/g) via incipient wetness and HDS activity was probed against dibenzothiophene (DBT). All samples were less active than TPR prepared

materials and the smallest particles were the least active, contrary to expectation. This is attributed in part to particle sintering under HDS conditions. Sintering occurs independently of wt% loading of catalyst, time, incipient wetness procedure and ionic additives, at all temperatures greater than 200 °C.

To minimize sintering, we developed a route for in-situ mesoporous silica encapsulation of Ni_2P nanoparticles. We optimized the Ni_2P@$mSiO_2$ synthesis to yield samples on large scale with controlled loading. The generality of this approach is employed to other systems such as CdSe and Au. Sintering is minimized by encapsulation of Ni_2P nanoparticles in a mesoporous silica shell, resulting in a doubling of HDS activity. This enables us to study size-dependent HDS of Ni_2P nanoparticles.

The synthesis of monodisperse 5-10 nm Pd_5P_2 catalytic particles by encapsulation in a mesoporous silica network, along with preliminary data on hydrodesulfurization (HDS) activity, is also reported in this dissertation. Precursor Pd-P amorphous nanoparticles are prepared by solution-phase reaction of palladium (II) acetylacetonate with trioctylphosphine at temperatures up to 300 ºC. Direct crystallization of Pd_5P_2 in solution by increasing temperatures to 360 ºC leads to sintering, but particle size can be maintained during the transformation by encapsulation of the amorphous Pd-P particles in a mesoporous silica shell, followed by treatment of the solid at 500 ºC under a reducing atmosphere, yielding Pd_5P_2@$mSiO_2$. The resultant materials exhibit high BET surface areas (> 1000 m^2/g) and an average pore size of 3.7 nm. Access to the catalyst surface is demonstrated by dibenzodithiophene (DBT) HDS testing. Pd_5P_2@$mSiO_2$ shows a consistent increase in HDS activity as a function of temperature, with DBT conversion approaching 60% at 675 K. The ability to control particle size, phase, and sintering is expected to enable the fundamental catalytic attributes that underscore activity in Pd_5P_2 to be assessed.

AUTOBIOGRAPHICAL STATEMENT

GALBOKKA H. LAYAN SAVITHRA

Education

- 2007-2012 Ph.D., Inorganic Chemistry, Wayne State University, Detroit, MI
  Dissertation: Synthesis and characterization of size controlled transition metal phosphide nanoparticles and their hydrodesulfurization catalytic activity
  Advisor: Prof. Stephanie L. Brock
- Bachelor of Science (B.Sc.) First Class Honors in Chemistry, University of Colombo, Colombo, Sri Lanka, 2006

Research and Training Experience

- **08/2007 – 08/2009** Graduate Teaching Assistant, Dept. of Chemistry, Wayne State University, Detroit, MI
- **08/2009 – 12/2012** Graduate Research Assistant, Dept. of Chemistry, Wayne State University, Detroit, MI
- **08/2006 – 07/2007** Graduate Teaching Assistant, Department of Chemistry, University of Colombo, Colombo, Sri Lanka

Technical Skills

Glove box and Schlenk line synthetic techniques, Powder X-ray Diffraction, Transmission Electron Microscopy, Energy Dispersive Spectroscopy, Thermogravimetric Analysis, UV-Visible and Infra-Red Spectroscopies, Porosimetry Analysis

Awards and Fellowships:

- Summer Dissertation Fellowship, 2012, Graduate School, Wayne State University, Detroit, Michigan.

- Winner of the Prof. R.S. Ramakrishna Gold Medal for the best performance in Inorganic Chemistry in the Chemistry Special/Major Degree program at convocation, 2006, Colombo, Sri Lanka

- Winner of the Prof. P. P. G. L. Siriwardena memorial scholarship for the best performance in Chemistry during the third year of the Chemistry major degree program

- Winner of the Dr. C. L. de Silva Memorial Prize for the best performance in Chemistry in the first two years of the Bachelor of Science degree program

Publications

1. Muthuswamy, E.; Savithra, G. H. L.; Brock, S. L. Synthetic Levers Enabling Independent Control of Phase, Size, and Morphology in Nickel Phosphide Nanoparticles. *ACS Nano* **2011**, *5*, 2402–2411
2. Wani, A.; Muthuswamy, E.; Savithra, G.; Mao, G.; Brock, S.; Oupický, D., Surface Functionalization of Mesoporous Silica Nanoparticles Controls Loading and Release Behavior of Mitoxantrone
3. Rational Design of Nickel Phosphide Hydrodesulfurization Catalysts: Controlling Particle Size and Preventing Sintering (manuscript submitted)
4. Mesoporous Matrix Encapsulation for the Synthesis of Monodisperse Pd_5P_2 Nanoparticle Hydrodesulfurization Catalysts: Size Dependent Catalytic Activity of Supported Ni_2P Nanoparticles (manuscript submitted)
5. Large-scale Synthesis of Mesoporous Silica Encapsulated Nanoparticles (manuscript in preparation)